Detection of Magnetic Monopoles below the Cherenkov Limit

Cover photograph by Martijn de Jonge, http://www.martijndejonge.nl/

Printed by Ponsen & Looijen b.v., Wageningen.

The work described in this thesis is part of the research programme of the Nationaal Instituut voor Kernfysica en Hoge-Energiefysica (NIKHEF) in Amsterdam, the Netherlands. The author was financially supported by the Stichting voor Fundamenteel Onderzoek der Materie (FOM).

Detection of Magnetic Monopoles below the Cherenkov Limit

Academisch Proefschrift

ter verkrijging van de graad van doctor
aan de Universiteit van Amsterdam
op gezag van de Rector Magnificus
prof.mr. P.F. van der Heijden
ten overstaan van een door het college voor promoties
ingestelde commissie, in het openbaar te verdedigen
in de Aula der Universiteit
op vrijdag 7 juli 2006, te 14:00 uur

door

Bram Antonius Philomena van Rens

geboren te Tegelen

Promotores: Prof. dr. P.M. Kooijman
Prof. dr. M. de Jong

Faculteit der Natuurwetenschappen, Wiskunde en Informatica

Contents

Introduction

Already many centuries before Christ, the ancient Chinese and Greeks knew about rare stones that had the power to attract iron. Large deposits of these stones were found near an ancient town named Magnesia in what is nowadays Turkey. From this town the word magnetism is derived. The first scientific study of magnetic materials may be attributed to the medieval crusader and engineer Petrus Peregrinus de Maricourt. In 1269 he wrote his "Epistola de Magnete", in which he describes the dipolarity of magnets, and names the poles north and south. Subsequent observations have shown that all magnetic objects are dipoles, no isolated magnetic poles have ever been found. Nevertheless, it has been theorised that isolated magnetic poles, called magnetic monopoles, can exist in the form of sub-atomic particles. These particles would then carry a net magnetic charge.

Many of the theories that predict the existence of magnetic monopoles aim to unify the strong, weak and electromagnetic interactions. This unification is expected to occur at the extreme energy scales that were available in the early Universe. As the Universe evolved toward lower energies, the unification broke down, leaving magnetic monopoles as relic particles. Monopoles could therefore provide information on the earliest moments of our Universe and on energy scales far beyond the reach of man-made particle accelerators. The various unification schemes and mechanisms for the acceleration of relic monopoles in the cosmos result in a wide range of possible monopole masses and velocities.

This thesis describes the preparatory work for a monopole search with the ANTARES neutrino telescope. This is an underwater detector that is designed for the detection of high-energy cosmic neutrinos. The detection principle relies on the observation of Cherenkov light that is emitted by neutrino-induced muons. Unlike searches that have already been performed with other neutrino telescopes, the work presented here does not concern monopoles with velocities equal or close to the speed of light. These fast monopoles produce a Cherenkov signal in the detector that is similar to that of a muon, but which is much brighter.

As theoretical predictions cover a wide range of monopole velocities, the searches for monopoles with neutrino telescopes should be extended to lower velocities. Monopoles cease to emit Cherenkov light when their velocity drops below the speed of light in the sea water ($0.74\,c$). This threshold velocity is referred to as the Cherenkov limit. However, the interaction of monopoles with the electrons in the water molecules results in the liberation of energetic electrons. These so-called δ-rays may have enough kinetic energy to emit Cherenkov light. This process leads to detectable signals of monopoles with velocities below the Cherenkov limit. The detection of these monopoles is the subject of the work described in this thesis.

Chapter 1 gives an introduction to the ANTARES experiment. It includes a descrip-

tion of the detection principle, architecture, data acquisition system and calibration of the detector. In chapter 2, the data transmission system of the ANTARES detector is explained in more detail. Measurements carried out to quantify the performance of this system are summarised. The theoretical background of the creation and acceleration of monopoles is briefly discussed in chapter 3 together with an inventory of upper limits on the cosmic monopole flux. In chapter 4, the signals of monopoles that can lead to detection in the ANTARES detector are presented. The inclusion of these signals into a simulation program is described as well. The development and performance of a trigger designed specifically for monopoles with velocities below the Cherenkov limit are discussed in chapter 5. The method that is used to analyse the events found by this monopole trigger is presented in chapter 6. These new trigger and analysis methods have been used to determine the discovery potential and upper flux limit of the ANTARES detector for monopoles with velocities down to about half the speed of light.

Chapter 1

The ANTARES neutrino telescope

The ANTARES collaboration is constructing an underwater neutrino telescope on the bottom of the Mediterranean Sea, about 40 km off the coast of Toulon in the south of France. The main physics goals of the ANTARES collaboration include detection of cosmic neutrinos, a search for astrophysical neutrino sources, indirect neutralino detection and searches for exotic particles like magnetic monopoles. In this chapter the basic detection principle of a neutrino telescope is briefly explained, as well as the specific architecture of the ANTARES detector. Descriptions of the data acquisition system and the calibration of the detector are given, including an explanation of the software trigger that is used. Estimates of the expected angular and energy resolution are also given. Finally, the simulation of the physics processes involved and the corresponding detector response are described.

1.1 Detection principle

The ANTARES detector is designed primarily for the detection of high-energy muon neutrinos (ν_μ) [1]. It consists of a large number of photo-multiplier tubes (PMTs) that are positioned in a three-dimensional lattice on the sea floor. A muon neutrino can interact with matter inside or near the instrumented detector volume via a charged current weak interaction in which a muon (μ) is produced. While travelling through the sea water at relativistic velocity, the muon emits Cherenkov radiation that can be detected by the PMTs. From the measurement of the arrival times and intensities of this Cherenkov light at different positions in the detector, the path and the energy of the muon can be reconstructed. From this information the direction and the energy of the incident neutrino can be deduced.

1.1.1 Neutrino interactions

The charged current interaction of a muon neutrino with a nucleon, $\nu_\mu + N \rightarrow \mu + X$, is dominantly deeply inelastic for neutrino energies above 10 GeV [2]. The interaction results in the break-up of the target nucleon into a hadronic state X and in the emergence of a muon. Below neutrino energies of 10 TeV, the cross section of this process rises linearly with the energy of the neutrino [2]. For energies above 10 TeV, the increase of the cross

section becomes less than linear with the neutrino energy. The cross section is about 10^{-37} cm^2 at a neutrino energy of 10 GeV, and increases to approximately 10^{-33} cm^2 at 10 PeV. Because of these small cross sections, a large detector volume is needed for a detectable event rate.

Due to the scattering angle of the muon at the neutrino interaction point, the direction of the muon may deviate from the initial neutrino direction. A safe limit on the average angular difference between the neutrino and muon direction $\langle\theta_{\nu\mu}\rangle$ is

$$\langle\theta_{\nu\mu}\rangle < \frac{1.5^\circ}{\sqrt{E_\nu}} \ , \tag{1.1}$$

where the energy of the neutrino E_ν is in TeV. This shows that the direction of the neutrino and the muon are closely related at high energies. The average energy of the emerging muon is roughly half of the initial neutrino energy [2]. These relations are used to estimate the initial neutrino direction and energy from the measured muon properties.

1.1.2 Cherenkov radiation

A charged particle radiates light when it has a velocity that exceeds the phase velocity of light in the medium it travels through [3]. This so-called Cherenkov radiation is a coherent emission of light in a very narrow cone at a characteristic angle with respect to the path of the particle. This Cherenkov angle is given by

$$\cos\theta_c = \frac{1}{\beta n} \ , \tag{1.2}$$

where n is the index of refraction of the medium and βc the velocity of the particle, with c the speed of light in vacuum. The minimum particle velocity for this phenomenon to occur is thus c/n. In that case, the angle at which the light is emitted is 0 degrees.

The number of photons N emitted per unit path length dx of the particle and per unit wavelength interval $d\lambda$ of the photons is

$$\frac{d^2N}{dxd\lambda} = \frac{2\pi\alpha z^2}{\lambda^2}\left(1 - \frac{1}{\beta^2 n^2}\right) \ , \tag{1.3}$$

where ze is the charge of the particle and α is the fine structure constant. With a refractive index of sea water of about 1.35 [4], a highly relativistic muon ($z = 1,\ \beta \simeq 1$) produces about 345 Cherenkov photons per cm path length in the sensitive wavelength range of the PMT (see section 1.2). The corresponding Cherenkov angle is then approximately 42 degrees.

1.1.3 Light propagation

The propagation of the Cherenkov light from the muon path to the PMTs depends on several optical properties of the sea water. Firstly, photons can be absorbed by water molecules and sedimentation in the sea water. The degree of absorption can be characterised by the absorption length λ_{abs}. Absorption mainly affects the intensity I of the

Cherenkov light arriving on the PMTs, which decreases with the photon path length r as

$$I \propto \frac{1}{r} e^{-r/\lambda_{abs}} \ . \tag{1.4}$$

The factor $1/r$ arises from the geometrical expansion of the Cherenkov cone. Another property of sea water involves the scattering of photons off molecules and microscopic particles in the water. It can be characterised by the scattering length λ_{sct}, which is the mean distance between two scatters. Scattering mainly affects the arrival times of the Cherenkov light on the PMTs, and consequently the angular resolution (see section 1.7). The λ_{abs} and λ_{sct} of the sea water at the ANTARES site are about 60 and 260 m respectively for a photon wavelength of 473 nm [5].

The velocity of the Cherenkov light in the water is given by the group velocity v_g [6], which is characterised by a group refractive index $n_g = c/v_g$ of about 1.38 at a wavelength of 460 nm [7]. The wavelength dependence of v_g introduces a small spread in the propagation times of the Cherenkov photons. This effect is generally referred to as dispersion. For a photon path length of 150 m, the resulting spread in the arrival times on the PMTs is about 2 ns [7].

1.2 Detector architecture

The ANTARES detector will be located on the floor of the Mediterranean Sea at a depth of 2.5 km. The site is about 40 km off the southern French coast at a latitude of 42°50′ N and a longitude of 6°10′ E. The detector will be operated from a control room on shore, called the shore station. A single cable provides the connection between the shore station and the detector. Figure 1.1 shows a schematic view of the detector. A detailed description of the detector design can be found in [8].

The PMT that was selected as sensitive element in the ANTARES experiment is the Hamamatsu R7081-20. It is a hemispherical tube with a photo-cathode area of about 500 cm^2 and 14 amplification stages. The PMT is sensitive to single photons in the wavelength range from 300 to 600 nm. Its quantum efficiency peaks at approximately 400 nm, where it is about 25%. The gain of the PMT is 5×10^7 for a typical high voltage of 1800 V. The transit time spread and charge resolution of the PMT for this gain are 2.6 ns (FWHM) and 40% respectively [9]. Together with the base that provides the high voltage and a LED calibration system, the PMT is assembled into a pressure resistant glass sphere. A transparent gel provides the optical and mechanical contact between the PMT and the glass sphere. A μ-metal cage is immersed in the optical gel to shield the PMT from the Earth's magnetic field. The back of the glass sphere is painted black [10] and contains a penetrator that provides a waterproof connection to the outside. In figure 1.2 a schematic view of the whole assembly, referred to as an optical module (OM), is shown.

A triplet of OMs forms a storey, of which a photograph is shown in figure 1.3. The OMs are mounted on a titanium frame at equidistant angles, facing away from the centre of the frame and downward at an angle of 45 degrees with respect to the horizontal. The frame also supports the local control module (LCM), a titanium cylinder that contains the read-out and control electronics of the OMs. The read-out electronics contain several

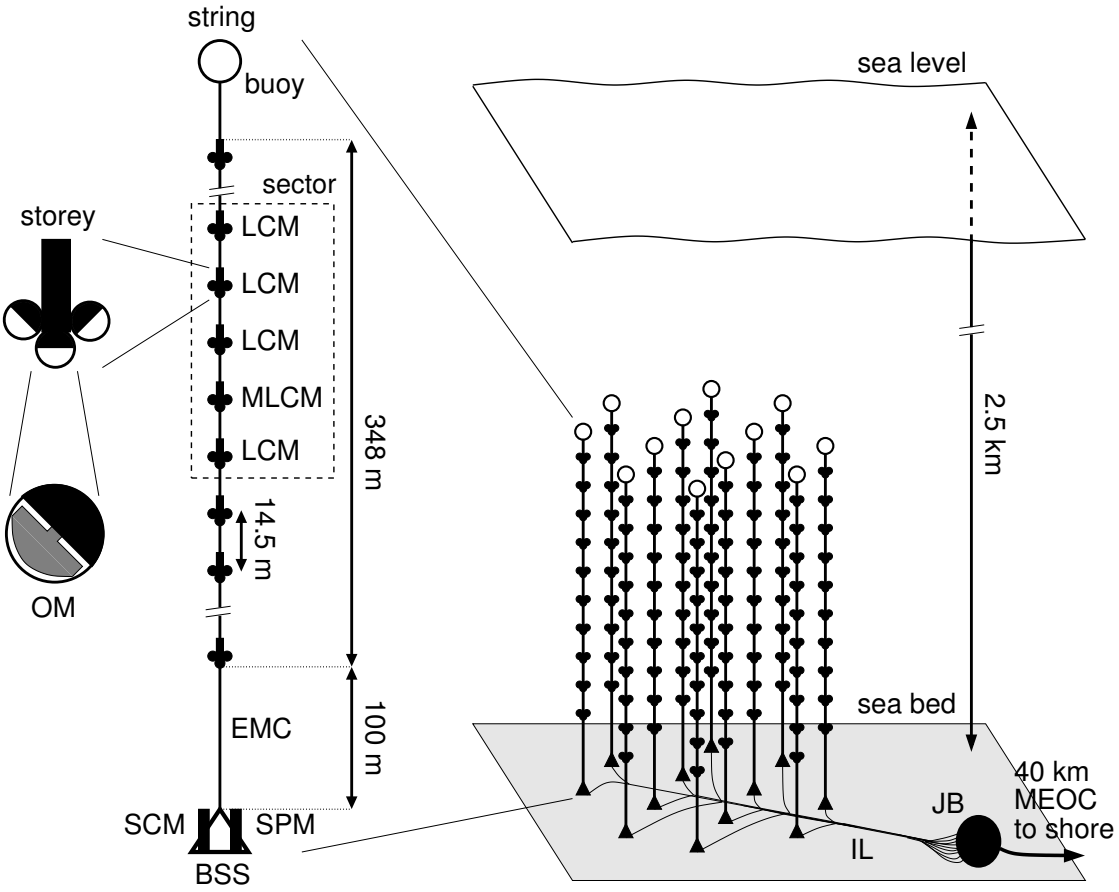

Figure 1.1: *A schematic view of the ANTARES detector architecture. The sensitive elements in the detector are photo-multiplier tubes (PMTs). Each PMT is housed in a pressure resistant glass sphere. The assembly is called optical module (OM), of which three are mounted on each storey. The local control module (LCM) in each storey contains the read-out and control electronics. A complete detector string consists of 25 storeys spaced 14.5 metres apart. The string is anchored with the bottom string socket (BSS) that also contains the string control module (SCM) and string power module (SPM). The string is kept vertical by a buoy at the top of the string. The complete detector comprises 12 strings situated on the sea bed. Each string is connected to the junction box (JB) which is the interface to the main electro-optical cable (MEOC). The 40 km long MEOC is the single cable to shore that accommodates all electrical and optical links.*

front-end chips that digitise the signals of the PMTs, and a processor that sends these data to shore. The OMs are connected to the LCM with a cable that penetrates both the OM and LCM housing.

Storeys are interconnected with an electro-mechanical cable (EMC), which serves as mechanical link between the storeys. It also contains electrical wires for power distribution to the LCMs, and optical fibres for the data transmission between the LCMs and the shore. A group of five storeys forms a sector. Each sector has its own power supply and an independent optical data link to shore. The data from all LCMs in the same sector are

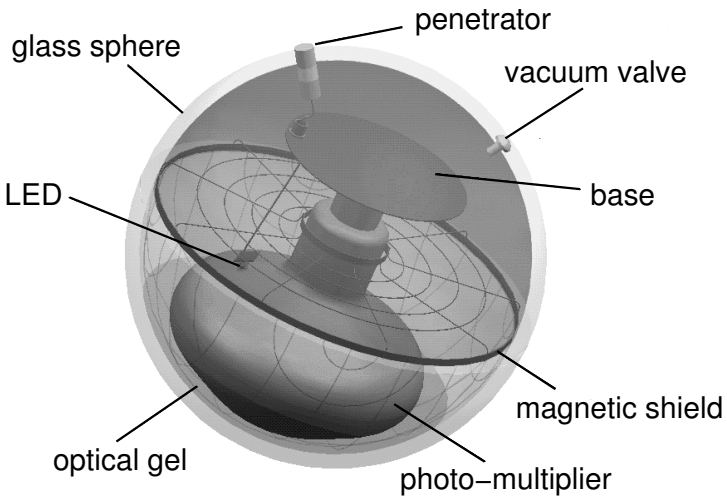

Figure 1.2: *A schematic view of the optical module (OM) used in ANTARES, taken from [9].*

collected in the master local control module (MLCM) and sent to shore using this link. Signals coming from shore are distributed within the sector via the MLCM.

Five serially connected sectors constitute a full detector string. The spacing of the storeys in the string is 14.5 metres. The string is anchored on the sea bed with the bottom string socket (BSS). The BSS also holds the string control module (SCM) with control electronics for the string, and the string power module (SPM) that contains the power supplies for the sectors and the SCM. The bottom 100 metres of the string, between the BSS and the first storey, are not instrumented. The string is kept vertical by a buoy at the top of the string.

Figure 1.3: *Photograph of two fully integrated storeys. A titanium frame supports three optical modules that are connected to the local control module which contains the control and read-out electronics. The frame also provides the mechanical connection to the electro-mechanical cable that interconnects the storeys.*

The complete detector consists of 12 strings that are positioned on the sea bed some 60 metres apart on a grid as shown in figure 1.4. In this way a lattice of 900 PMTs is constructed which instruments a volume of approximately 0.02 km^3 of the sea. Each string is connected with an Interconnecting Link (IL) to the junction box (JB), which is the interface to the single 40 km long main electro-optical cable (MEOC) to shore. The MEOC contains all electrical and optical links between the detector and the shore that are used for power distribution and data traffic. On shore, the MEOC is connected to the shore station from where the detector is operated. The shore station also houses the necessary computing power to process and store the data coming from the detector.

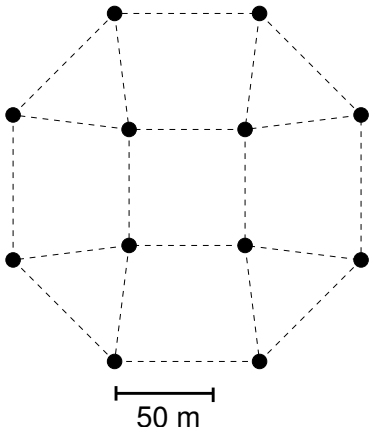

Figure 1.4: *The layout of the string positions on the sea bed. Each black circle represents the position of a detector string. The ground area of the detector is approximately 180 × 180 m^2.*

1.3 Data acquisition

The measurements of the arrival times and the number of Cherenkov photons on the PMTs in the detector are handled by the data acquisition (DAQ) system. The system initialises and operates the detector, and acquires and processes the PMT signals for offline reconstruction and analysis of the data. A schematic view of the DAQ system is shown in figure 1.5.

A photon that hits the photo-cathode of a PMT can liberate an electron with a probability equal to the PMT's quantum efficiency. The electron, referred to as a photo-electron (p.e.), induces an amplified electrical signal on the anode of the PMT. When the amplitude of this analogue signal crosses a certain voltage threshold, the signal is digitised by a front-end chip called analogue ring sampler (ARS) [11]. The threshold is applied to exclude small signals due to the dark current in the PMT. Its value is typically the equivalence of 0.3 p.e. At the moment of the threshold crossing, the ARS chip assigns a time stamp to the PMT signal. Timing information is provided by a local clock system in the LCM. The local clock system is synchronised with a 20 MHz master clock situated on shore. The ARS counts the number of clock pulses for a rather coarse timing (units of 25 ns), and uses a time-to-voltage converter (TVC) to interpolate between two subsequent clock pulses to achieve a more precise timing of about 0.2 ns accuracy. The ARS measures the charge contained in the PMT signal by integrating the anode current over a certain time interval, which is typically 25 ns [12]. The integrated charge is related to the amount of photo-electrons in the signal, and therefore a measure for the intensity of the

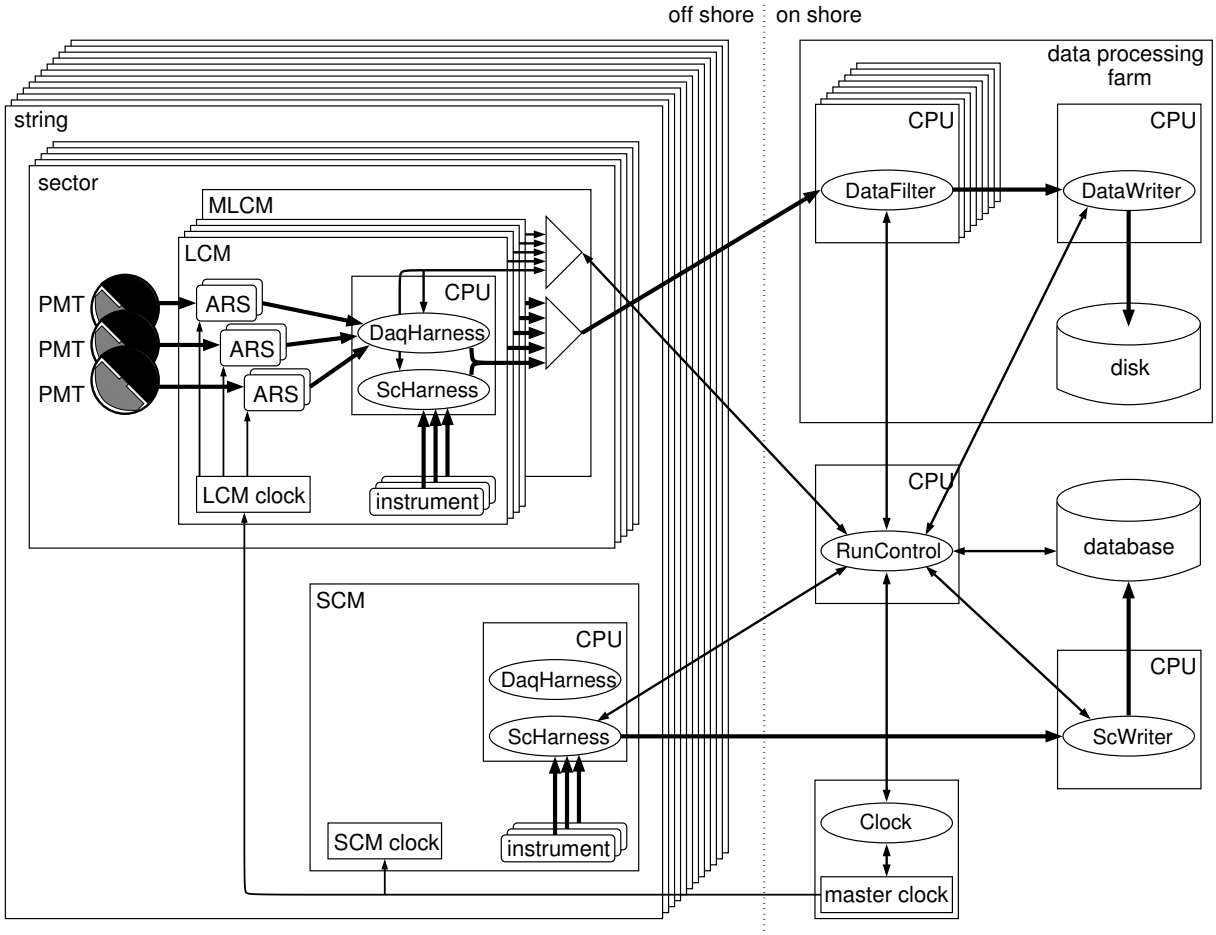

Figure 1.5: *A schematic view of the data acquisition system. The boxes represent hardware devices in the system, the ellipses software processes. The arrows indicate the exchange of information between the different devices and processes. The thick solid arrows show the flow of the raw data. Communication between processes is indicated with the thin solid arrows, as is the distribution of the clock signal.*

instantaneous radiation on the PMT. After digitisation of a signal, the ARS is inactive for a period of approximately 250 ns [13]. To reduce the effect of this dead time on the data taking, each PMT is read out by two ARS chips which alternately process the PMT signals.

The combined digital information on the time and charge of a PMT signal is referred to as a hit. The read-out of the ARS chips is performed by a field programmable gate array (FPGA), which arranges the hits from each ARS in the LCM into so-called data frames. A data frame contains all the hits produced by a specific ARS within a predefined time interval of typically 13 ms. The frames are sent as separate data packages to shore via the MLCM. The transmission of the frames is controlled by the DaqHarness program, which runs on the central processor (CPU) of the LCM. The processor uses a 100 Mbit/s Ethernet link for the connection to the MLCM. In the MLCM, the Ethernet links from all five LCMs in the sector are merged into a single 1 Gbit/s Ethernet link to shore. The

LCM processor also runs the ScHarness program, which controls and reads out the local power supply, PMT bases and various monitoring and calibration instruments present in the LCM (see section 1.6). Information from these devices, commonly referred to as slow control data, is transferred to shore via the same channel as the ARS data. The ScHarness program that runs on the processor in the SCM controls and reads the SPM and some calibration instruments in the BSS. The SCM processor is directly connected to shore with a 100 Mbit/s Ethernet link.

Except for the ARS threshold of 0.3 p.e., no selection of PMT signals is performed off shore. This means that all hits are sent to shore, a concept referred to as all-data-to-shore (ADTS). However, the amount of data produced in the detector is too large to store all data for off-line analysis (see section 1.4). Therefore, the ARS data are processed on shore by the DataFilter program. The DataFilter program incorporates a fast software algorithm that is designed to suppress background and find muon signals in the data. Only data samples that are possibly related to a muon signal are kept for off-line analysis, all other data are discarded (see section 1.5). In this way, the data output of the detector can be reduced significantly. To achieve real-time processing of the data, the DataFilter program runs on multiple processors. The set of processors is referred to as the data processing farm, and resides in the shore station. One processor in the farm runs the DataWriter program, which collects the output of all DataFilter processes. It organises these data according to their type, and stores them on disk in ROOT format [14]. The data acquired during different data taking runs are stored in separate files. These files are copied to a central computer centre elsewhere for permanent storage and easy access for off-line analysis. The slow control data coming from the detector are handled by the ScWriter program, which runs on a separate PC. It stores the data in a database that is located in the shore station.

The main user interface to the DAQ system is the RunControl program, which runs on a separate PC in the shore station. It controls the operation of the detector, including all processes in the system. For the synchronisation of the processes the RunControl uses a finite state machine that has been implemented using the CHSM programming language [15]. The organisation of the data and message traffic between the processes is done with Ligier [16], a software package based on ControlHost [17]. The RunControl program uses the database for the bookkeeping of detector settings and run information. Details on the RunControl program and the implementation of Ligier and the state machine can be found in [18].

All offshore and on-shore processors in the DAQ system are connected to an Ethernet switch fabric on shore. In this way, they constitute an Ethernet network. The Transmission Control Protocol and Internet Protocol (TCP/IP) are used for the transmission of data between processes. Each processor is identified by a unique IP address, which is used to route data through the network. This enables transparent communication between all processes in the system. The data transmission in the DAQ system is explained in more detail in chapter 2.

1.4 Background and data rate

The ANTARES detector will be built at a depth where no daylight penetrates. This provides an environment in which PMTs can be used to detect the relatively rare light. Unfortunately, the Cherenkov radiation from neutrino-induced muons is not the only light at the depth of the ANTARES site. Background light is produced by the decay of radioactive potassium (^{40}K), a trace element in sea water, and by bioluminescence. Another source of background light are energetic muons that originate from particle showers produced by cosmic ray interactions in the Earth's atmosphere above the detector. When their energies are sufficiently high, these muons can travel large distances and reach the detector from above. The water column above the detector acts as a shield, reducing the flux of downward going atmospheric muons to some extent. Still, the rate of atmospheric muons that produce detectable light in the detector amounts to a few hundreds per second [18].

Muons that travel upward in the detector can only be produced by neutrino interactions, as muons cannot penetrate the Earth*. Therefore the PMTs in the detector face downward. This reduces the sensitivity to background light from atmospheric muons and increases the sensitivity to neutrino-induced muons. Most upward going muons are produced by neutrinos that originate from cosmic ray interactions in the atmosphere on the other side of the Earth. For cosmic neutrino detection, these atmospheric neutrinos form an irreducible background. The rate of atmospheric neutrinos that produce detectable light in ANTARES is less than one per minute [18], which is several orders of magnitude smaller than that of atmospheric muons.

The hit counting rate of a PMT in the detector is predominantly due to background light produced by ^{40}K decay and bioluminescence. These processes cause mainly single hits with a charge that corresponds to one p.e. The counting rate of a PMT is commonly referred to as the singles rate. The contribution of ^{40}K decay to the singles rate can be considered constant and amounts to about 27 kHz [19]. The contribution of bioluminescence however exhibits large fluctuations in time. Measurements with a prototype detector have shown that the average singles rate can vary between 50 and 300 kHz over periods of just a few hours to many days [20]. Besides these relatively slow variations, bioluminescence also causes sporadic peaks in the singles rate of up to several MHz during periods of a few seconds.

In this work, a constant singles rate of 100 kHz is assumed. This is based on a rough estimate of the average rate measured with the prototype detector over a period of three months. Peaks in the singles rate due to bioluminescence are not considered. The data rate that corresponds to a singles rate of 100 kHz amounts to approximately 0.6 GByte/s for the whole detector. All these data are transferred to shore according to the ADTS concept.

*Although the muon range increases with increasing energy, it is limited to only a few tens of kilometres for the highest possible energies, see section 1.7.

1.5 Data processing

The data rate from the detector is reduced significantly by effectively removing hits due to ^{40}K decay and bioluminescence from the data. This is done on shore with a fast software algorithm that is used to process all data coming from the detector in real time. The algorithm searches for hits caused by a muon traversing the detector. These hits are related in time and position as a consequence of the properties of Cherenkov light emission (see section 1.1). These time-position correlations generally do not apply to hits caused by ^{40}K decay and bioluminescence. These processes are mostly uncorrelated and can therefore be considered as random background. Thus, a group of correlated hits may imply the presence of a muon signal in the data. Only data corresponding to a sufficient number of correlated hits are selected for off-line analysis, all other data are discarded. The resulting reduction of the data rate corresponds to a factor of at least 10^4. Since the algorithm mimics a standard hardware trigger as implemented in many high-energy physics experiments, it is commonly referred to as trigger algorithm. It is implemented in the DataFilter program, which runs on the data processing farm on shore (see section 1.3).

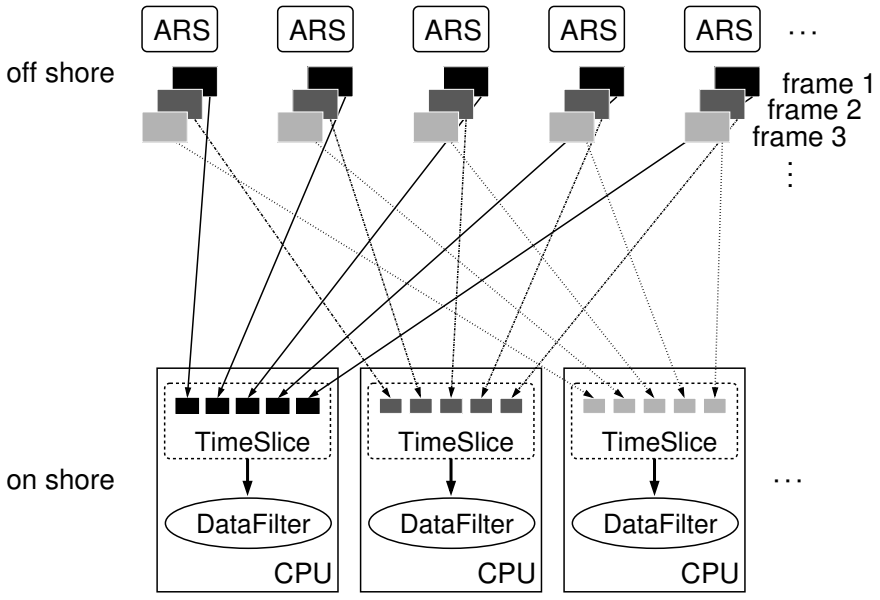

Figure 1.6: *A schematic view of the data collection on shore. All data frames that belong to a particular time window are sent to the same processor in the data processing farm. The DataFilter program that runs on this processor collects the frames. When all frames of the same time window have been collected, they are passed to the trigger algorithm. The complete set of frames is called a time slice.*

Off shore, the ARS data are organised in data frames. All frames that belong to the same time window are sent to the same processor in the processing farm. This is shown schematically in figure 1.6. The DataFilter program collects the frames, reconstructing the complete data set that was taken with the whole detector during the same 13 ms.

The program buffers the frames in a queue to handle transmission delays in the network. When all frames of a particular time window have been collected, they are passed to the trigger algorithm. The complete collection of frames is referred to as a time slice. The time and charge of all hits in the data are corrected using the known calibration of the detector.

The trigger algorithm first selects hits from the time slice that either form a local coincidence or have a large charge. This selection is based on the assumption that the simultaneous arrival of two (or more) photons on the same storey is more likely to be caused by a muon than by random background. A local coincidence consists of at least two hits that occur within 20 ns on two different PMTs in the same storey. This covers the case that two simultaneous photons on a storey are detected by different PMTs. The time window of 20 ns accommodates the difference in PMT positions, uncertainties in the time calibration and some light scattering. The detection of two coinciding photons by the same PMT generally results in a single hit with a charge that corresponds to 2 p.e. This is unlike random background hits, which are mainly produced by single photons and consequently have a charge that corresponds to a single p.e. Therefore, the algorithm selects hits with a large charge. The charge threshold for large hits corresponds to typically 3 p.e.[†]

Local coincidences and large hits selected by the algorithm are called level 1 or L1 hits. These hits consist of the time information of the coincidence or large hit, and the position of the storey on which it occurred. In the next step, the trigger algorithm searches for correlations between these L1 hits. This is based on causality, which is the time-position relation between hits in different parts of the detector due to unscattered Cherenkov light from the same muon path. Assuming that the muon is highly relativistic, the slowest possible speed for unscattered light is the group velocity of light in the sea water $v_g = c/n_g$. For two different L1 hits, causality then implies

$$|\Delta t| \leq \frac{n_g}{c} d \ , \tag{1.5}$$

where Δt is the time difference between the L1 hits, and d the three-dimensional distance between the corresponding storeys. The positions of the storeys are obtained from the calibration of the detector. An additional time window of 20 ns is taken into account to accommodate uncertainties in the storey positions, time calibration and some light scattering. Hits that satisfy equation 1.5 could have been produced by a muon travelling in any direction. A group of causally related L1 hits is referred to as a cluster.

In the final step of the hit selection, the algorithm only considers the L1 hits in a cluster. It searches for correlations between these hits with a more constrained causality relation, which is derived from the actual geometry of Cherenkov light emission. For this purpose, a loop over a certain number of predefined directions is implemented. These directions are arranged uniformly in the solid angle. The number of directions is typically 200, which corresponds to a mutual angular spacing of about 10 degrees. For each direction, the co-ordinate system of the ANTARES detector is rotated in such a way, that the z-axis of

[†]The threshold for selection of large hits was foreseen to be 2 p.e. However, it has been shown that many random background hits pass this threshold. This is due to the limited charge resolution of the PMT, which causes a considerable tail in the charge distribution [21].

the rotated system points along that direction. Consequently, the positions of the storeys acquire new co-ordinates in the rotated system. Then the assumption is made that the muon travels along the z-axis of the rotated system. In this way, the motion of the muon and the propagation of the emitted Cherenkov photons can be decoupled.

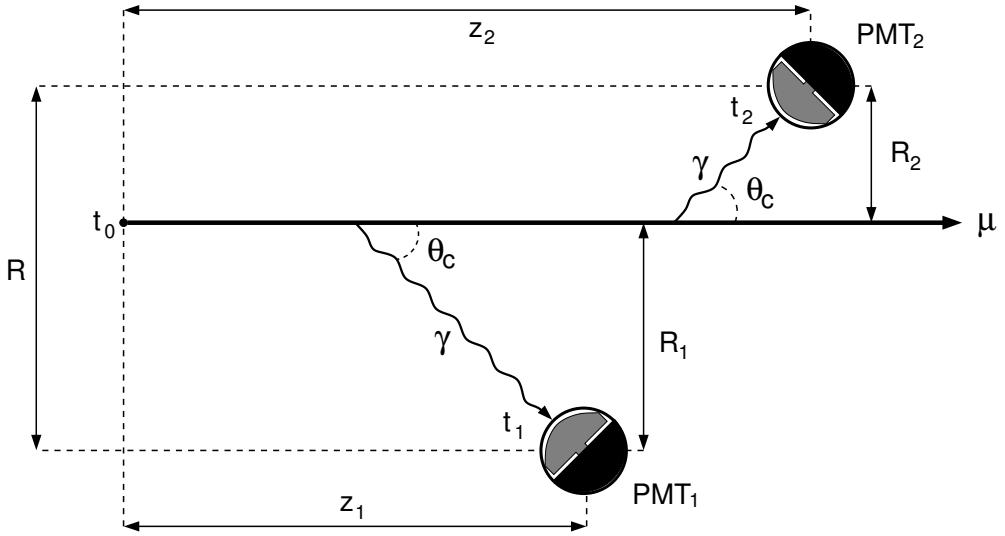

Figure 1.7: *The geometry of the Cherenkov light emission by a muon that travels in the z-direction. The Cherenkov photons are emitted under the Cherenkov angle θ_c, and can be detected by different PMTs along the muon path. The position of a PMT$_j$ can be expressed by the distance z_j to the muon position at time t_0, and the distance of closest approach R_j to the muon path.*

Figure 1.7 depicts the geometry of Cherenkov light emission by a muon that travels along the z-axis. According to the figure, the expected arrival time t_j of a Cherenkov photon on PMT$_j$ is given by

$$t_j = t_0 + \frac{1}{c}\left(z_j - \frac{R_j}{\tan\theta_c}\right) + \frac{n_g}{c}\frac{R_j}{\sin\theta_c} \ , \tag{1.6}$$

where t_0 is some reference time, c is the velocity of the muon, θ_c is the Cherenkov angle, z_j is the difference between the z-positions of the point at t_0 and PMT$_j$, and R_j is the distance of closest approach between PMT$_j$ and the muon path. The second term in the equation is the time that the muon needs to travel from the position at t_0 to the point where the detected photons are emitted. The third term represents the time these photons need to reach the PMT.

The difference between the arrival times t_1 and t_2 of two Cherenkov photons can then be written as

$$t_2 - t_1 = \frac{z_2 - z_1}{c} + \frac{R_2 - R_1}{c}\tan\theta_c \ , \tag{1.7}$$

where the approximation $\cos\theta_c = 1/n_g$ is used[‡]. Since only the direction of the muon path

[‡]For a muon with velocity c, the Cherenkov angle is actually given by $\cos\theta_c = 1/n$, with n the phase refractive index of the sea water, see section 1.1.2.

is assumed, and no assumption on its position is made, the value of the factor $(R_2 - R_1)$ is unknown. However, the absolute value of this factor is maximal when the muon crosses either PMT_1 or PMT_2. This maximum value is defined by the distance R between the projections of the two PMT positions on a plane perpendicular to the direction of the muon, as is shown in figure 1.7. Thus, two L1 hits within a cluster are assumed to be correlated if their time difference obeys the modified causality relation

$$\frac{z_2 - z_1}{c} - \frac{R}{c}\tan\theta_c \leq t_2 - t_1 \leq \frac{z_2 - z_1}{c} + \frac{R}{c}\tan\theta_c \ . \tag{1.8}$$

This relation is more stringent than the one in equation 1.5, since $R\tan\theta_c$ is always smaller than $n_g d$. Again, an extra time window of 20 ns is applied to account for calibration uncertainties and light scattering.

When the trigger algorithm finds a sufficient number of correlated L1 hits within a cluster in any of the directions, it is assumed that a muon signal is present in the data. From this cluster a physics event is constructed, which is stored on disk for off-line analysis. Besides the ARS hits that are directly related to the cluster, a physics event also contains all ARS hits within a time window of about 2 μs around the time of the cluster. This is done to include hits that are possibly related to a muon signal, but are not a local coincidence or a large hit. The window of 2 μs corresponds to the maximum time that a muon needs to travel through the detector. Different clusters that are found within this time window are merged into a single physics event. They will be disentangled in the off-line analysis.

The trigger algorithm, as explained above, is very successful in the suppression of random background hits. However, due to accidental coincidences, some of these hits survive all hit selections and are considered as a physics event. The rate with which the algorithm finds such background events increases rapidly with the singles rate [21]. As the singles rate in the detector is relatively high, two cuts are applied in the trigger algorithm in addition to the described hit selection. Since background events produce small clusters [21], one cut involves a minimum number of L1 hits that is required for a cluster to qualify as physics event. This cut is adjustable and is typically set to 5. Another feature of background events is that the hits in their clusters in general have large mutual distances [21]. In the case of a muon signal however, most correlated hits are expected to occur within a limited radius around the muon path. A second cut is therefore applied to the transverse distance between two L1 hits (R in equation 1.8). If this distance exceeds a specified maximum, it is assumed that the two hits are not correlated. This cut is referred to as the maximum transverse distance R_{max}, and can be adjusted as well. A reasonable estimate of R_{max} can be derived from equation 1.4, and corresponds to a photon path length of about twice the absorption length λ_{abs}. For a singles rate of 100 kHz, a minimum cluster size of 5 and a maximum transverse distance of 90 m are sufficient to suppress the rate of random background events to about 0.1 Hz [22]. Under these circumstances, the number of farm processors that is necessary to process the data in real time is of the order of 10[§].

Of course, application of cuts inevitably leads to loss of muon signals. The degree of signal loss can be characterised by the efficiency with which the trigger algorithm finds

[§]This estimate is based on a processor speed of 2.2 GHz.

muon signals. It strongly depends on the energy of the muon, and on the values of the cuts. For the cuts mentioned above, the efficiency of the algorithm for muons that produce at least 6 detected photons in the detector is about 10% for muon energies of the order of 100 GeV, and increases to approximately 65% for energies of the order of 10^7 GeV [22]. The large majority of muons that produce light in the detector are atmospheric muons (see section 1.4). The rate with which the algorithm finds these muons is about 5 Hz [23], which largely exceeds the rate of background events. With a typical physics event size of approximately 3 kByte [21], the reduction in data rate is then a factor of about 4×10^4.

Since their signals are similar, atmospheric and neutrino-induced muons are treated equally in the trigger algorithm. In the off-line data analysis, dedicated software is used to reconstruct the muon signals from the physics events stored by the trigger algorithm. Only after the direction and energy of the muons are determined is discrimination between atmospheric and neutrino-induced muons possible. The ultimate goal of the analysis is to find neutrino-induced muons and determine the direction and energy of the incident neutrinos.

1.6 Detector calibration

For the accurate time and charge measurements of the PMT signals, the detector needs to be calibrated. An internal timing calibration can be performed with the clock system to measure the signal transit times between the on-shore master clock and each LCM and SCM slave clock. In this way the relative time offsets between the LCM and SCM clocks, caused by the difference in optical path lengths in the distribution of the clock signal, can be obtained. The transit time of the PMTs can be measured by firing the LED inside the OMs (see figure 1.2) and recording both the time of the LED flash and the resulting PMT signal with the ARS. In general, PMT signals are uncorrelated with respect to the clock signal. This results in a uniform distribution of the TVC output of the ARS, from which the slope and the offset of the TVC can be determined.

For an overall calibration of the PMT and clock system, two devices are available. The first is a so-called optical beacon that consists of a set of blue LEDs. In each string four storeys are equipped with such a beacon. It can illuminate a number of OMs on neighbouring strings. The other device is a laser beacon that is located in the BSS of the Instrumentation Line[¶]. It can illuminate a large part of the detector. The overall timing accuracy is expected to be around 1 ns [8], which is of the order of the transit time spread of the PMTs (see section 1.2).

Absolute timing of events is realised by interfacing the on-shore master clock system to the Global Positioning System (GPS) clock, giving an accuracy of the order of a millisecond.

The charge calibration of the PMTs is obtained by measuring random background that consists mainly of single photo-electron signals, and by varying the intensity of the

[¶]In addition to the detector strings described, an additional string called Instrumentation Line is deployed. This string is equipped with devices that measure and monitor environmental parameters at the detector site like pressure, salinity and temperature of the sea water, water current, sound velocity and light attenuation.

optical beacons.

Precise positions of the OMs in the detector are necessary for the trigger and reconstruction algorithms. Since the detector strings are not rigid structures, the shape of the strings and the position and orientation of the OMs are influenced by currents in the sea water. Therefore regular monitoring of the OM positions is needed.

In each LCM a biaxial tilt meter and a compass are located to measure the pitch, roll and heading of the storey. In the BSS of each string a transmitter is located which can emit acoustic signals. These signals are detected by hydro-phones mounted on 5 storeys and the BSS of each string. By measuring the propagation times of the acoustic signals, the relative positions of the hydro-phones can be determined. The tilt meter, compass and acoustic system data are used to reconstruct the shape and torsion of the string. From these, the relative positions of the OMs are obtained with an expected precision of about 10 cm [8].

The absolute geographical location of the detector is determined with an accuracy of a few metres during string deployment using GPS positioning of the ship, acoustic position monitoring below the ship and depth measurements [8]. The absolute orientation of the detector with respect to the sky is determined using four reference acoustic beacons placed on the sea floor around the detector. The location of these beacons is measured with respect to the detector and with respect to the GPS position of the ship at the surface. The absolute orientation is determined with a precision of better than 0.3 degrees, which is the expected angular resolution of the ANTARES detector (see section 1.7).

Accurate performance of the acoustic positioning systems requires knowledge of the sound velocity at the site, which is measured by five sound velocimeters placed at various positions in the detector.

1.7 Angular and energy resolution

The energy and direction of a muon emerging from a charged current neutrino interaction are closely related to the energy and direction of the parent neutrino, as explained in section 1.1.1. The accuracies with which these quantities of the muon are measured determine the overall angular and energy resolution of the neutrino telescope.

The distance that a muon can travel in sea water as a function of its energy is shown in figure 1.8. For muon energies below a few hundreds of GeV, the energy loss of a muon in sea water is primarily due to ionisation. It is approximately constant and amounts to about 0.2 GeV/m [24]. This means that the muon range is proportional to the muon energy and is limited to a few hundreds of metres. This can be used to estimate the energy of the muon from the measured length of its path in the detector. For the muon path to be reconstructible, a minimum number of different PMTs that detect the Cherenkov signal is required. This translates into a threshold for the muon energy of the order of 10 GeV [1].

The range of the muon increases with its energy. For muon energies above a few TeV, radiative processes like bremsstrahlung and pair production dominate the energy loss. In this regime, the average energy loss of a muon is approximately proportional

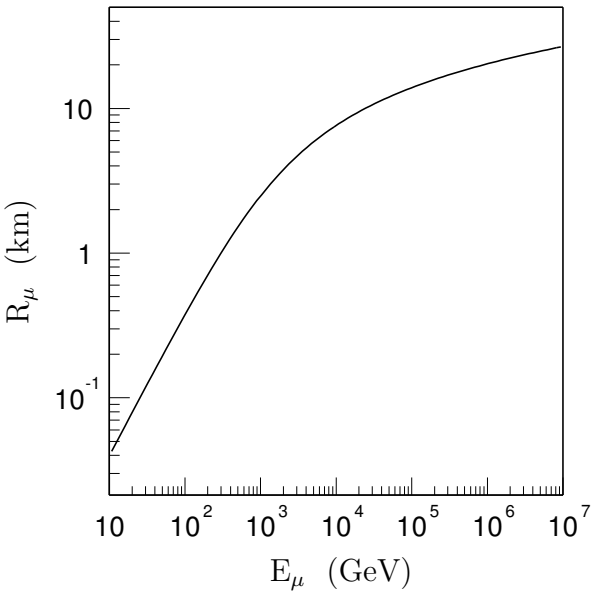

Figure 1.8: *Approximate range of the muon R_μ in sea water as function of its energy E_μ, extracted from [24].*

to its energy [24], which implies that its range is proportional to the logarithm of its energy. The particle showers produced along the muon path also emit Cherenkov light. The amount of detected Cherenkov radiation is a measure for the average energy loss of the muon. From this, the muon energy can be determined. The opacity of the Earth to upward going neutrinos with energies in excess of 10 PeV results in an upper limit on the sensitivity of the detector [1].

Monte Carlo studies have shown that the muon energy resolution is approximately a factor 2 at 1 TeV, improving to a factor 1.6 at an energy of 10 PeV [25]. For neutrino interactions near or inside the instrumented detector volume, the Cherenkov yield of the hadronic shower at the interaction point provides additional information on the neutrino energy [1].

The search for point sources with ANTARES requires a good angular resolution of the detector. It depends on several factors like the muon scattering angle in the interaction, multiple scattering of the muon in the medium, light dispersion, absorption and scattering in the sea water, alignment of the PMTs, timing of the read-out system and quality of the reconstruction software. Monte Carlo studies have shown that for neutrino energies below approximately 10 TeV the angular resolution is limited by the scattering angle of the muon at the neutrino interaction vertex. Above 10 TeV the resolution is limited by the timing and alignment accuracy of the detector. For these energies the angular resolution is better than 0.3 degrees [26].

1.8 Physics and detector simulation

To study the response of the ANTARES detector to the physics signals caused by high-energy neutrino interactions, several software packages are used to simulate the underlying processes. A detailed description of these simulation tools is given in [7, 26]. Basically,

the simulation consists of three steps. First, the interactions from which muons and other charged particles emerge are simulated. Then, the produced particles are propagated from the interaction point to a predefined distance from the instrumented detector volume. Finally, the simulation of the emission, propagation and detection of the Cherenkov light that the particles produce as they pass through the detector volume, is performed. The result of the full simulation is a set of hits on different PMTs in the detector, which reflects the response of the detector. Besides giving insight in the behaviour of the detector, the output of the simulation is also used to study the performance of the trigger and the reconstruction software.

1.8.1 Atmospheric muons

As mentioned in sections 1.4 and 1.5, atmospheric muons are a source of correlated background light in the detector. A full simulation of the energetic air showers in which they are produced is performed using the CORSIKA package [27]. Protons and helium, nitrogen, magnesium and iron nuclei are considered as primary cosmic ray particles in the energy range from 1 TeV to 100 PeV [28]. The observed energy spectrum is assumed for the flux of each primary particle, and only the hemisphere above the detector is taken into account. CORSIKA also simulates the propagation of the produced muons to the sea level. From there, the muon propagation through the sea water to the surface of the so-called can (see below) is done with a modified version of MUSIC [29]. This tool simulates all relevant energy loss processes of the muon, and the deviations in the muon direction due to multiple scattering.

The can is a cylindrical volume around the instrumented detector volume in which the simulation of the Cherenkov light production and propagation is performed. The can extends typically a few absorption lengths beyond the instrumented volume, and has a size of about 0.1 km^3.

1.8.2 Neutrino interactions

Interactions of neutrinos with energies between 10 and 10^8 GeV are simulated in a large volume around the detector with the GENHEN package [7]. The size of this volume is defined by the maximal muon range associated with a given energy interval, and is typically 8×10^4 km^3 for an upper limit of 10^8 GeV. The energy spectrum of the neutrinos is generally assumed to follow an $E^{-\gamma}$ law, with values of γ between 1 and 3. Only neutrinos from the hemisphere below the detector are considered. If the neutrino interaction takes place inside the can, all particles produced in the interaction are taken into account for the Cherenkov light emission simulation. If the interaction is outside the can, only the emerging muon is propagated to the can surface.

1.8.3 Cherenkov emission

The Cherenkov light emission, propagation and detection is only simulated for particles that reach the can, or are produced inside it. For muons, this simulation is done with the KM3 package [30]. It incorporates the main features of Cherenkov light emission

(see section 1.1.2), and only considers light in the PMT's sensitive wavelength range (see section 1.2). The measured properties of the sea water at the ANTARES site are used to simulate the dispersion, absorption and scattering of the Cherenkov photons. These processes influence the intensities and arrival times of the Cherenkov light on the PMTs. The simulation of the photon detection includes the transparency of the glass sphere and optical gel in the OM, and the effective photo-cathode area, quantum efficiency, transit time spread and charge resolution of the PMT. Eventually, the digitisation of the PMT signals by the ARSs is simulated. For the propagation of the muon through the can, KM3 uses MUSIC.

The propagation of particles other than the muon are simulated with GEASIM [31], a software tool based on GEANT3 [32]. It performs full tracking of the particles through the can volume, simulating all relevant physics processes. The simulation of the Cherenkov light emission and the detector hardware is similar to KM3, except for scattering of the Cherenkov photons in the sea water, which is not simulated with GEASIM.

The output of both KM3 and GEASIM contains a list of hits that represent the arrival times and the number of Cherenkov photons that would have been detected by different PMTs in the detector. Generally, simulation of hits due to random background is also performed. These hits are generated randomly in time at a fixed rate of 100 kHz, and have a charge that typically corresponds to a single p.e. They are added to the list of hits due to Cherenkov photons.

Chapter 2

The data transmission system

The data acquisition (DAQ) system of ANTARES has been developed primarily to acquire and process the signals of the photo-multiplier tubes (PMTs) in the detector. Each PMT signal that crosses a certain amplitude threshold is digitised by the front-end electronics in the local control module (LCM). No additional signal selection is performed off-shore, all digitised signals are sent to shore according to the all-data-to-shore (ADTS) concept. The average counting rate of a PMT is expected to be about 100 kHz, which results in a data rate of approximately 0.6 GByte/s for the whole detector. Therefore, a high bandwidth is required for the transmission of the data to shore. This is achieved by a fibre-optics system that uses dense wavelength division multiplexing (DWDM) in combination with Gigabit Ethernet (GbE).

In this chapter a brief description of the data transmission system in ANTARES is given. The concept of DWDM is explained, and measurements carried out on a DWDM multiplexer and demultiplexer are described. Finally, a brief description of the GbE standard is presented together with the results of measurements of the data transmission error rate.

2.1 Data transmission

Between the detector and the shore, two data flows can be distinguished in the DAQ system. The first is the flow of control and command messages that are sent from shore to the detector. The purpose of these messages is to initialise and configure the different processes, sensors and instruments in the detector. The second data flow is in the opposite direction, from the detector to the shore. It consists of measurement and status data from the sensors and instruments in the detector. Data concerning the readout of the PMTs are specifically referred to as ARS data (see chapter 1). Data concerning other hardware devices and calibration instruments, are commonly referred to as slow control (SC) data. The Transmission Control Protocol and Internet Protocol (TCP/IP) are used for the communication between the processes in the system. TCP/IP defines the format of the packages in which the data are sent over the network, and implements a handshaking mechanism between the source and destination. The physical transmission of the data packages is defined by the Ethernet standard.

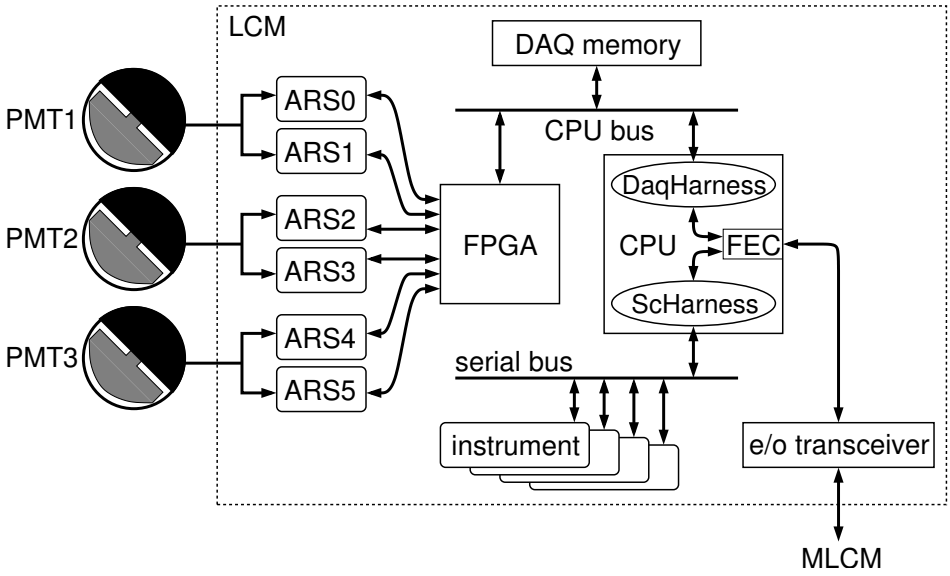

Figure 2.1: *A schematic view of the DAQ system in the LCM. The PMT signals are digitised by the ARS chips. A field programmable gate array does the readout of the ARSs. It transfers the ARS data to the DAQ memory where they are buffered. The DaqHarness process that runs on the LCM processor transfers the ARS data from the DAQ memory to the shore via the MLCM using a Fast Ethernet controller. The slow control data from the instruments linked to the LCM are handled by the ScHarness process that runs on the same CPU. Control messages coming from shore via the MLCM are passed to the DaqHarness and ScHarness through the Fast Ethernet controller.*

2.1.1 Data acquisition in the LCM

Figure 2.1 shows a schematic view of the data acquisition in the LCM. The signals of each PMT are processed by two analogue ring sampler (ARS) chips. The chips assign a time stamp to the PMT signals and digitise the charge. The serial outputs of all 6 ARS chips are connected to a field programmable gate array (FPGA), which performs the ARS readout. The asynchronously arriving ARS data are decoded in the FPGA and transferred to the DAQ memory where they are buffered. The data are organised according to ARS identifier and data type. The DAQ memory is connected to the central processing unit (CPU) of the LCM via the CPU bus. The DaqHarness process that runs on the CPU transfers the ARS data from the memory to shore via the master local control module (MLCM) using a Fast Ethernet controller (FEC). The data are routed through the network according to the IP address of their destination on shore. Fast Ethernet operates at a data transmission rate of 100 Mbit/s. The electrical signals from the FEC are converted into optical signals by an electro-optical (e/o) transceiver*. The link to the MLCM uses a single bidirectional optical fibre in the electro-mechanical cable (EMC).

Several devices in the LCM like the power supply, compass and tilt meter are connected to the CPU through a serial port. The data from these instruments are collected by the

*The combination of a transmitter and receiver is commonly referred to as transceiver.

ScHarness process which runs on the same CPU . The process transfers these data to shore via the same channel as the ARS data.

Command messages coming from shore are passed to the DaqHarness and ScHarness processes through the FEC. The routing of these messages through the network is based on the IP address of the CPU. The bidirectional fibre between the LCM and MLCM accommodates the data traffic in both directions.

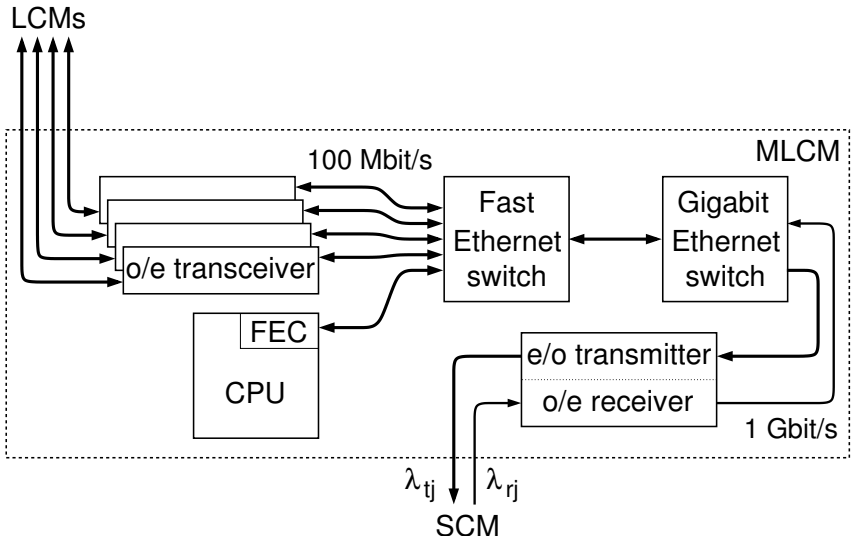

Figure 2.2: *A schematic view of the DAQ system in the MLCM. The MLCM has the same functionality as the LCM. In addition, it contains an Ethernet switch which merges the Fast Ethernet links from all five LCMs in the sector into a single GbE link (1 Gbit/s) to shore. The optical transmitter in each MLCM uses a unique wavelength λ_{tj}. Command messages are sent from shore to the MLCM using the same wavelength λ_{rj}. They pass the MLCM switch and are distributed to the LCMs.*

2.1.2 The MLCM switch

A schematic view of the DAQ system in the MLCM is shown in figure 2.2. The MLCM has the same functionality as the LCM (see figure 2.1). The ARS and SC data from the local DAQ are passed from the FEC of the MLCM processor to the MLCM Ethernet switch. In addition, the optical signals from the four other LCMs in the sector are converted into electrical signals and then passed to the switch. The switch is a combination of a Fast Ethernet switch and a GbE switch. It merges the five Fast Ethernet links into a single GbE link, which operates at a data transmission rate of 1 Gbit/s. The gigabit signals are converted into optical signals by an electro-optical transmitter, and transferred to shore via the string control module (SCM). The transmitter uses a unique wavelength λ_{tj}. The link to the SCM uses a unidirectional optical fibre in the EMC.

Command messages coming from shore via the SCM travel the reverse path over a separate unidirectional fibre, and are distributed to the LCMs in the sector by the same switch. The wavelength λ_{rj} that is used for the connection from shore to the MLCM

is chosen to be the same as the transmitter wavelength λ_{tj}. Hence, each MLCM (and therefore each sector) inside a detector string is uniquely defined by this wavelength.

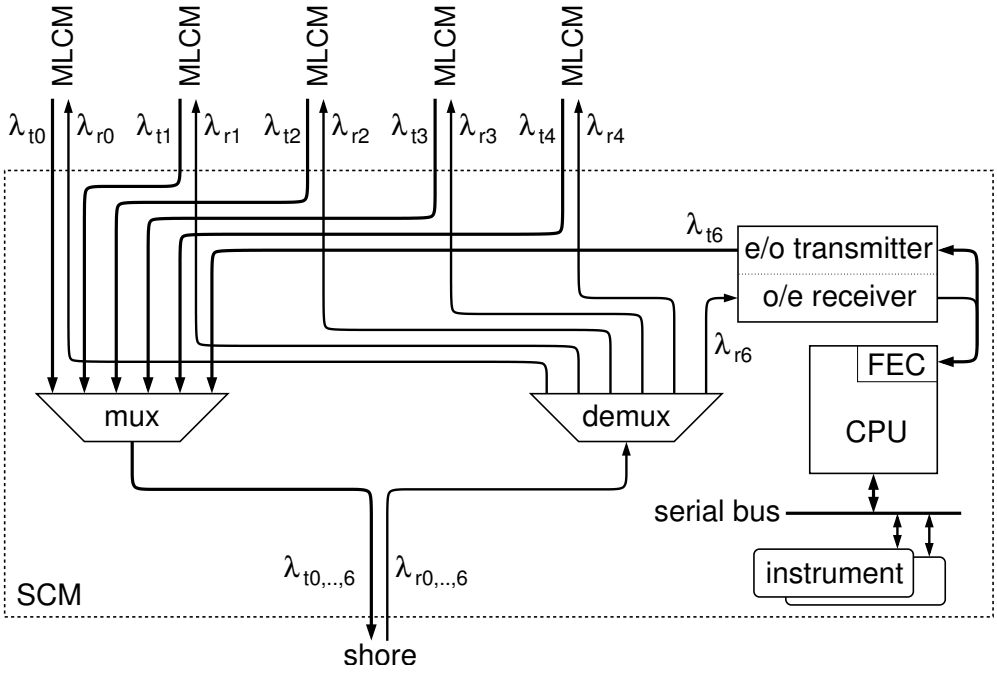

Figure 2.3: *A schematic view of the DWDM signal multiplexing and demultiplexing in the SCM. The signals from the five MLCMs in the string, each operating at a unique wavelength λ_{tj}, are combined into a single optical fibre to shore by a multiplexer (mux). The slow control signals from the SCM are multiplexed into a sixth wavelength channel. Signals coming from shore are split up into different fibres using a demultiplexer (demux). The destination of these signals, either one of the MLCMs or the SCM, is identified by the wavelength λ_{rj}.*

2.1.3 Signal (de)multiplexing in the SCM

To increase the bandwidth of the fibres in the main electro-optical cable (MEOC), dense wavelength division multiplexing (DWDM) is used. A schematic view of the DWDM system in the SCM is shown in figure 2.3. A passive optical device called multiplexer (mux in figure 2.3) combines the optical signals coming from the five MLCMs in the string into a single unidirectional fibre to shore. Each MLCM is then identified by its unique wavelength λ_{tj}. The data link of the slow control in the SCM is multiplexed into a sixth wavelength channel.

To avoid crosstalk between the signals in the two opposite directions, command data for the string are sent to the detector through a separate unidirectional fibre. In this case, the MLCMs and the SCM are then identified by the unique wavelengths λ_{rj}. As is explained above, the wavelengths are chosen such that $\lambda_{tj} = \lambda_{rj}$ for each MLCM and the SCM. An optical demultiplexer (demux in figure 2.3) in the SCM is used to split up the different wavelengths into separate fibres to the MLCMs.

For each string, the unidirectionality of the data transmission requires two fibres in the MEOC between the shore and the junction box (JB), between the JB and the SCM, and between the SCM and each MLCM.

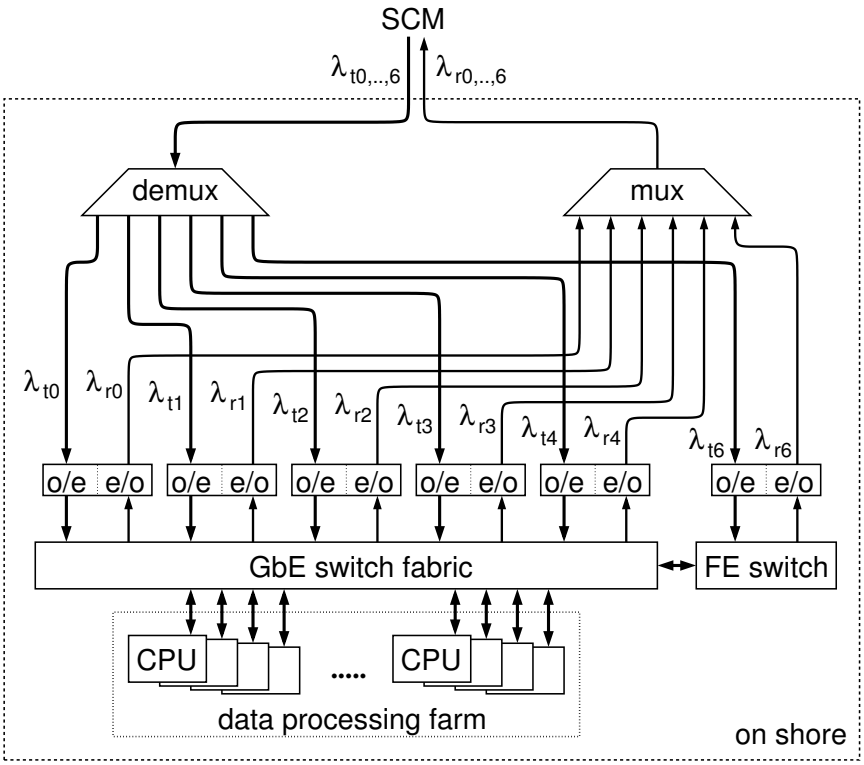

Figure 2.4: *A schematic view of the signal handling on shore for a single string. The multiplexed MLCM signals coming from the detector are demultiplexed and passed to a GbE switch fabric. The main purpose of the switch fabric is to route the ARS data to the CPUs in the data processing farm. The data from the SCM are first passed to a Fast Ethernet (FE) switch. Command messages pass the same switch fabric and are then multiplexed into a single fibre to the detector. The switch fabric accommodates all CPUs in the detector and on shore.*

2.1.4 Signal handling on shore

Figure 2.4 shows a schematic view of the signal handling on shore for a single string. The optical signals coming from the detector are demultiplexed and the data from the MLCMs are passed to a GbE switch fabric. The main purpose of the switch fabric is to route the ARS data to the software trigger processes that run on the data processing farm (see chapter 1). The data from the SCM are first passed to a Fast Ethernet switch and then upgraded to GbE.

Command messages are routed to the LCMs through the same switch fabric. Each of the optical transmitters is matched with one of the MLCMs or the SCM in the string using its specific wavelength λ_{rj}. All signals for a string are multiplexed into a single fibre

to the SCM. The transmission of data between the detector and the shore is identical for each string. The switch fabric accommodates all CPUs in the detector and on shore.

2.2 Dense wavelength division multiplexing

Dense wavelength division multiplexing (DWDM) is used to increase the bandwidth of a single optical fibre. It relies on the principle that a single fibre can carry several wavelengths simultaneously without mutual interference. The type of fibre that is used for the data transmission between the detector and the shore is that of a standard telecommunication cable. It supports wavelengths in the range from 1535 nm to 1570 nm. Each string uses a pair of these fibres for the connection to the shore. Each fibre accommodates the data traffic in one direction. As explained in the previous section, the data links of the five MLCMs and the SCM in the same string are carried by a single fibre. The six corresponding wavelengths must therefore be fitted into the operating wavelength window of the fibre.

The International Telecommunication Union (ITU) [33] has defined a grid of standardised wavelengths, of which ANTARES uses eight. The selected ITU wavelengths are spaced by 400 GHz (approximately 3.2 nm). Each wavelength represents a data link within a fibre. The transmitters in the MLCMs and in the SCM are set to one of these wavelengths. The wavelengths and the corresponding data links are shown in table 2.1. The wavelength labels in the table match those in figures 2.3 and 2.4.

wavelength label	ITU value (nm)	data link (rate)
$\lambda_{t0}, \lambda_{r0}$	1560.61	MLCM 0 (1 Gbit/s)
$\lambda_{t1}, \lambda_{r1}$	1557.36	MLCM 1 (1 Gbit/s)
$\lambda_{t2}, \lambda_{r2}$	1554.13	MLCM 2 (1 Gbit/s)
$\lambda_{t3}, \lambda_{r3}$	1550.92	MLCM 3 (1 Gbit/s)
$\lambda_{t4}, \lambda_{r4}$	1547.72	MLCM 4 (1 Gbit/s)
$\lambda_{t5}, \lambda_{r5}$	1544.53	spare channel
$\lambda_{t6}, \lambda_{r6}$	1541.35	SCM (100 Mbit/s)
$\lambda_{t7}, \lambda_{r7}$	1538.19	spare channel

Table 2.1: *The eight ITU wavelengths that are used in ANTARES [34]. The labels in the first column correspond to the figures in the previous sections.*

2.2.1 DWDM components

A simplistic scheme of the DWDM data transmission from a detector string to the shore is shown in figure 2.5. The active components of the data transfer are the optical transmitters and receivers. In between these, the network consists only of passive components like the fibre, multiplexer, demultiplexer and various submarine connectors.

The optical transmitter consists of an internally cooled distributed feedback (DFB) laser. When modulated, it has a spectral width of approximately 0.2 nm. Wavelength

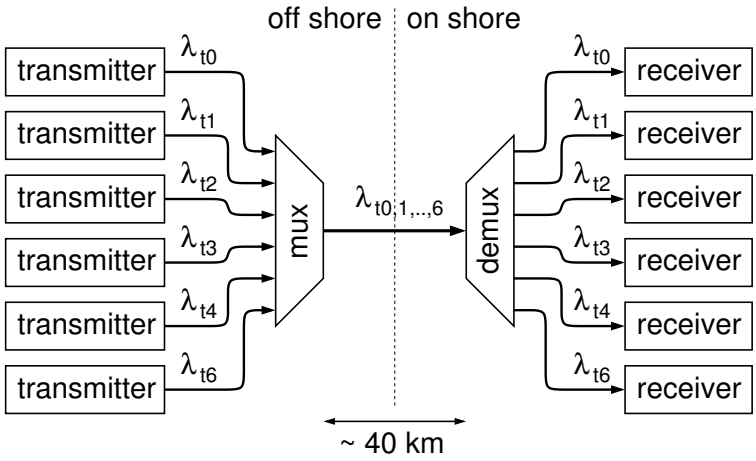

Figure 2.5: *A simplistic scheme of the DWDM data transmission from the detector to the shore for a single string. The signals from the transmitters are multiplexed off shore into a single fibre. On shore, the signals are demultiplexed and passed to the receivers.*

instability of the laser due to temperature fluctuations is kept within 0.1 nm. Over time, the laser wavelength may drift due to ageing effects. For periods of up to ten years, the wavelength drift is expected to be less than 0.1 nm. These effects need to be accommodated into an overall operating window for the wavelength of the laser. For an expected system life-time of ten years, a safe estimate for the operating window is then ±0.3 nm around the ITU wavelength [35]. The laser is operated at an output power level[†] of about 6 dBm. The optical receiver that is used consists of an avalanche photo diode (APD), which is a semiconductor radiation sensor. It is sensitive to the complete wavelength range used, and its power sensitivity is typically -30 dBm [8].

Both the multiplexer and demultiplexer, also referred to as filters, are passive optical devices. They perform no amplification or modulation on the signals that pass them. Around each ITU wavelength, they have a certain wavelength band in which the signal power is transmitted with minimal loss. The multiplexer combines the signals from its multiple input fibres into a single output fibre. Each of the input fibres carries a single ITU wavelength that identifies the signal source. The demultiplexer is used to extract the different wavelengths from the single input fibre into multiple output fibres. The signal in each separate output fibre corresponds to one source. After demultiplexing, the signals are passed to the receivers. The same scheme is used for the DWDM data transmission in the opposite direction, from the shore to the detector.

[†]Absolute power measurements are expressed in units of decibels referred to one milliwatt, dBm:

$$P\ (dBm) \equiv 10\ \log_{10}\left(\frac{P}{1\ mW}\right)\ .$$

Relative power measurements are expressed in units of decibels, dB:

$$\Delta P\ (dB) \equiv 10\ \log_{10}\left(\frac{P_{out}}{P_{in}}\right)\ .$$

The wavelength stability of the passive components in the network is intrinsically very good [35]. The sensitivity of the optical receivers can safely be considered as wavelength independent. The stability of the laser is therefore the critical factor in the long term system performance. Consequently, the transmission bands of the multiplexer and demultiplexer have to be matched with the operating windows of the lasers.

2.2.2 Characteristics of the optical (de)multiplexer

Some specific quantities are used to characterise the DWDM filters and to determine if they satisfy the system requirements. A detailed description of these quantities can be found for instance in reference [36].

The channel through which a signal with a certain ITU wavelength is routed in a DWDM filter, is referred to as a filter channel. In figure 2.6 an example of the transmission band of a filter channel for a specific ITU wavelength is shown. The ITU wavelengths of the adjacent filter channels are also depicted. The shaded areas around the ITU values indicate the operating windows of the lasers. The power level at which a signal passes the (de)multiplexer without attenuation is labelled as 0 dB loss line.

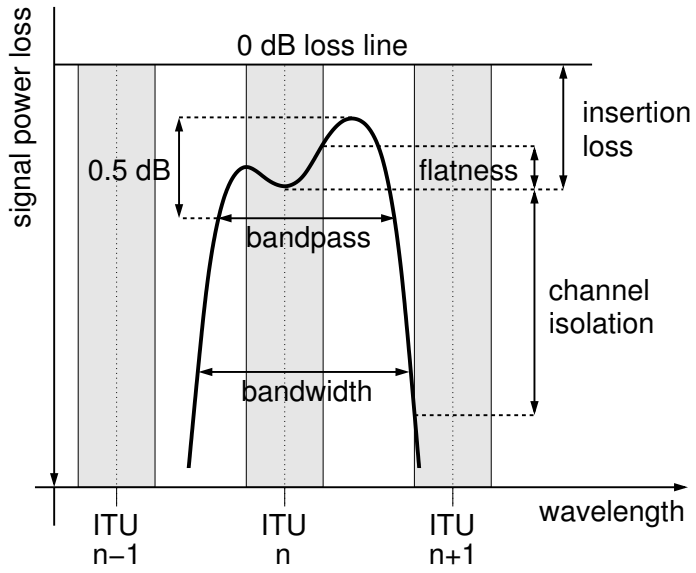

Figure 2.6: *An example of a (de)multiplexer transmission band around a specific ITU wavelength. The adjacent ITU wavelengths are shown as well. The shaded areas around the ITU wavelengths represent the operating windows of the lasers.*

The bandwidth of a filter channel is defined as the spectral range of its transmission band over which the transmission of the signal exceeds some stated power value. The bandwidth over which the power loss is acceptable for transmission purposes, is commonly referred to as the bandpass. The bandpass is taken at 0.5 or 1.0 dB loss with respect to the maximum transmission power of the filter channel, as is shown in figure 2.6. It should

at least cover the wavelengths in the laser operating window. Otherwise, the loss of laser power may be arbitrarily large.

The insertion loss of a filter channel is defined as the difference between the input and output power of the signal with the corresponding ITU wavelength. As will be described in section 2.3, the power loss of the optical signal has to be restricted for a reliable data transmission. It has been estimated that a maximum total power loss of about 26 dB is allowed in the network between an MLCM and the shore [8]. This power budget takes into account an insertion loss of 3.6 dB for each filter channel. The insertion loss is taken as the largest power loss in the bandpass within the laser operating window, see figure 2.6.

The edges of the transmission bands of the filter channels are not infinitely steep. Therefore, the transmission band of a particular channel may show overlap with neighbouring ITU wavelengths. This means, that part of the signal power from adjacent channels is transmitted into this particular channel. Since the receivers are sensitive to a large wavelength range, this could cause interference. This so-called crosstalk is of course undesirable. The transmission band of each channel must therefore be narrow enough to suppress signals from adjacent filter channels sufficiently. This is referred to as channel isolation. It is determined at the worst-case conditions, which occur at the edges of the laser operating window, as is shown in figure 2.6. It has been estimated that a channel isolation of at least 25 dB is required.

The flatness of the transmission band is the difference between the minimum and maximum power of the bandpass within the laser operating window. It gives information about the possible variations in the transmitted power. Generally, the flatness should be smaller than 0.5 dB.

2.2.3 Measurements on the DWDM (de)multiplexer

To determine whether the filter characteristics comply with the system requirements stated in section 2.2.2, measurements on a multiplexer and demultiplexer were carried out. To mimic the data transmission in the detector, the multiplexer and demultiplexer were connected in series. The transmission band of the filters was measured for each ITU wavelength. From these measurements, all relevant characteristics of the filter channels could be determined.

Test set-up

The set-up for the measurements is shown schematically in figure 2.7. A tunable laser (TuLa) is used as signal source. The output wavelength of this device can be varied. It is used to step through the DWDM wavelength range (1535-1570 nm). The signal of the TuLa passes the demultiplexer and multiplexer, which are connected in series. To measure the wavelength and the power of the TuLa signal after it has traversed the filters, an optical spectrum analyser (OSA) is used. Both the TuLa and the OSA are controlled and read out by software which runs on a standard PC.

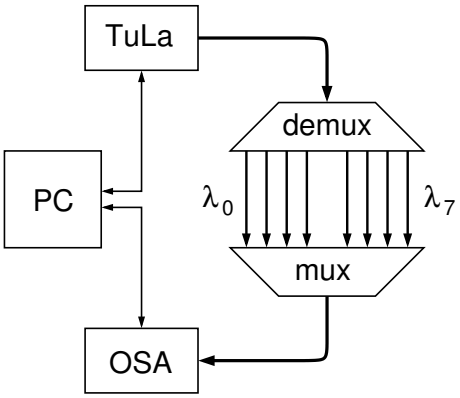

Figure 2.7: *A schematic view of the test set-up used for measurements on the DWDM multiplexer and demultiplexer. The filters are connected in series. The signal of a tunable laser (TuLa) passes the filters and is detected by an optical spectrum analyser (OSA). The TuLa and OSA are controlled and read out by a PC.*

Measurements and results

To determine the channel isolation, the transmission band of each filter channel was measured separately. The TuLa swept through the complete wavelength range of the DWDM system with steps of 0.25 nm. The output power level was set to a constant value of +10 dBm. For each step, the OSA measured the power and wavelength of the signal that passed the filters.

The measured transmission bands for all eight ITU wavelengths are shown in figure 2.8. The filter channels are divided into two groups. The channels that correspond to the largest wavelengths are referred to as the high-end channels, the other four channels as the low-end channels. The ITU wavelength and the laser operating window for each filter channel are shown in the figure as well. The channel isolation is determined for the worst case, which occurs at the edges of the laser operating window. As can be seen in the figure, there is no crosstalk between channels down to a power level of -35 dBm. The results for the channel isolation are listed in table 2.2.

To determine the bandpass properties, another measurement was performed with the step size of the TuLa set to 0.2 nm. All filter channels were connected and the joint transmission profile was measured with the TuLa output level set to +10 dBm. The top region of the measured transmission bands is shown in figure 2.9. The ITU wavelengths and the laser operating windows are shown in the figure as well. The errors on the measurements are also shown. The spectral width of the bandpass is determined by those wavelengths where the transmission power drops below 0.5 dB loss with respect to the maximum. These wavelengths are determined by linear interpolation between the two data points above and below this value. The bandpass for each channel is shown in the figure as a horizontal line in the transmission band. The values of the bandpass edges are given in table 2.2. The flatness of the bandpass within the laser operating window is also listed there.

To determine the insertion loss of the filter channels, the power level that corresponds to 0 dB loss must be known. Therefore, the filters were removed from the set-up and the output level of the TuLa was directly measured by the OSA. The difference between this measurement and the measured minimum power transmission of the bandpass within the laser window defines the insertion loss. Table 2.2 gives the insertion loss of the filter channels connected in series.

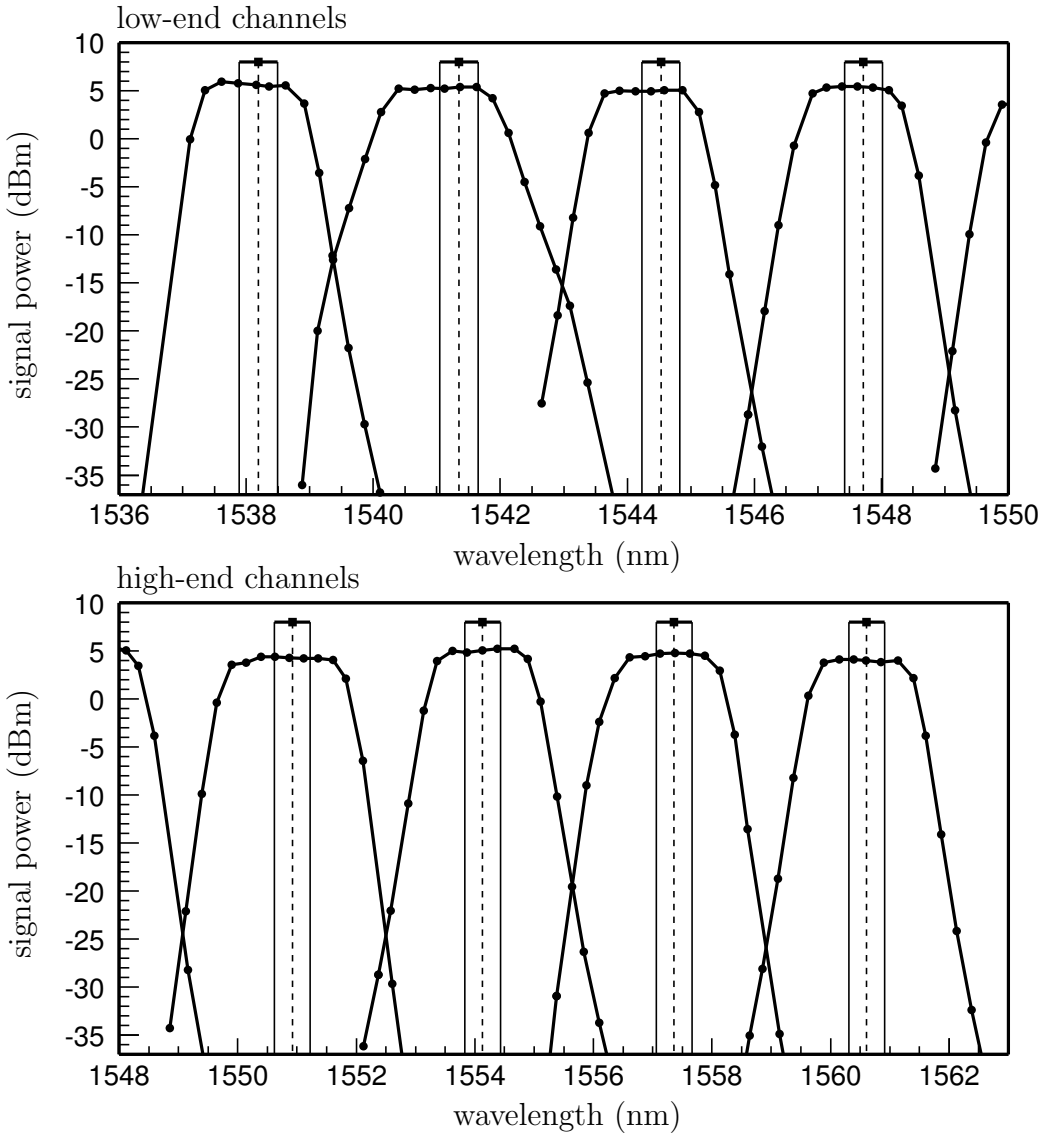

Figure 2.8: *The transmission bands of the filters for the eight ITU wavelengths. The bands were measured individually. The ITU wavelength of each channel is printed on top of the data as a dashed vertical line. The operating wavelength window of the laser is shown as solid vertical lines.*

2.2.4 Conclusions

The results of the measurements are tabulated in table 2.2 for all eight filter channels. The multiplexer and demultiplexer were connected in series during these measurements. The channel isolation of each channel is larger than 35 dB, which amply meets the 25 dB requirement. The maximum allowed insertion loss for the channels is 3.6 dB for each filter, which amounts to 7.2 dB for a multiplexer and demultiplexer connected in series. The results show that this requirement is also satisfied. The bandpass of each channel covers the corresponding ITU wavelength and laser operating window, as desired. As can

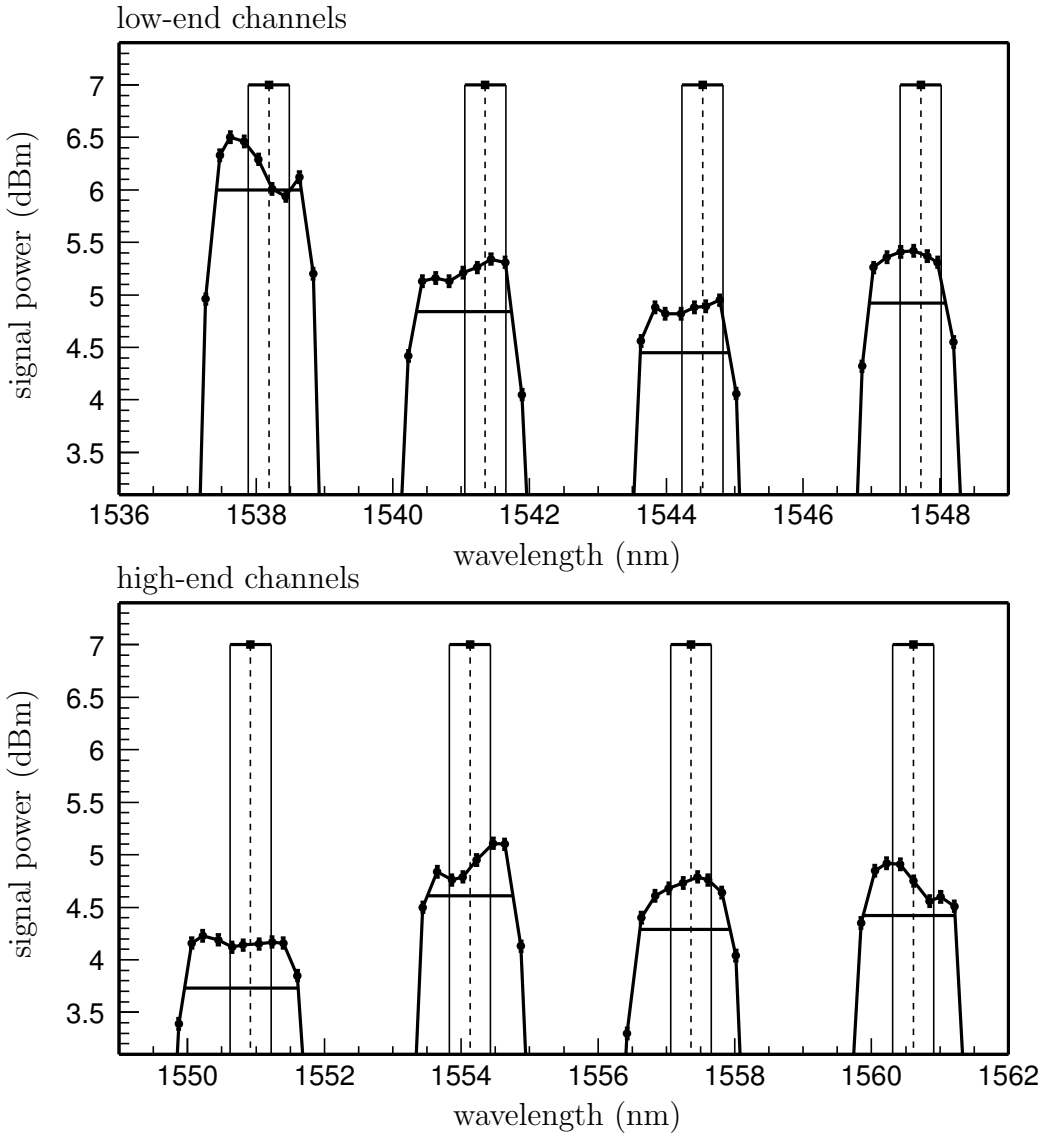

Figure 2.9: *The top region of the eight measured transmission bands. The ITU wavelengths and the laser operating windows are shown as dashed and solid vertical lines respectively. The solid horizontal lines in the transmission bands indicate the 0.5 dB bandpass of the corresponding channel.*

be seen in figure 2.9, for the first channel (1538.19 nm) one data point falls below the bandpass definition. The difference is still within the measurement errors. The flatness of this channel may exceed the 0.5 dB requirement when the error on its value is taken into account. The insertion loss of this channel is such, that this is nevertheless acceptable. The other channels display sufficient flatness. This means, that the selected multiplexer and demultiplexer satisfy the requirements for an expected system life-time of ten years.

ITU wavelength (nm)	flatness (dB)	insertion loss (dB)	channel isolation (dB)	bandpass 0.5 dB (nm)
				1537.42 ± 0.04
1538.19	0.5 ± 0.1	3.4 ± 0.1	> 35	↕
				1538.66 ± 0.04
				1540.35 ± 0.04
1541.35	0.1 ± 0.1	4.1 ± 0.1	> 35	↕
				1541.74 ± 0.04
				1543.62 ± 0.04
1544.53	0.2 ± 0.1	4.5 ± 0.1	> 35	↕
				1544.91 ± 0.04
				1546.97 ± 0.04
1547.72	0.3 ± 0.1	4.2 ± 0.1	> 35	↕
				1548.09 ± 0.04
				1549.95 ± 0.04
1550.92	0.1 ± 0.1	5.2 ± 0.1	> 35	↕
				1551.62 ± 0.04
				1553.51 ± 0.04
1554.13	0.3 ± 0.1	4.5 ± 0.1	> 35	↕
				1554.75 ± 0.04
				1556.61 ± 0.04
1557.36	0.1 ± 0.1	4.6 ± 0.1	> 35	↕
				1557.93 ± 0.04
				1559.87 ± 0.04
1560.61	0.4 ± 0.1	4.7 ± 0.1	> 35	↕
				1561.22 ± 0.04

Table 2.2: *Results of the measurements on the eight filter channels. The multiplexer and demultiplexer were connected in series during the measurements.*

2.3 Gigabit Ethernet

For the data transmission between the MLCMs and the shore, the Gigabit Ethernet (GbE) 1000BASE-X standard is used [37]. The data are transferred in a serial bit stream at a rate of 10^9 bits per second (1 Gbit/s). The transmission is in baseband, which means that the data signals are coupled directly into the optical fibre. Each data byte (8 bits) is transmitted as a 10-bit code according to the 8B10B encoding scheme [38]. The additional bits provide transmission redundancy that is used for a.o. separation of data and control codes and for suppression of direct current (DC) components in the data. The transmission rate of 1 Gbit/s corresponds to the effective rate at which the user data are transferred. The encoding of the data bytes into 10-bit code requires an actual transmission rate of 1.25 Gbit/s. The duration of a single bit in the bit stream is thus 0.8 ns. The data stream is synchronised with a local clock which has a frequency of 1.25 GHz.

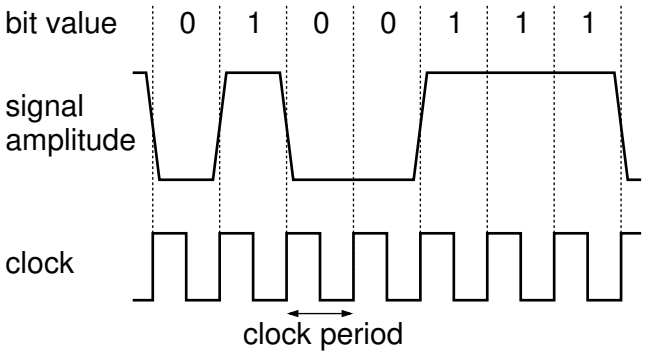

Figure 2.10: *Ideal signal shape of a transmitted bit stream. The bit stream is synchronised with the clock, whose frequency corresponds to the bit rate. The values of the bits are also shown.*

The 1000BASE-X standard uses a two-level, non-return-to-zero (NRZ) modulation of the signal amplitude to represent bits. The lower amplitude level corresponds to bits of value 0 (logical 0), the upper level to bits of value 1 (logical 1). The signal amplitude can change level at the boundaries between clock periods, and remains at the same level between bits with the same value. Figure 2.10 shows an ideal shape of a transmitted bit stream and its relation to the clock signal. The separation between the two amplitude levels is maximum for most of the clock period. The transitions between the levels occur rapidly and are centred on the boundaries between clock periods.

The GbE link from the MLCM to the shore is shown as a block diagram in figure 2.11. The transmission signal is formatted in the GbE switch in the MLCM. The output signal of the switch is an electrical bit stream. In the transmitter, this signal is used to modulate the output power level of the laser. The generated optical signal travels through the optical network from the detector to shore. On shore, the optical signal is detected and converted into an electrical signal by the photo diode. The receiver electronics amplify

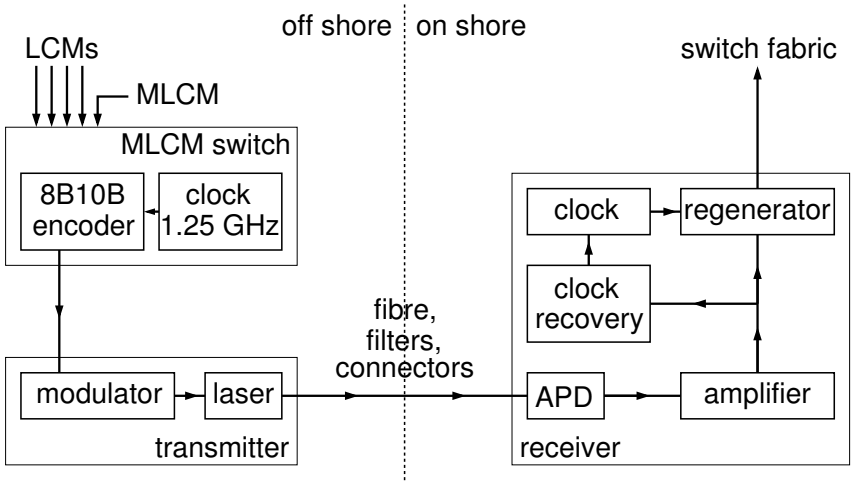

Figure 2.11: *A block diagram of the data link between the MLCM and the shore. The GbE bit stream, formatted in the MLCM switch, is used to modulate the laser. The generated optical signals travel through the optical network to shore, where they are detected by the photo diode (APD). The signals are converted into electrical signals and the bit stream is regenerated. It is then passed to the switch fabric.*

this signal and regenerate the original bit stream, which is then passed to the switch fabric for further routing to the data processing farm.

For the regeneration of the bit stream from the detected analogue signal, the signal amplitude is sampled every clock period to decide whether the bit value is 0 or 1. The sampling is done with a local clock which is synchronised with the bit stream by recovering the clock signal from that same bit stream.

2.3.1 System performance and the eye diagram

Limited bandwidth and thermal noise of the electronic components, power attenuation and dispersion in the optical network affect the transmitted signal. This results in a distorted signal shape at the receiver. Severe distortion may cause incorrect recovery of the data stream in the receiver, and consequently degrade the performance of the system.

A means to estimate the performance of a digital system is the so-called eye diagram. It can be formed by measuring the bit stream in a certain time interval around the centre of subsequent clock periods, and overlaying many measurements. In this way, an eye-like shape appears. Figure 2.12 shows the eye diagram of the ideal signal shape shown in figure 2.10 in the time interval from -T to T around the bit centre, where T is the clock period. The opening of the eye, indicated with the shaded area in figure 2.12, is a measure for the degree of signal distortion.

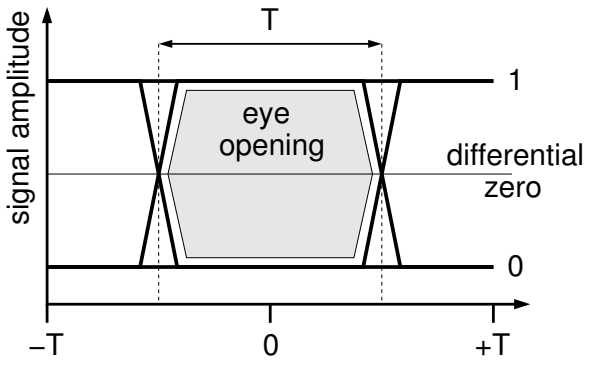

Figure 2.12: *The eye diagram of an ideal signal. It is formed by overlaying the signal shapes in the time interval [-T,T] around the centre of subsequent bits, with T the clock period. The eye opening, represented by the shaded area, is a measure for the distortion of the signal.*

The eye diagram of a real signal is shown in figure 2.13. This diagram was made from measurements acquired with a test set-up of the data link between the MLCM and the shore. These measurements are described in section 2.3.3. Compared to the ideal case, the transitions between the signal amplitude levels are less steep. The crossing points of the level transitions with the differential zero level are broader, and the signal does not always reach the minimum and maximum amplitudes. The eye opening of this signal, which is represented by the shaded area in the figure, is more closed than in the ideal case.

For correct recovery of the bit values in the receiver, the amplitude of the signal must be greater than (logical 1), or less than (logical 0), a certain threshold value at the moment of sampling. These thresholds are referred to as the decision thresholds. In addition, there may be an uncertainty in the phase of the recovered clock. Consequently, the sampling of the signal amplitude does not occur at a fixed time with respect to the signal, but

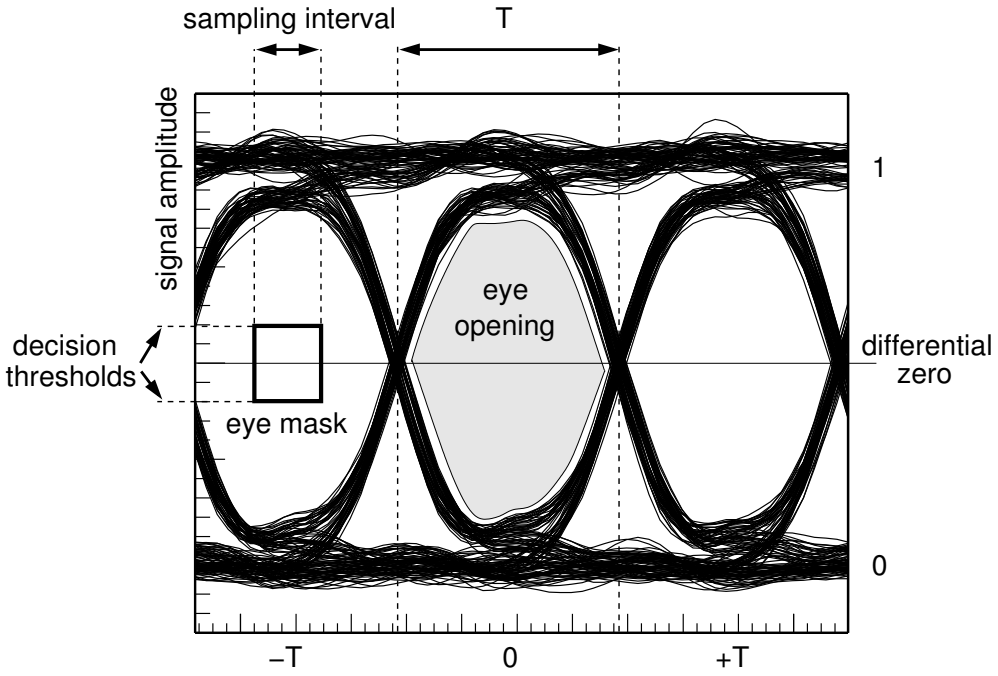

Figure 2.13: *The eye diagram of a real bit stream. The level transitions and amplitude levels are broader than in the ideal case (figure 2.12). This results in an eye opening, indicated with the shaded area, that is more closed. For regeneration of the bit stream in the receiver, the signal is sampled in a small time interval within each clock period. For correct recovery of the bit, the signal amplitude must be greater than (logical 1), or less than (logical 0), a certain threshold value at the moment of sampling. These decision thresholds and the sampling interval define the so-called eye mask.*

rather within a certain time interval. The region bounded by the sampling interval and the decision thresholds is referred to as the eye mask, as is shown in figure 2.13.

Thus, if the signal falls within the eye mask, it is expected that a bit is falsely recovered in the receiver. The probability that this happens can be estimated from the distance between the boundaries of the eye opening and the eye mask. The more closed the eye opening is, the more likely it is that the signal falls within the eye mask and a so-called bit error occurs.

2.3.2 Noise, signal-to-noise and bit error ratio

As can be seen in figure 2.13, there is a spread in the time that the level transitions of the signal cross the differential zero point. The time difference between the expected and actual differential zero crossing of a level transition is referred to as instantaneous jitter [39]. Average jitter is defined as the root mean square (RMS) value of multiple instantaneous jitter measurements. It is commonly expressed in units of psrms (picosecond rms). Jitter can be divided into two fundamental types. The first type is random jitter, which is due to thermal and other random noise effects. It is unpredictable and typically

has a Gaussian probability density function. The second type is deterministic jitter, which is caused by non-ideal component behaviour in the system. It has a non-Gaussian distribution and usually has definite lower and upper bounds. Therefore, deterministic jitter is commonly expressed in terms of a peak-to-peak value with unit psp-p (picosecond peak-to-peak). The amplitude levels of the signal also show a spread, as can be seen in figure 2.13. The origins of random and deterministic jitter also account for this.

The performance of a digital transmission system is commonly expressed in terms of the bit error ratio (BER). This is the ratio of the number of falsely recovered bits to the total number of bits received. As explained in the previous section, a bit error may occur when the signal amplitude is in between the decision thresholds at the moment of sampling. If the amplitude has a Gaussian distribution, the probability of a bit error (i.e. the BER) can in principle be calculated when the signal-to-noise ratio (SNR) is known [40]. The signal S in this case is the distance between the average of the amplitude level (which is related to the boundary of the eye opening) and the decision threshold. The noise N is the standard deviation σ of the amplitude level distribution. When the noise exceeds the signal at the moment of sampling, it can be expected that a bit error occurs. The probability of a bit error is then equal to the area of the Gaussian beyond the decision threshold. The BER can thus be calculated as

$$BER = \int_{S/N}^{\infty} \frac{1}{\sqrt{2\pi}} e^{-x^2/2} dx \ . \tag{2.1}$$

2.3.3 Measurements on the Gigabit Ethernet link

Measurements on the data link that is used between the MLCM and the shore were carried out with a test set-up in order to determine the jitter and BER of the transmission system. The goal of the measurements described in this section is merely to demonstrate that the BER of the system can be determined from an analysis of the eye diagram.

Test set-up

A schematic view of the measurement set-up is shown in figure 2.14. Two standard PCs are interconnected via a GbE link which consists of the optical transmitter, fibre and receiver that are normally used in the data transmission from the MLCM to the shore. Software that runs on the first PC sends data to the second PC through this link. A digital oscilloscope is used to measure and digitise the received signal before it is regenerated. The oscilloscope is controlled and read out by a user interface that runs on a third PC.

The digital oscilloscope has a real-time sampling rate of 1 GHz, which is insufficient for the reconstruction of the 1.25 GHz bit stream. Therefore, the oscilloscope is operated in equivalent-time sampling mode [41]. In this mode, the oscilloscope samples the signal at a rate of 1 GHz across multiple triggers. Each sampling period starts at a different time with respect to the trigger. In this way, the oscilloscope acquires 25×10^9 samples per second. A maximum of 15,000 such samples can be stored in the oscilloscope, which corresponds to 600 ns. These data are transferred to the third PC and stored as binary files.

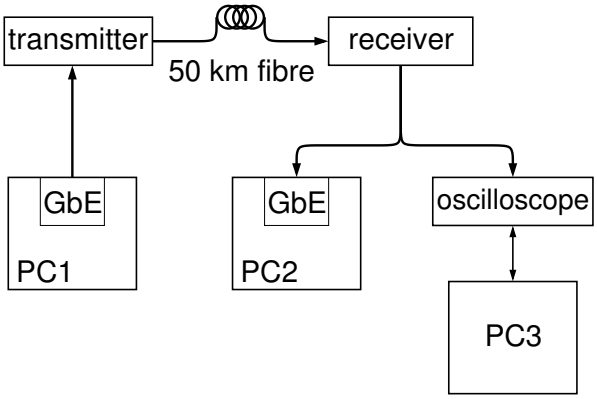

Figure 2.14: *A schematic view of the test set-up used for the measurements on the data link that is used between the MLCM and the shore. Data are sent from a standard PC to another over the link. The received signal is measured with a digital oscilloscope. The oscilloscope is controlled and read out by a third PC.*

Analysis of the measurements and results

The transmission signals of two different, repetitive bit patterns were measured. The repetitive patterns were constructed by giving each byte in the transmission data the same value. The two patterns are defined by the hexadecimal notation of their byte content, which are 0xFE and 0x78 respectively. According to the 8B10B encoding scheme, each pattern has two corresponding 10-bit transmission codes which have opposite polarity. Which 10-bit code is used for transmission of the byte, is based on the preceding sequence of bits in the data. This is done to provide sufficient density of level transitions for clock recovery, and to balance DC components in the data. The byte content and the corresponding 10-bit codes of both patterns are shown in table 2.3.

pattern label	8-bit data	10-bit codes	
		(-)	(+)
0xFE	1111 1110	01111 00001	10000 11110
0x78	0111 1000	11001 10011	00110 01100

Table 2.3: *The byte content and the corresponding 10-bit transmission codes of the two bit patterns that were used for the measurements. Each pattern can be represented by two 10-bit codes that have opposite polarity.*

In the case of the 0xFE pattern, the transmitted bit stream in the measurements is a repetition of the 10-bit code 01111 00001. Consequently, the stream contains sequences of either one or four bits with the same value. For the 0x78 pattern, the bit stream is an alternation of the two 10-bit codes. Hence, this pattern only contains sequences of two equal bits. For both patterns several measurements were done, each measurement containing 600 ns of data.

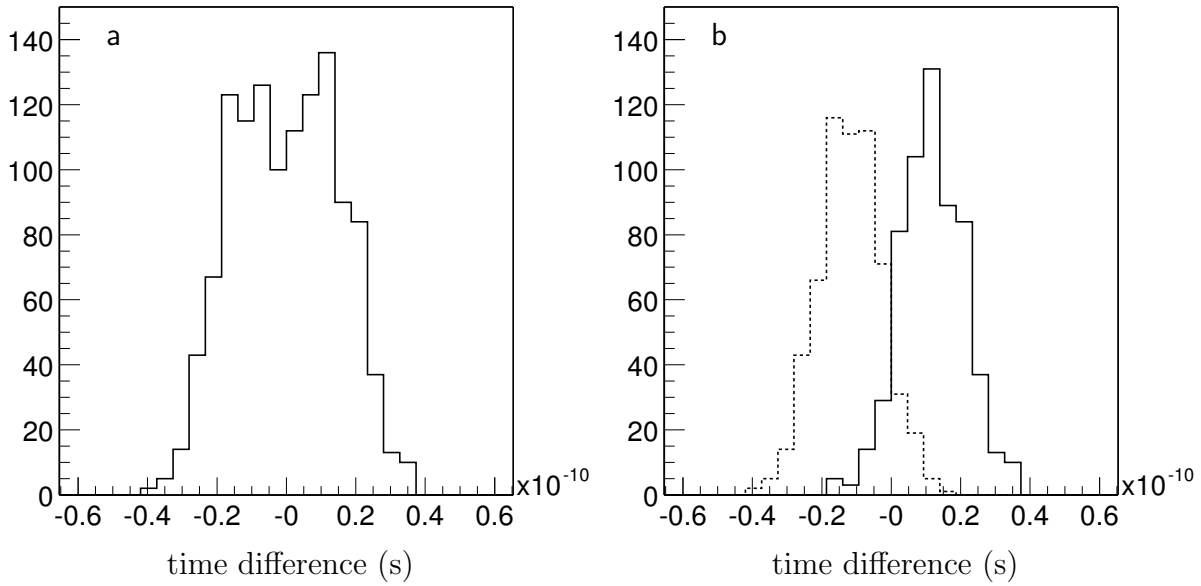

Figure 2.15: *a: The distribution of 1200 instantaneous jitter measurements of the 0xFE pattern. b: The distribution in (a) is split up according to the bit sequence in the pattern before a level transition (see text).*

An algorithm was developed to determine the jitter and amplitude spread from the data acquired with the oscilloscope. First, the times that the signal crosses the differential zero level are reconstructed. This is done for each crossing by linear interpolation between the two data points that are directly above and below the differential zero level. The clock frequency of the signal is obtained from a linear fit through the reconstructed zero crossing times. With this clock frequency, the times that the signal is expected to cross the zero level are calculated. The time difference between the expected and the reconstructed zero crossing of a level transition is then an estimate of the instantaneous jitter.

Figure 2.15a shows the distribution of the instantaneous jitter of 1200 level transitions of the 0xFE pattern. The RMS value of the distribution is about 15 ps. The distribution seems to indicate the presence of two peaks. According to the definitions of random and deterministic jitter given in section 2.3.2, this may indicate that the jitter has a deterministic component. A common type of deterministic jitter is data dependent jitter. It is caused by bandwidth limitations of the transmission system, and appears as a phase difference between level transitions of quickly and slowly changing bit patterns.

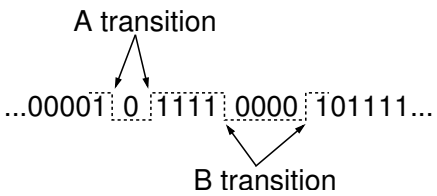

Figure 2.16: *The 0xFE pattern contains sequences of one and four equal bits. A level transition that occurs after a 1-bit sequence is referred to as an A transition, a transition after a 4-bit sequence is referred to as a B transition.*

The 0xFE pattern contains sequences of either one or four equal bits before a level transition, as is shown in figure 2.16. Level transitions that occur after a 1-bit sequence (i.e. a quickly changing pattern) are referred to as A transitions. Transitions after a 4-bit sequence (i.e. a slowly changing pattern) are referred to as B transitions. When the A and B transitions are considered separately, the instantaneous jitter distribution in figure 2.15a splits up into two distinct distributions, as is shown in figure 2.15b. The solid line represents the jitter distribution of A transitions, the dashed line that of B transitions. As can be seen in the figure, indeed a phase difference between the two different transitions is present. The RMS value of both distributions is about 9 ps. These values are significantly smaller than the common RMS of 15 ps. The phase difference between the A and B transitions is determined from the mean values of the distributions, and is approximately 24 ps.

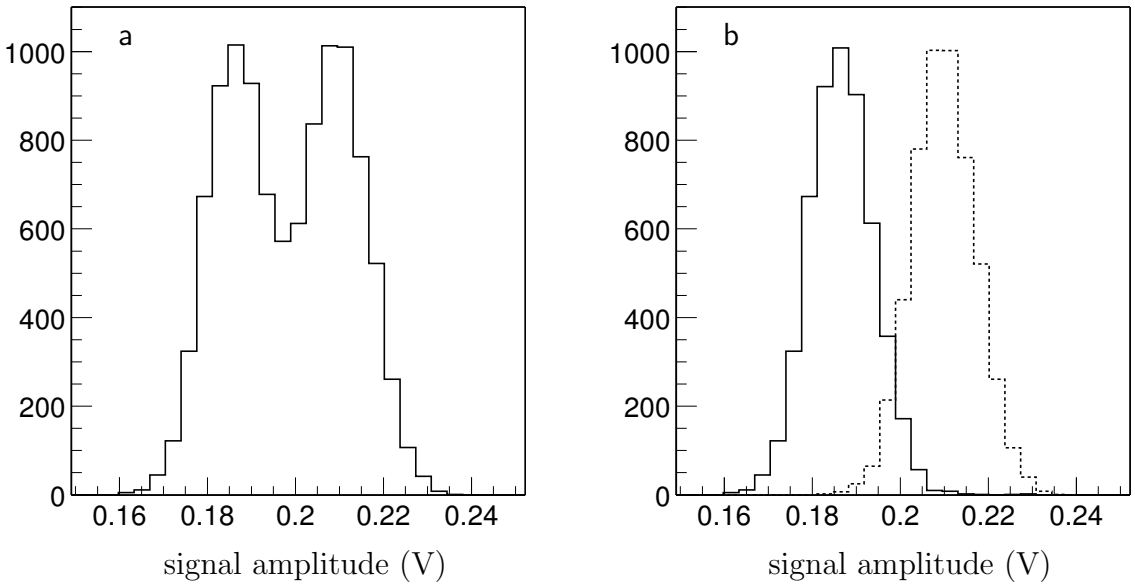

Figure 2.17: *a: The distribution of the signal amplitude of a logical 1 in the 0x78 pattern. b: The distribution in (a) is split up according to the value of the preceding bit (see text).*

The signal amplitude sampling for bit recovery in the receiver typically occurs in the time interval between 0.4T and 0.6T, with T the clock period. For each bit in the measured bit stream, the algorithm determines which data points fall within the sampling interval according to the reconstructed clock frequency. The distribution of the differential amplitude value is shown in figure 2.17a for the upper amplitude level (logical 1) of the 0x78 pattern. The distribution has a mean of 0.20 V and an RMS value of 0.014 V. The distribution clearly shows two distinct peaks.

The 0x78 pattern only contains sequences of two equal bits after a level transition, as is shown in figure 2.18. The first bit after a level transition to a logical 1 is denoted as bit A, the second bit after such a transition as bit B. Thus, bit A is preceded by a bit of value 0, whereas bit B is preceded by a bit of value 1. When the amplitude values of bit A and B are considered separately, the amplitude distribution in figure 2.17a splits up

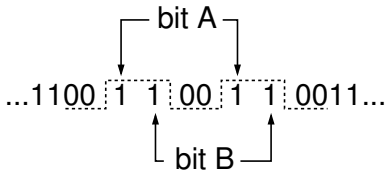

Figure 2.18: *The 0x78 pattern consists of sequences of two equal bits. The first bit after a transition to the upper amplitude level is referred to as bit A, the second bit after the transition as bit B.*

into two separate distributions, as is shown in figure 2.17b. The solid line corresponds to the amplitude distribution of bit A, the dashed line to that of bit B. As can be seen from the figure, the amplitude level of a logical 1 is affected by the value of the preceding bit.

When it is assumed that the two distributions in figure 2.17b are due to only random noise effects, the BER of the system for the 0x78 pattern can be determined as explained in section 2.3.2. Therefore, a Gaussian function is fitted to both distributions. The results are shown in figures 2.19a and 2.19b. The fit to the amplitude distribution of bit A yields a χ^2 value of 1.5 per degree of freedom, and has a mean and σ of 0.187 V and 0.00721 V respectively. For bit B, the fit gives a χ^2 value of 0.94 per degree of freedom, and has a mean and σ of 0.210 V and 0.00726 V respectively. The normalised χ^2 values indicate that the distributions are fitted rather well.

For a given decision threshold of 50 mV, the amplitude distribution of bit A gives the worst-case SNR, which is $(0.187 - 0.050)/0.00721 \approx 19$. The corresponding BER can be calculated with the integral in equation 2.1, which is evaluated numerically. The BER for an SNR of 19 is smaller than the precision with which the integral can be determined. This precision is of the order of 10^{-16}, and is reached at an SNR of about 8.2. Therefore, an analytical estimate of the upper limit of the BER is made. This is done by rewriting

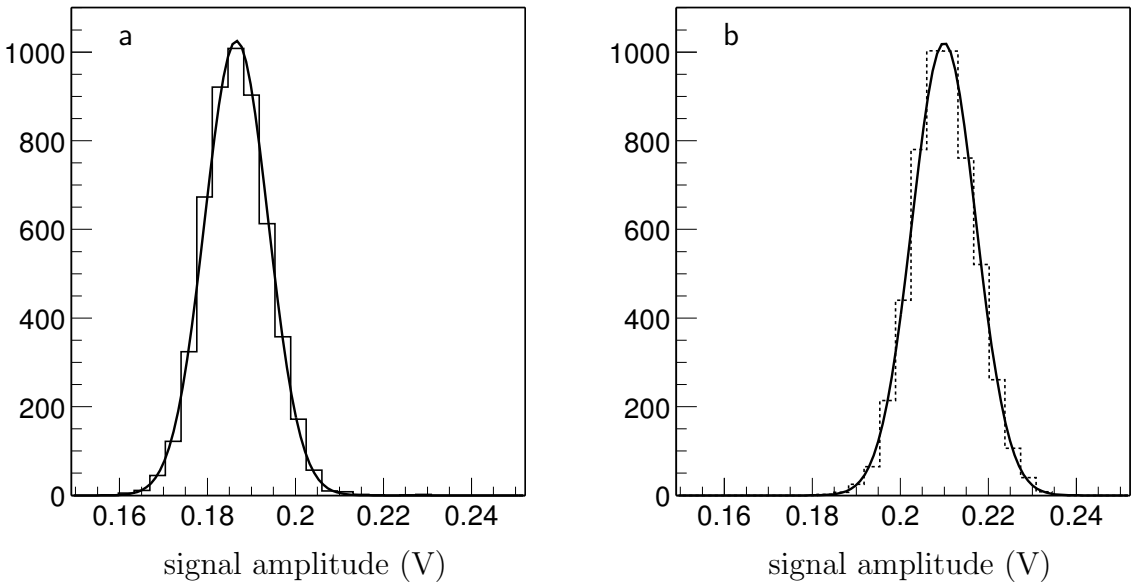

Figure 2.19: *a: Gaussian fit on the amplitude distribution of bit A. b: Gaussian fit on the amplitude distribution of bit B.*

equation 2.1 as

$$\begin{aligned} \int_{S/N}^{\infty} \frac{1}{\sqrt{2\pi}} e^{-x^2/2} dx &= \frac{1}{\sqrt{2\pi}} \sqrt{\int_{S/N}^{\infty} e^{-x^2/2} dx \int_{S/N}^{\infty} e^{-y^2/2} dy} \\ &\leq \frac{1}{\sqrt{2\pi}} \sqrt{\int_{0}^{\pi/2} \int_{S/N}^{\infty} e^{-r^2/2} r dr d\phi} \ . \end{aligned} \tag{2.2}$$

A graphical representation of this inequality is shown in figure 2.20. The BER corresponds to the square root of the integral over the shaded area in the figure, which has the limits $\frac{S}{N} \leq x < \infty$ and $\frac{S}{N} \leq y < \infty$. This integral cannot be calculated exactly. However, an upper limit on the integral is given by the integral over the area with limits $0 \leq \phi \leq \pi/2$ and $\frac{S}{N} \leq r < \infty$. The right hand side of equation 2.2 then becomes $\frac{1}{2} e^{-(S/N)^2/4}$, which for an SNR of 19 gives an upper limit on the BER of the order of 10^{-40}.

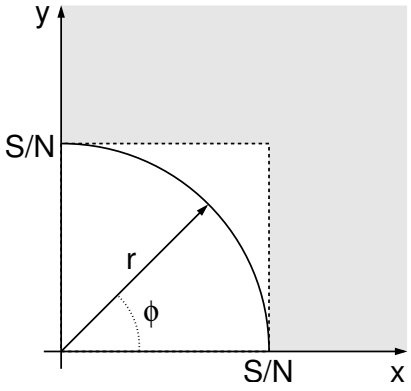

Figure 2.20: *A graphical representation of the inequality in equation 2.2.*

The results discussed above apply to the amplitude of a logical 1 in the 0x78 pattern. The results for a logical 0 in this pattern also yield a worst-case SNR of approximately 19, and a corresponding BER of less than 10^{-40}.

2.3.4 Conclusions

A test set-up to measure the performance of the GbE link between the MLCM and the shore was built. With the set-up, the transmission signal of different bit patterns was measured with a digital oscilloscope. An algorithm was developed to estimate the jitter and bit error ratio of the system from the oscilloscope data. The dependence of the jitter on slowly and quickly changing bit patterns could be demonstrated. Also, the dependence of the signal amplitude on the sequence of the bits was shown.

The jitter of the system was determined for data consisting of the 0xFE bit pattern. It was shown that the jitter contains a data dependent component, induced by the sequences of 1 and 4 equal bits in the pattern. The data dependent jitter is about 24 psp-p, and the average jitter of the system is approximately 9 psrms for both the 1-bit and 4-bit sequences in the data.

The BER of the system was determined from measurements of the 0x78 pattern, which only consists of 2-bit sequences. For a decision threshold of 50 mV, the BER is smaller than 10^{-40}, which corresponds to about one bit error per 6×10^{22} years with the rate

at which data is taken with the ANTARES detector (see chapter 1). This period is longer than the expected life-time of the detector. However, the data set that is used to determine the BER is limited. It is expected that more measurements will yield a more realistic estimate of the BER. Moreover, the used method relies on the assumption that the signal amplitude has a Gaussian distribution. This assumption might be wrong, although the distributions shown in figure 2.19a and 2.19b do not suggest this.

Another, more reliable estimate of the BER of the used GbE link is given in [42]. It was obtained by measuring the retransmission rate of data packages using a higher level protocol (TCP), and is of the order of 10^{-22}. This corresponds to about one bit error per 60,000 years.

Chapter 3

Magnetic monopoles

In this chapter a brief description of theories that predict the possible existence of magnetic monopoles is given. The creation of monopoles in the early Universe and their acceleration in the cosmos are explained. The interaction of monopoles with matter, which provides a means to detect them, is also described. Since monopoles have not (yet) been observed, the searches for them have resulted in a number of upper limits on their flux. These limits are summarised at the end of the chapter.

3.1 The Dirac monopole

In 1931, Dirac showed that the theory of quantum mechanics allows the existence of magnetic monopoles, provided that their magnetic charge is quantised [43]. He found that the magnetic charge g is connected with the elementary electric charge e by the relation

$$2eg = k\hbar c \ , \tag{3.1}$$

where k is an integer. This is referred to as Dirac's quantisation condition. The numerical value of the magnetic charge quantum g_D, also called the Dirac charge, follows from the value of the fine-structure constant $\alpha = e^2/\hbar c$ and is

$$g_D = \frac{e}{2\alpha} \simeq \frac{137}{2} e \ . \tag{3.2}$$

A prediction of the monopole mass, however, is not possible within the framework of quantum mechanics.

3.2 The 't Hooft/Polyakov monopole

In 1974, 't Hooft and Polyakov showed that magnetic monopoles occur as solutions in unified gauge theories in which the electromagnetic group U(1) is taken as a subgroup of a larger compact gauge group [44, 45]. In these theories, the mass and charge of the monopoles are calculable. In fact, monopole solutions necessarily exist in theories where a simple gauge group is spontaneously broken into a subgroup that contains an explicit U(1) factor [46].

Grand unified theories (GUTs) are based on the hypothesis that at sufficiently high energies, the strong gauge coupling is of the same order as the coupling in the gauge theories of the weak and electromagnetic interactions. At these energies, all interactions can be described with a single simple gauge group in which only one gauge coupling appears. At lower energies, the unified gauge group is spontaneously broken into the gauge group SU(3) × SU(2) × U(1), with SU(3) the strong and SU(2) × U(1) the electroweak symmetries of the Standard Model. Hence, the existence of magnetic monopoles is a generic prediction of grand unification.

The mass M of the monopoles generated in the symmetry breaking of the unified group is related to the energy scale Λ of the unification by

$$M \gtrsim \frac{\Lambda}{\alpha_G} \,, \tag{3.3}$$

where α_G is the unified gauge coupling constant. As determined from the running of the low-energy coupling constants, Λ and α_G are expected to be of the order of 10^{15} GeV and 10^{-2} respectively [46]. Thus, monopoles associated with GUTs have masses of the order of 10^{17} GeV. Objects with such masses cannot be produced in today's man-made particle accelerators. It is very likely that the only place where they could have been produced is the hot early Universe.

3.3 Creation of monopoles in the early Universe

It is expected that gauge symmetries that are broken today, were restored at the high temperatures in the early Universe [47]. As the Universe expanded and cooled, so-called phase transitions occurred that were associated with the spontaneous breakdown of these gauge symmetries. It is assumed that at a temperature of order Λ, the Universe underwent a phase transition in which the grand unified symmetry was spontaneously broken. In this phase transition, magnetic monopoles appeared as so-called topological defects according to the Kibble mechanism [48]. In this mechanism, roughly one monopole is created per causal domain at the time of the transition. With a typical monopole mass of 10^{17} GeV, this results in a mass density of relic monopoles that exceeds the mass density of the observable Universe by many orders of magnitude [49]. This inconsistency is referred to as the "monopole problem". It can be solved by assuming an inflationary phase in the early Universe, which dilutes the monopole density to a very small number [50]. Another possible solution is based on GUT models in which monopoles first appear in a phase transition at a temperature far below the initial unification scale [51]. Besides a smaller monopole density, this also leads to less massive monopoles.

The predictions for the mass and charge of monopoles depend strongly on the choice of the unified group and its symmetry breaking pattern in the early Universe. A minimal SU(5) model leads to monopoles which carry one Dirac charge and have masses of order 10^{17} GeV [52, 53]. Gauge models based on superstring theory give monopoles with masses of 10^{16} GeV and three Dirac charges [54]. Monopoles with masses of the order of 10^{13} to 10^{14} GeV and two units of Dirac charge occur in a model based on SO(10) [55]. An extension of minimal SU(5) results in a monopole mass of about 10^{11} GeV [56]. Monopoles with a mass of about 10^{8} GeV appear in an SU(15) GUT model [57, 58]. Some

supersymmetric models imply monopoles with multiple Dirac charges and masses as low as 10^7 GeV [59, 60]. With a monopole mass that varies over several orders of magnitude, and a monopole charge that can be between one and multiple Dirac units, the theoretical picture is thus far from unique.

3.4 Acceleration of cosmic monopoles

Similar to an electric charge in an electric field, magnetic monopoles are accelerated along the field lines of a magnetic field. While travelling a distance l along the direction of a magnetic field with strength B, a monopole with magnetic charge g gains kinetic energy

$$T = gBl \ . \tag{3.4}$$

Monopoles residing in the Universe are accelerated by large scale magnetic fields in the cosmos. In the galactic magnetic field for instance, which has a strength of approximately 3×10^{-6} G and a coherence length L of about 300 pc [61], a monopole with one Dirac charge can gain up to about 6×10^{10} GeV. Table 3.1 shows the properties of the magnetic fields of several astrophysical and cosmological environments. The typical kinetic energy of a monopole with unit Dirac charge that traverses a single coherent domain of these fields is also listed. The largest energies, about 10^{15} GeV, are obtained in fields that have the largest coherence lengths. Since radiative losses of monopoles and their interaction with electromagnetic radiation can be considered negligible in these environments [56, 62], monopoles with masses up to about 10^{15} GeV can be accelerated to relativistic velocities. This is in contrast with acceleration by gravitational fields, which results in monopole velocities that are limited to about $10^{-2}\,c$ [63].

cosmic environment	B (μG)	L (pc)	T (GeV)
Milky Way	3	300	$\sim 6 \times 10^{10}$
galaxy clusters	2 - 30	$10^2 - 10^6$	$10^{10} - 10^{15}$
extragalactic sheets	0.1 - 1	$10^6 - 3 \times 10^7$	$10^{12} - 10^{15}$
AGN jets	10^2	$10^2 - 10^4$	$10^{11} - 10^{13}$
radio galaxy lobes	$10 - 10^2$	10^5	$10^{13} - 10^{14}$

Table 3.1: *Magnetic field strength B and coherence length L of several cosmic magnetic fields, taken from [61, 62, 64]. The typical kinetic energy T of a magnetic monopole that traverses such a field is given in the last column.*

3.5 Fluxes of cosmic monopoles

Since theory does not predict a unique picture of monopole properties (see section 3.3), the most reliable limits on the flux of relic monopoles are given by considerations that are not dependent on specific models. An upper limit on the monopole flux can be derived from the cosmological requirement that the monopole mass density cannot exceed the mass

density of the Universe. As was recently confirmed, the mass density of the Universe is approximately equal to the critical density [65]. This leads to the limit on the average monopole flux [63]

$$\langle F \rangle \lesssim 10^5 \frac{v}{c} \frac{1}{M} \ \text{cm}^{-2}\text{sr}^{-1}\text{s}^{-1} \ , \tag{3.5}$$

with v the typical monopole velocity, c the speed of light and the monopole mass M in GeV. Adiabatic expansion of the Universe and a uniform distribution of monopoles in the cosmos have been assumed here. The upper limit on the flux of monopoles with mass 10^{17} GeV and typical velocity $10^{-3}\,c$ [63] is then 10^{-15} cm^{-2}sr^{-1}s^{-1}. This corresponds to about 4×10^{-3} monopoles per m^2 per year. The flux limits for monopoles with smaller masses are less strict, as can be seen in figure 3.1. This also accounts for monopoles with larger velocities, and for the case that monopoles are not uniformly distributed, but are clustered in galaxies [63].

Another limit on the monopole flux is the so-called Parker bound [66]. It is based on the requirement that the galactic magnetic field is not dissipated faster by acceleration of monopoles than it is regenerated by the dynamo action of the galactic disk [67]. This implies a mass-independent upper limit on the galactic monopole flux of approximately 10^{-15} cm^{-2}sr^{-1}s^{-1} for monopoles with masses less than 10^{17} GeV and typical velocity $10^{-3}\,c$ [61]. The Parker bound is also shown in figure 3.1. For larger monopole masses and velocities, the limit is less stringent.

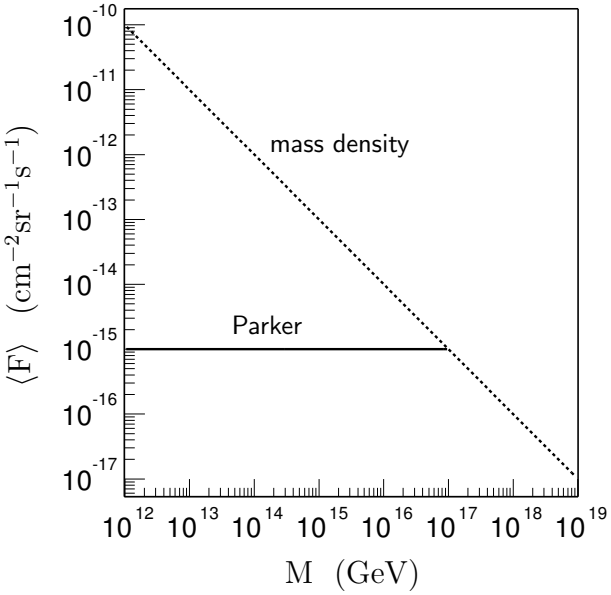

Figure 3.1: *Upper limits on the average monopole flux $\langle F \rangle$ as a function of the monopole mass M for a typical monopole velocity of $10^{-3}\,c$. The limits are based on the mass density of the Universe (dashed line) and the survival of the galactic magnetic field (i.e. the Parker bound, solid line).*

3.6 Detection of monopoles

Magnetic monopoles are one of the few predictions of GUTs that can be studied in the present low-energy environment. Being relics of the earliest moments of the Universe,

they are very interesting objects for which to search. The detection of monopoles relies, of course, on their interaction with matter and the related energy deposit.

3.6.1 Ionisation energy loss

When a magnetic monopole is in motion, its radial magnetic field induces a cylindrically symmetric electric field perpendicular to the direction of motion. While a monopole passes through matter, the magnetic and electric field interact with the medium, causing excitation and ionisation of the surrounding atoms. The energy that the monopole loses in these collisions with atomic electrons is referred to as ionisation energy loss. In first approximation, the ionisation energy loss of a monopole with magnetic charge g and velocity βc is about $(g\beta/ze)^2$ times larger than that of a particle with electric charge ze and the same velocity [68]. A monopole with one Dirac charge g_D (see equation 3.2) and $\beta \simeq 1$ thus deposits about 4700 times more energy than a minimum ionising particle with unit electric charge.

A more accurate relation for the average ionisation loss dE per unit distance dx travelled by a monopole in a nonconducting medium is given by [69]

$$\frac{dE}{dx} = \frac{4\pi N g^2 e^2}{m_e c^2} \left[\ln \frac{2m_e c^2 \beta^2 \gamma^2}{I} + \frac{K}{2} - \frac{1+\delta}{2} - B \right] , \tag{3.6}$$

which is the equivalent of the Bethe-Bloch formula for heavy electric charges. Here N is the electron density in the medium, m_e is the electron mass, βc is the monopole velocity, γ is the monopole's Lorentz factor, I is the mean excitation energy of the medium, δ is the density-effect correction, B is the Bloch correction and K is the so-called KYG cross-section correction [70]. The formula is valid in the velocity range $\beta \gtrsim 0.1$ and $\gamma \lesssim 100$.

Phenomena related to ionisation energy loss are the emission of Cherenkov radiation and the production of knock-on electrons (δ-rays). Cherenkov radiation provides the possibility to detect fast monopoles in transparent media. In a medium with refractive index n, a monopole with $\beta > 1/n$ emits a factor $(gn/ze)^2$ more Cherenkov light than an electrical charge ze with the same velocity [71]. In sea water with $n \simeq 1.35$, the Cherenkov light emission of a monopole with g_D thus exceeds that of a singly charged minimum ionising particle by a factor of about 8500. Cherenkov light can also be emitted by the abundance of energetic δ-rays that are produced along the trajectory of a monopole. This makes it possible to detect monopoles with $\beta < 1/n$. The Cherenkov light and δ-ray production of a monopole are discussed in more detail in chapter 4.

3.6.2 Radiative energy losses

The total energy loss of a monopole with $\gamma \lesssim 10^4$ is dominated by the ionisation energy loss. Above γ values of about 10^4, direct pair production and photonuclear interactions become the dominant energy loss processes [72], since bremsstrahlung is suppressed by a factor that is proportional to the inverse of the monopole mass [64]. These processes are commonly referred to as radiative processes.

3.6.3 Monopole catalysis of nucleon decay

As was shown by Rubakov [73, 74] and Callan [75, 76] in the early 1980's, magnetic monopoles within certain GUT models may catalyse the decay of nucleons. For nonrelativistic velocities of the monopole, a practical estimate of the catalysis cross section σ_{cat} takes the form

$$\sigma_{cat} = \frac{\sigma_0}{\beta} \ , \tag{3.7}$$

where σ_0 is roughly of the order of 10^{-28} cm^2 [77]. The catalysis cross section needs to be corrected when the electromagnetic interaction of monopoles with nucleons and nuclei is taken into account [78]. For free protons, this leads to an enhancement of the cross section proportional to β^{-1} [77, 78]. For certain heavier elements however, the cross section is suppressed by factors of the order of 10^{-2} to 10^{-6} for β between 10^{-3} and 10^{-4} respectively [78].

Monopole catalysis of nucleon decay does not seem to be a general property of GUTs. It was shown that it is possible to construct GUTs which exclude monopole catalysis [79, 80, 60, 59]. It may even be absent in the unification model studied by Rubakov and Callan [81].

3.6.4 Experimental flux limits

Many searches for cosmic monopoles have been performed since the theoretical prediction of their existence, using different techniques. A velocity and mass independent search for moving magnetic monopoles can be performed by measuring the change in electric current in a superconducting coil, see e.g. [82]. The shielding of these so-called induction detectors against any variation in the ambient Earth's magnetic field leads to high costs, which limits the detection area [51]. This difficulty is overcome by experiments that search for excitation and ionisation caused by monopoles. The MACRO experiment applied different types of excitation and ionisation detectors (liquid scintillators, streamer chambers and nuclear track-etch material) to search for monopoles in a large velocity range, $\beta \geq 4\times10^{-5}$, with a detection area of several 100 m^2 [83]. Another experiment based on the ionisation properties of monopoles is the Ohya experiment, which has used a 2000 m^2 array of track-etch detector to search for supermassive relic particles in the same velocity range as MACRO [84]. The bright Cherenkov signal of a monopole in water and ice (see section 3.6.1) is used by the Baikal and AMANDA neutrino telescopes to search for fast monopoles with $\beta \geq 0.8$ [85, 86]. Other experiments have been searching for the catalysis of proton decay, see e.g. [87, 88].

As no monopole candidates have been found, only upper limits on the cosmic monopole flux have been set. Some of the most restrictive limits for $\beta > 0.1$ follow from the experiments mentioned above, and are shown in figure 3.2. The Parker bound (see section 3.5) for $\beta = 10^{-3}$ is also shown in the figure. The flux limits are for monopoles with one Dirac charge, and are taken at a confidence level of 90%. The most stringent limit is set by the AMANDA detector for $\beta \simeq 1$, and is 0.61×10^{-16} cm^{-2}sr^{-1}s^{-1}. This is well below the Parker bound, and corresponds to about 2.4×10^{-4} monopoles per m^2 per year.

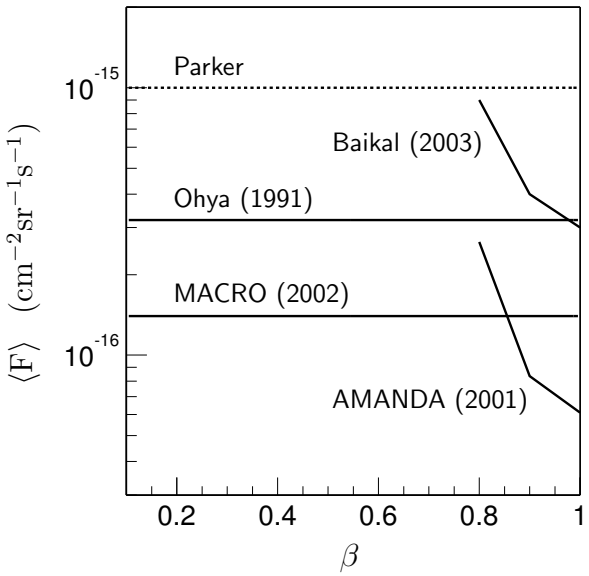

Figure 3.2: *Experimental upper limits (90% confidence level) on the average monopole flux $\langle F \rangle$ as a function of the monopole velocity βc (solid lines). The Parker bound for $\beta = 10^{-3}$ is also shown (dashed line).*

3.7 Monopole detection with ANTARES

At high velocities, monopoles emit very intense Cherenkov light in transparent media. This provides the possibility to search for relativistic monopoles with underwater and underice neutrino telescopes. Since a large detection area can be achieved with such detectors, a meaningful search for fast monopoles can be performed with them. In fact, the most stringent experimental limit on the flux of relativistic monopoles has been set by the AMANDA neutrino telescope. This limit corresponds to roughly 10 detectable monopoles per year for the ANTARES detector, which motivates a monopole search with it.

In the remainder of this thesis, the preparatory work for monopole detection with the ANTARES telescope is described. It only concerns the ionisation energy loss of monopoles, because the catalysis of nucleon decay is not necessarily a general feature of monopoles, and radiative losses are negligible at the monopole velocities that are considered. The work includes the direct Cherenkov light emission by monopoles, but focuses on the Cherenkov light that is emitted by the δ-rays that monopoles produce. As will be shown in the next chapter, monopoles emit direct Cherenkov light in the sea water when their velocity exceeds $0.74\,c$. The Cherenkov photons are then emitted in a narrow cone at the characteristic Cherenkov angle, which depends on the monopole velocity. The δ-ray induced Cherenkov radiation is characterised by a more isotropic emission of the photons and can lead to detectable signals of monopoles with velocities above $0.51\,c$. Monopoles with such velocities pass through the detector in a straight line and with a constant velocity. Muons, on the other hand, are visible as trajectories only at velocities very close to c. The corresponding Cherenkov angle is about 42 degrees. Consequently, the time-position correlations between hits caused by a monopole can be different from those between hits from a muon. This has been used in the development of a software trigger and an analysis method that are dedicated to the detection of monopoles with velocities

below about $0.74\,c$. The features and performance of the trigger are described in chapter 5. The analysis of monopole signals is explained in chapter 6.

Chapter 4

Monopole signals

In this chapter, the direct and δ-ray induced Cherenkov light emission by magnetic monopoles are discussed. They provide the possibility to detect relativistic monopoles with the ANTARES detector. Parameterisations of the direct and indirect Cherenkov light spectra have been made. These are included in a Monte Carlo program to simulate the response of the ANTARES detector to a passing monopole.

4.1 Energy loss of monopoles in water

The ionisation energy loss of magnetic monopoles was briefly discussed in section 3.6.1. A relation for the average ionisation loss of a monopole in a nonconducting material was given in equation 3.6. This relation is valid for monopoles with a velocity $\beta c > 0.1\,c$ and a Lorentz factor $\gamma < 100$. In this velocity range the total energy loss of a monopole is approximately equal to its ionisation energy loss [72]. The relation is used to compute the energy loss of monopoles in the sea water surrounding the ANTARES detector. The sea water is assumed to consist of water molecules only, i.e. contributions of dissolved substances are ignored. The electron density N in the water can then be calculated as

$$N = \rho N_A \frac{Z}{A} \,, \tag{4.1}$$

with $\rho = 1.04$ g/cm^3 the density of the water at the detector site [4], N_A Avogadro's number, and $Z = 10$ and $A = 18$ g/mol the molecular charge and mass numbers of water, respectively. The mean excitation energy I and the density-effect correction δ for water can be found in [89]. The KYG cross-section correction K and the Bloch correction B for monopoles with one Dirac charge $g_D \simeq 137e/2$ (see section 3.1) are 0.406 and 0.248 respectively [69]. The rest mass m_e of the electron is 0.511 MeV/c^2 [24].

The energy loss per unit path length of a monopole with g_D is shown in figure 4.1 as a function of the monopole velocity. It is about 3.5 GeV/cm at $\beta = 0.1$ and increases with the velocity to approximately 13 GeV/cm at $\gamma = 100$.

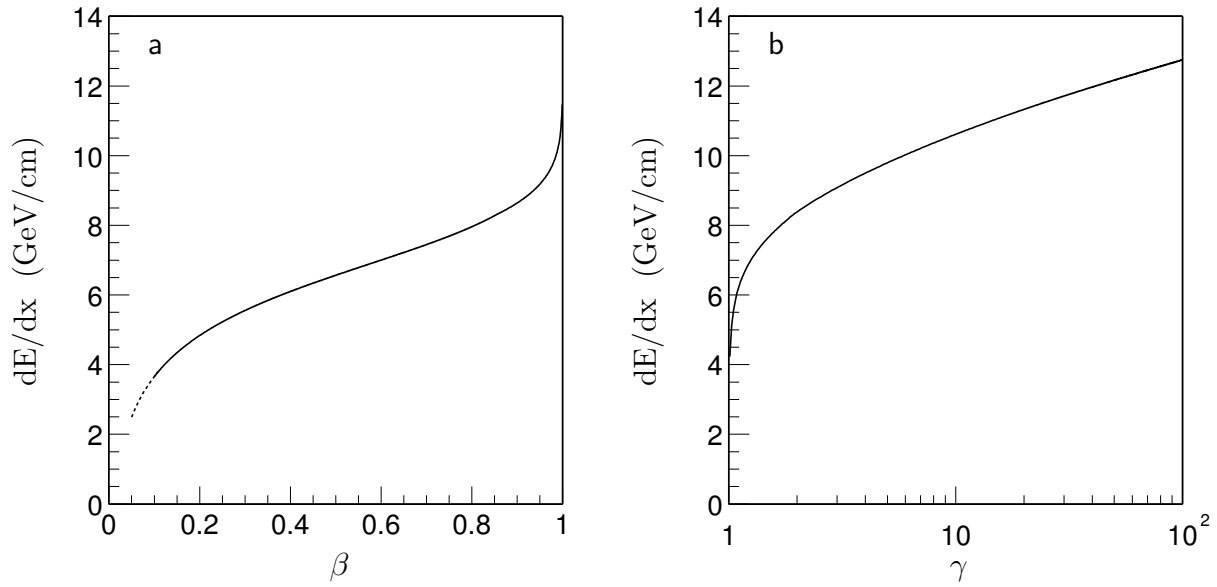

Figure 4.1: *The energy loss of a monopole with one Dirac charge g_D in the sea water as a function of the monopole velocity βc (a) and the monopole's Lorentz factor γ (b). The dashed tail of the curve indicates the limited validity of the underlying assumptions at low β.*

4.2 Cherenkov radiation

A magnetic monopole emits Cherenkov radiation when it passes through a medium with a velocity that is larger than the phase velocity of light in that medium. The phase velocity of light is given by c/n, where n is the refractive index of the medium. In the sea water, n is around 1.35. The minimum monopole velocity for Cherenkov light emission to occur in the water is thus about $0.74\,c$. This threshold velocity will be referred to as the Cherenkov limit.

The spatial symmetry of the Cherenkov light emission by a monopole is the same as for an electric charge due to the symmetry of the underlying physics [71]. The Cherenkov photons are thus emitted at the characteristic Cherenkov angle

$$\cos\theta_c = \frac{1}{\beta n} \tag{4.2}$$

with respect to the direction of the monopole. The number of Cherenkov photons N_γ emitted by a monopole with magnetic charge g per unit path length dx and unit photon wavelength interval $d\lambda$ is

$$\frac{d^2N_\gamma}{dxd\lambda} = \frac{2\pi\alpha}{\lambda^2}\left(\frac{gn}{e}\right)^2\left(1-\frac{1}{\beta^2n^2}\right)\ , \tag{4.3}$$

which is a factor $(gn/ze)^2$ more than that emitted by a particle with electric charge ze and the same velocity [71]. A monopole with g_D and $\beta \simeq 1$ emits about 3×10^6 photons

with wavelengths between 300 and 600 nm per centimetre path length. The corresponding energy loss of the monopole is about 3 MeV/cm, which is only a very small fraction of its total energy loss (see figure 4.1). Nevertheless, Cherenkov radiation provides a detectable signal. The wavelength interval of the photons corresponds to the sensitive range of the photo-multiplier tube that is used in the ANTARES detector (see section 1.2).

4.3 Cherenkov radiation from δ-rays

A monopole that passes through matter loses energy in collisions with the atomic electrons. The energy that is transferred from the monopole to an electron in such a collision may be large enough to knock the electron out of its atomic orbit. The electron may even gain enough kinetic energy to travel a short distance through the medium. These electrons are referred to as knock-on electrons or δ-rays. Like any electrically charged particle, they emit Cherenkov light when their velocity exceeds c/n. An introduction to the Cherenkov light emission by δ-rays can be found in references [90, 12]. The authors of these works use some commonly accepted assumptions for the quantum-mechanical aspects of the interaction between a monopole and an electron. These assumptions have been adapted in the discussion on the δ-ray light production that follows below. However, the assumptions lead to an underestimation of the amount of light that is produced by the δ-rays. This will be discussed in more detail in section 4.6.

4.3.1 Production of δ-rays

For a given velocity βc, the electromagnetic interaction of a monopole with matter can be approximated by that of an electric charge with the substitution $z = g\beta/e$ [68]. Thus, the distribution of δ-rays that are produced by a monopole can be derived from the δ-ray distribution for a heavy electric charge [24]. The number of δ-rays N_e produced by a monopole per unit path length dx and unit energy interval dT_e is then given by

$$\frac{d^2N_e}{dT_e dx} = \frac{2\pi N g^2 e^2}{m_e c^2} \frac{F(T_e)}{T_e^2} \ , \tag{4.4}$$

where T_e is the kinetic energy of the electrons. The form of the factor $F(T_e)$ depends on the spin of the monopole. The expression is valid for secondary electrons with $T_e \gg I$. Since an electron must have a kinetic energy of at least $T_0 = 0.25$ MeV to radiate Cherenkov light in the sea water, and $I = 74$ eV for water [89], the equation can be used to determine the number of δ-rays that produce Cherenkov radiation.

As long as T_e is small compared to the kinetic energy and mass of the monopole, the δ-ray production is independent of the monopole spin [91]. The factor $F(T_e)$ is then equal to that for a spin-0 particle,

$$F(T_e) = \left(1 - \beta^2 \frac{T_e}{T_m}\right) \ , \tag{4.5}$$

where T_m is the classical upper limit on the energy that can be transferred to an atomic electron in a single collision with a monopole. As the mass of the monopole is predicted

to be much larger than the electron mass (see section 3.3), the maximum energy transfer can be approximated by

$$T_m = 2m_e c^2 \beta^2 \gamma^2 \ . \tag{4.6}$$

This expression follows from kinematics and is related to the classical lower limit of the impact parameter* in the Coulomb scattering of an electron by a heavy charged particle [3].

Quantum-mechanical effects in the δ-ray production can be taken into account by carefully considering the lower limit of the impact parameter. For scattering by electrically charged particles, the classical limit is valid when the ratio

$$\eta = \frac{z\alpha}{\beta} \tag{4.7}$$

is larger than 1 [3]. However, when $\eta < 1$ the quantum-mechanical lower limit of the impact parameter must be used, which in this case is larger than the classical one. If it is assumed that an equivalent relation for η holds for magnetic charges with the replacement $z = g\beta/e$, then the lower limit of the impact parameter in the collision of an electron with a monopole with one Dirac charge $g_D = e/2\alpha$ is always determined by the quantum-mechanical limit. The corresponding maximum energy transfer is given by [68]

$$T_{max} \approx 0.69 \cdot T_m \ , \tag{4.8}$$

which should then be used in equation 4.5 instead of T_m. The distribution of δ-rays produced by a monopole then becomes

$$\frac{d^2 N_e}{dT_e dx} = \frac{2\pi N g^2 e^2}{m_e c^2} \left(\frac{1}{T_e^2} - \frac{\beta^2}{T_e T_{max}} \right) \ . \tag{4.9}$$

As follows from equations 4.6 and 4.8, the monopole must have a velocity of at least $0.51\,c$ to be able to produce δ-rays that are energetic enough to emit Cherenkov light.

The distribution of δ-rays that are produced with kinetic energies of at least T_0 by a monopole with g_D in water is shown in figure 4.2 for different monopole velocities. The lower energy limit T_0 of the distribution is the same for all velocities. The upper energy limit is defined by T_{max}, which increases with increasing monopole velocity. At high velocities and δ-ray energies well below T_{max}, the distribution has essentially a $1/T_e^2$ dependence, which is indicated with the dashed line in the figure. Hence, at energy T_0 about $(T_e/T_0)^2$ times more δ-rays are produced per unit energy interval than at energy T_e. For δ-ray energies close to T_{max}, the spectrum differs from the $1/T_e^2$ dependence by a factor of about $(1 - \beta^2)$.

The largest monopole velocity that is considered here corresponds to a Lorentz factor of 10. This limit is related to the assumptions that are made to determine the Cherenkov light emission by δ-rays, as will be discussed below.

*In terms of the impact parameter b, the energy transfer T can be expressed as

$$T(b) \propto \frac{1}{b_{min}^2 + b^2} \ ,$$

where b_{min} is referred to as the lower limit of the impact parameter [3].

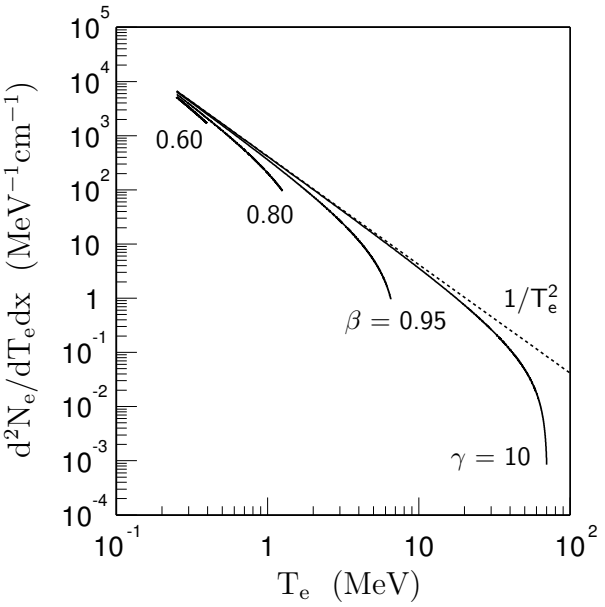

Figure 4.2: *The distribution of δ-rays with kinetic energies above 0.25 MeV produced by a monopole with one Dirac charge g_D passing through water. The distribution is shown for monopole velocities $\beta c = 0.60\,c$, $0.80\,c$, $0.95\,c$ and $\gamma = 10$. The dashed line indicates a spectrum that is proportional to $1/T_e^2$.*

4.3.2 Cherenkov light emission by δ-rays

The total number of δ-rays with energies above T_0 that are produced per unit monopole path in water can be determined by integrating equation 4.9 between T_0 and T_{max}. The result is shown in figure 4.3 as a function of the monopole velocity. The number of δ-rays produced per centimetre is zero at the threshold $\beta \simeq 0.51$, and increases to about 1.7×10^3 at $\beta = 1$ ($\gamma \to \infty$).

The number of Cherenkov photons N_γ that is emitted by a δ-ray in the sea water per unit path length dx_e and unit wavelength interval is given in section 1.1.2. For photons

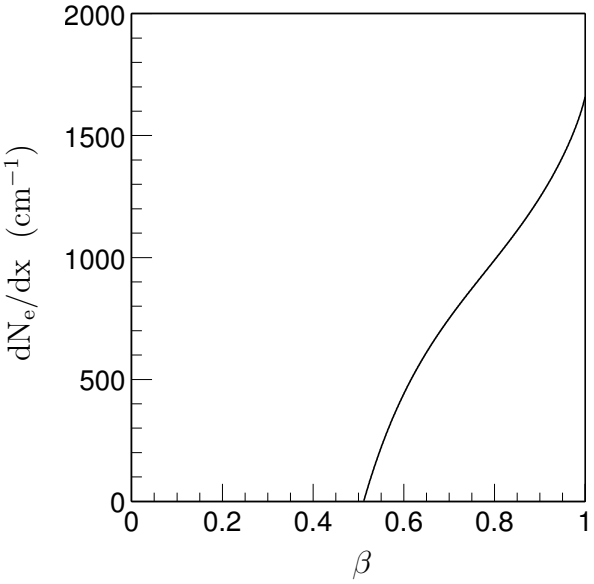

Figure 4.3: *The total number of δ-rays with kinetic energies above 0.25 MeV produced per centimetre path length by a monopole with g_D, as a function of the monopole velocity. The assumed medium corresponds to sea water.*

with wavelengths between 300 and 600 nm, it amounts to about

$$\frac{dN_\gamma}{dx_e} \simeq 764 \left(1 - \frac{1}{\beta_e^2 n^2}\right) \text{ cm}^{-1}, \tag{4.10}$$

where $\beta_e c$ is the velocity of the δ-ray. The total number of photons emitted by a δ-ray thus depends on the δ-ray's velocity and on its path length before its kinetic energy drops below T_0. The δ-ray's path length and velocity depend on its initial kinetic energy and its energy loss in the sea water. Given the relatively low energies of the δ-rays, only the ionisation energy loss is considered here. This is a good approximation of the total energy loss of a δ-ray up to the so-called critical energy. The critical energy is the energy at which the ionisation loss becomes equal to the energy loss due to bremsstrahlung. In water, the critical energy of an electron is about 70 MeV [24]. As follows from equations 4.8 and 4.6, the present calculation is thus valid for monopoles with Lorentz factors up to about 10.

The ionisation energy loss of a δ-ray can be described by the parameterisation given in [92]. It can then be expressed as

$$\frac{dE_e}{dx_e} = \frac{2\pi N e^4}{m_e c^2 \beta_e^2} \left(B(T) - 2\ln\frac{I}{m_e c^2} - \delta\right) , \tag{4.11}$$

where T is the kinetic energy of the δ-ray as it moves through the water, δ is the density-effect correction, and the factor $B(T)$ depends only on the kinetic energy as

$$B(T) = \ln\frac{\tau^2(\tau^2+2)}{2} + \frac{1 + \tau^2/8 - (2\tau+1)\ln 2}{(\tau+1)^2} , \tag{4.12}$$

with $\tau = T/m_e c^2$. The total number of Cherenkov photons N_γ emitted by a δ-ray with initial kinetic energy T_e can then be calculated as

$$N_\gamma = \int_{T_0}^{T_e} \frac{dN_\gamma}{dx_e} \left(\frac{dE_e}{dx_e}\right)^{-1} dE_e . \tag{4.13}$$

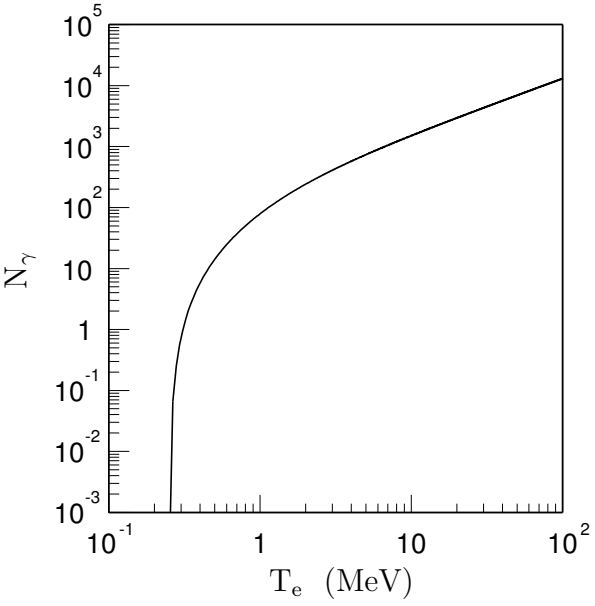

Figure 4.4: *The total number of Cherenkov photons with wavelengths between 300 and 600 nm emitted by a δ-ray with initial kinetic energy T_e. The assumed medium corresponds to sea water.*

The result is shown in figure 4.4 as a function of T_e. The number of Cherenkov photons rises approximately linearly with T_e above about 5 MeV, and it falls off rapidly to zero for T_e approaching T_0.

The total number of Cherenkov photons n_γ that is emitted by all δ-rays that are produced per unit path length of a monopole can be determined with

$$\frac{dn_\gamma}{dx} = \int_{T_0}^{T_{max}} \frac{d^2N_e}{dT_e dx} \int_{T_0}^{T_e} \frac{dN_\gamma}{dx_e} \left(\frac{dE_e}{dx_e}\right)^{-1} dE_e dT_e \ . \tag{4.14}$$

This is shown in figure 4.5 as a function of the monopole velocity. It is assumed that the δ-rays do not act coherently, nor that destructive interference occurs. The Cherenkov light that is emitted directly by a monopole (see section 4.2) and by a minimum ionising muon (see section 1.1.2) are also shown in the figure. The amount of light emitted by the δ-rays increases with increasing monopole velocity. Above $\beta \simeq 0.6$, it exceeds the direct light yield of a muon. This indicates that detection of monopoles below the Cherenkov limit may be possible. The number of photons emitted by the δ-rays is about 2×10^5 per centimetre path at $\gamma = 10$, which is only a factor of about 10 less than the direct emission by a monopole at this velocity.

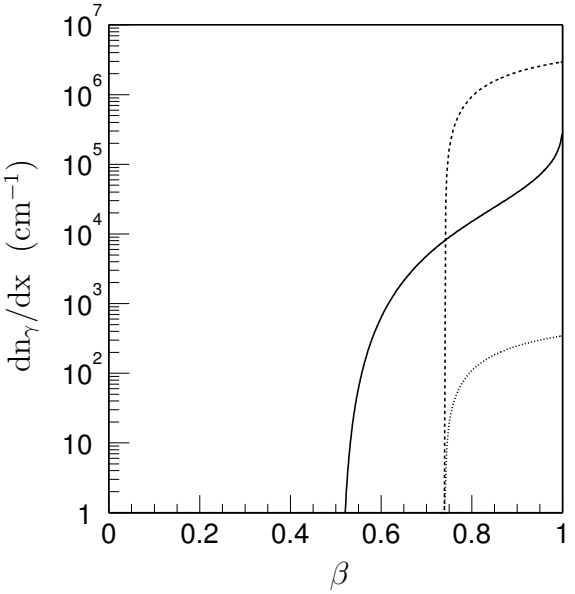

Figure 4.5: *The total number of Cherenkov photons with wavelengths between 300 and 600 nm emitted by δ-rays that are produced per centimetre path length by a monopole with g_D (solid line), as a function of the monopole velocity. The number of Cherenkov photons emitted directly by a monopole (dashed line) and by a minimum ionising muon (dotted line) are also shown as a function of the velocity.*

4.3.3 Angular distributions of the δ-ray light

The δ-rays are produced at an angle θ_e with respect to the direction of the monopole. This angle is determined by the kinematics of the collision between the monopole and the electron. It can be expressed as

$$\cos\theta_e = \frac{1}{\beta}\sqrt{\frac{T_e}{T_e + 2m_e c^2}} \ . \tag{4.15}$$

It only depends on the velocity of the monopole and on the kinetic energy of the δ-ray. The angular distribution of the δ-rays produced in the sea water is shown in figure 4.6 as a function of $\cos\theta_e$ for different monopole velocities. The δ-rays that are produced at the largest possible angles, i.e. the left limit of the distributions in the figure, are those with the smallest kinetic energy, T_0. The δ-rays with the largest kinetic energy, T_{max}, are produced at the smallest possible angles. This corresponds to the right limit of the distributions in the figure. A uniform distribution of the δ-rays in the azimuthal angle ϕ_e around the monopole path is assumed because of the rotational symmetry of the monopole field.

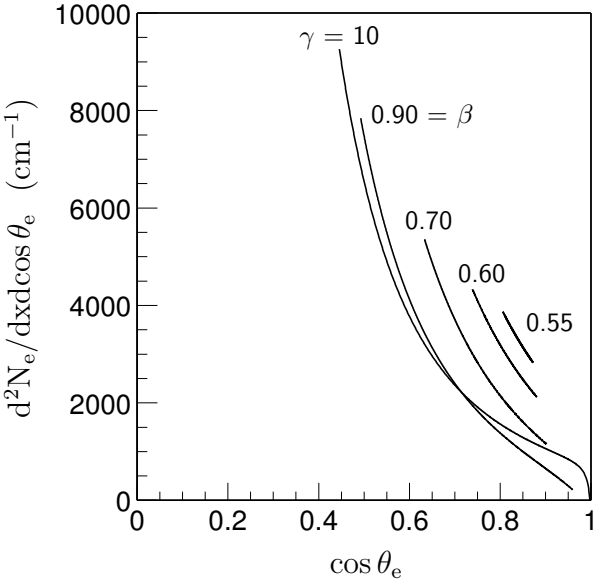

Figure 4.6: *The angular distribution of δ-rays with kinetic energies above 0.25 MeV produced by a monopole with g_D, as a function of their production angle θ_e. The distribution is shown for monopole velocities $\beta c = 0.55\,c$, $0.60\,c$, $0.70\,c$, $0.90\,c$ and $\gamma = 10$.*

The Cherenkov photons are emitted at the characteristic Cherenkov angle θ_c with respect to the direction of the δ-ray. The Cherenkov angle can be expressed as

$$\cos\theta_c = \frac{1}{n\sqrt{1 - m_e^2c^4/(m_ec^2 + T)^2}} \ , \tag{4.16}$$

where T is the kinetic energy of the δ-ray as it passes through the water. The photons are distributed uniformly in the azimuthal angle ϕ_c around the path of the δ-ray.

The δ-ray production angle θ_e and the Cherenkov angle θ_c can be combined to determine the emission angle θ_γ of the δ-ray photons with respect to the direction of the monopole,

$$\cos\theta_\gamma = \sin\theta_e \sin\theta_c \cos\phi_c + \cos\theta_e \cos\theta_c \ . \tag{4.17}$$

Since both θ_e and θ_c are related to the kinetic energy of the δ-rays, the integral in equation 4.14 can be used to obtain the angular distribution of the photons in θ_γ. The result is shown in figure 4.7. It is assumed here that the angle between the δ-ray and the monopole is constant for the entire path of the δ-ray, i.e. the directional deviations of the δ-ray due to multiple scattering are ignored. The photons have a uniform distribution in the azimuthal angle.

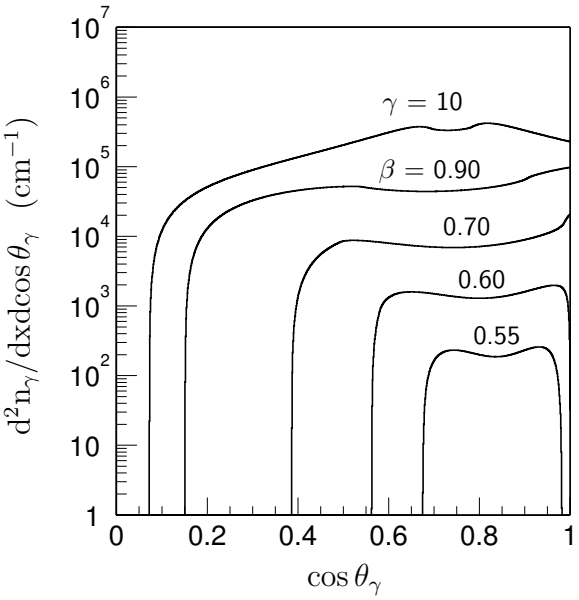

Figure 4.7: *Angular distributions of the Cherenkov photons emitted by the δ-rays that are produced per centimetre path length by a monopole with g_D in the sea water, as a function of the emission angle θ_γ between the photons and the monopole. The angle between the δ-rays and the monopole is assumed to be constant. The distribution is shown for $\beta = 0.55$, 0.60, 0.70, 0.90 and $\gamma = 10$.*

The angular spread of the photon emission in θ_γ increases with increasing velocity. Nevertheless, all photons are still emitted in forward directions with respect to the monopole, i.e. in directions with $\cos\theta_\gamma > 0$.

As a δ-ray passes through the water, it is deflected continuously due to multiple scattering off atomic electrons and nuclei. The distribution of the corresponding scattering angle can be approximated by a Gaussian distribution with standard deviation [93]

$$\theta_0 = \frac{13.6\ \text{MeV}}{E_e \beta_e^2} \sqrt{\frac{x_e}{X_0}} \left(1 + 0.038 \ln \frac{x_e}{X_0}\right) , \tag{4.18}$$

where E_e is the total energy of the δ-ray, x_e is the distance it travelled and $X_0 = 36.1$ cm is the radiation length of water [94]. As follows from this relation, the δ-ray undergoes larger scattering at lower energies. The scattering thus increases along the path of the δ-ray due to the δ-ray's energy loss. When multiple scattering of the δ-rays is taken into account, the angle between the δ-rays and the monopole varies continuously, which results in a larger angular spread of the Cherenkov photon emission. This is reflected by the angular distributions shown in figure 4.8. For monopole velocities above $0.60\,c$, the photons can even be emitted in backward directions.

The angular distribution for $\gamma = 10$ has a peak at $\cos\theta_\gamma \simeq 0.74$. This is due to the contribution of the most energetic δ-rays at this velocity, which are produced in directions very close to the monopole direction. Due to their relatively high energies, these δ-rays travel larger distances and are less influenced by multiple scattering than less energetic δ-rays. They emit a considerable number of Cherenkov photons at the typical Cherenkov angle $\cos\theta_c \simeq 0.74$, of which many are thus emitted at the same angle with respect to the monopole direction.

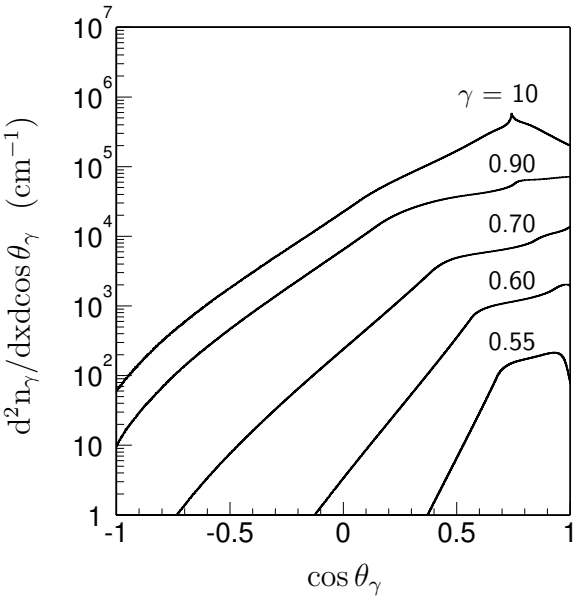

Figure 4.8: *Angular distributions of the Cherenkov photons (see figure 4.7) with multiple scattering of the δ-rays taken into account.*

4.4 Monopoles traversing the detector

Monopoles approaching the Earth are accelerated by the geomagnetic field. The change in kinetic energy of a monopole with Dirac charge g_D due to this field is of the order of 10^3 GeV [66]. With an assumed monopole mass of at least 10^7 GeV (see section 3.3), this change in energy can be considered negligible.

Since monopoles interact heavily with matter (see section 3.6.1), they can lose large amounts of energy in the terrestrial environment. The total energy loss of a relativistic monopole with one Dirac charge that crosses the full diameter of the Earth[†] is of the order of 10^{11} GeV [95]. Because monopoles can be accelerated in the cosmos to kinetic energies of about 10^{15} GeV (see section 3.4), they can be capable of crossing the Earth and reach the ANTARES detector from below. This indicates that monopoles can reach the detector from any direction, as most energy is lost in crossing the full Earth. However, when reaching the detector they must have a velocity of at least $0.51\,c$ to be able to produce light. This velocity corresponds to a Lorentz factor of about 1.16. Consequently, only monopoles with masses below approximately 10^{15} GeV can be fast enough to produce a detectable signal.

The maximum distance that is covered by the sensitive volume of the detector is about 400 m. The corresponding energy loss of monopoles with $\beta \gtrsim 0.51$ and $\gamma \lesssim 10$ is about 4×10^5 GeV (see figure 4.1). In most cases, this is small compared to their total kinetic energy[‡]. Furthermore, multiple scattering of monopoles can be considered negligible due

[†]The energy loss in the Earth's atmosphere is neglected, since its density is at least a factor 1000 less than that of rock.

[‡]For a monopole with $\beta \simeq 0.51$ and the lowest predicted mass of 10^7 GeV, the maximum energy loss in the detector is about 20% of its kinetic energy. This fraction decreases rapidly with increasing velocity and mass.

to their large mass (see equation 4.18). It is therefore assumed that monopoles travel through the detector in a straight line and with a constant velocity.

4.5 Simulation of monopole signals

The Monte Carlo program GEASIM (see section 1.8.3) has been adapted to simulate the response of the detector to monopole signals. The program performs tracking of monopoles through a cylindrical volume surrounding the detector, simulating the emission, propagation and detection of the direct and δ-ray induced Cherenkov light. Only photons with wavelengths between 300 and 600 nm are considered, as these correspond to the sensitive range of the PMTs. The monopoles are simulated as straight, through-going tracks and are generated in the velocity range $\beta \geq 0.55$ and $\gamma \leq 10$. The directions of the generated monopoles are distributed uniformly over the hemisphere above and below the detector.

The cylindrical volume around the instrumented detector volume in which the simulation is performed, is referred to as the can. It extends typically a few absorption lengths beyond the instrumented volume to include light that is produced outside the detector. In the case of monopoles, the can volume needs to be enlarged because of the very intense Cherenkov radiation.

The direct Cherenkov light emission is simulated for monopoles with $\beta > 1/n \simeq 0.74$. Equations 4.2 and 4.3 are used to calculate the velocity-dependent emission angle and light yield on the monopole track. The propagation of the direct light is simulated in accordance with the known decrease of the light intensity I with the photon path length r, which is given by

$$I(r) \propto \frac{1}{r} e^{-r/\lambda_{abs}} \ . \tag{4.19}$$

Here, λ_{abs} is the absorption length of light in the sea water. The absorption length and consequently the light intensity depend on the wavelength of the light. This dependence is taken into account in the simulation.

The δ-ray induced Cherenkov light emission is simulated for monopoles with $\beta \geq 0.55$. The emission angle and light yield are determined from the angular distribution of the Cherenkov photons as shown in figure 4.8. The distribution has been determined for 10 monopole velocities in the range $\beta \geq 0.55$ and $\gamma \leq 10$. Logarithmic interpolation is used to determine the δ-ray light emission by monopoles with velocities for which no distribution is available. Since the path lengths of the δ-rays are generally much smaller than the typical distance between the monopole track and the point where the light is detected[§], this distance is calculated assuming that the photons are emitted from the monopole track. The propagation of the δ-ray light is simulated taking into account the decrease of the δ-ray light intensity I_e with the photon path length. The decrease can be expressed as

$$I_e(r) \propto \frac{1}{r^2} e^{-r/\lambda_{abs}} \tag{4.20}$$

[§]The path length of a δ-ray increases with its kinetic energy. For a monopole with $\gamma \leq 10$, the largest δ-ray energy is about 70 MeV (see section 4.3.2). The corresponding path length is about 0.3 m.

because of its approximately isotropic nature (see figure 4.8).

The simulated response of the detector to monopole signals is summarised in figures 4.9 to 4.11 for different monopole velocities. For each velocity, the same sample of 2000 upward going monopole tracks was used. The distance between the can surface and the instrumented volume was 200 m. In the figures, only monopoles that produced hits on at least 5 different PMTs have been considered. In the following, a hit is defined as a pulse of light that is detected by a PMT which is separated in arrival time from other light pulses by at least 1 ns. Thus, the effect of the read-out electronics is not taken into account.

Figure 4.9 shows the number of hits produced by monopoles with $\beta = 0.65$, 0.75, 0.85, 0.95. The number of hits increases with the monopole velocity, as does the fraction of monopoles that produce hits. This is due to the increasing light yield as monopoles move faster, as is shown in figure 4.5.

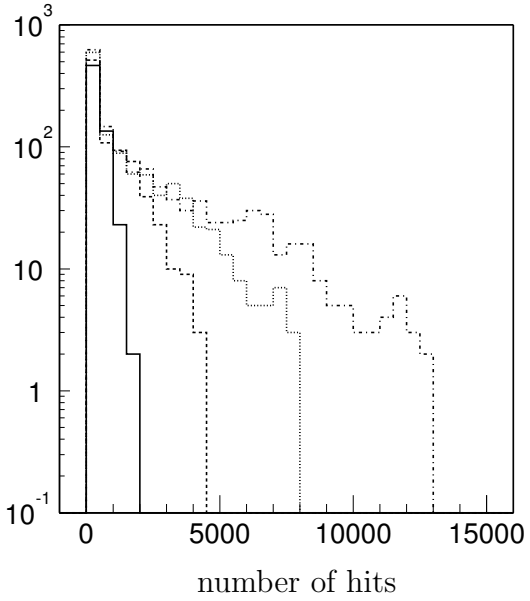

Figure 4.9: *The number of hits that are produced in the detector by monopoles with β = 0.65 (solid line), 0.75 (dashed line), 0.85 (dotted line) and 0.95 (dash-dotted line).*

As can be expected from figure 4.5, the number of detected photons from a monopole with a velocity above the Cherenkov limit is dominated by the direct Cherenkov light emitted by the monopole. This is reflected by the ratio of the number of detected δ-ray photons to the number of detected direct photons, which is shown in figure 4.10a for velocities $0.85\,c$ and $0.95\,c$. The ratio is significantly smaller than 1 for both velocities. Only photons that are detected within a radius of one absorption length around the monopole track have been considered. The number of hits produced within this radius, however, is primarily due to the light emitted by the δ-rays. This follows from figure 4.10b, which depicts the ratio of the number of hits due to δ-ray light to the number of hits due to direct light. This ratio is considerably larger than 1 for both velocities. These features are caused by the difference in angular distribution and light yield of the two types of light emission. The very intense direct Cherenkov light is concentrated in a narrow cone, which results in relatively few hits with very large amplitudes. The less

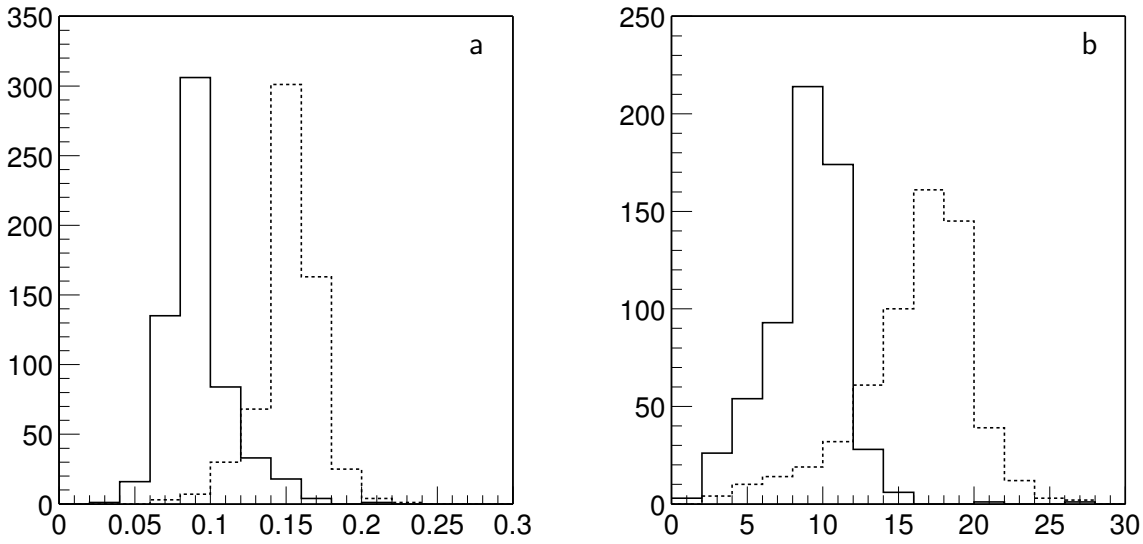

Figure 4.10: *The ratio of detected δ-ray photons to detected direct photons (a), and the ratio of δ-ray hits to direct hits (b), for monopoles with velocities 0.85 c (solid line) and 0.95 c (dashed line).*

intense δ-ray light has a much wider angular distribution, which produces many separate hits with relatively small amplitudes.

The effect of the different angular distributions is also evident in the arrival times of the photons on the PMTs. Figure 4.11a shows the time difference between the first and last hit on a PMT due to direct and δ-ray light separately for monopoles with $\gamma = 10$. PMTs with only one hit are included, which causes a peak at zero. Almost all direct hits occur within 20 ns after the first hit, whereas the time difference between δ-ray hits can run up to several hundreds of nanoseconds. The time difference for both light contributions combined is shown in figure 4.11b for monopoles with $\beta = 0.55$, 0.65, 0.85 and $\gamma = 10$. The spread in arrival times decreases with the monopole velocity. This is due to the smaller angular spread of the δ-ray light at lower velocities, as shown in figure 4.8.

The intense light produced by monopoles can result in the simultaneous arrival of many thousands of photons on a PMT. This causes a large current in the PMT, which may result in the collapse of the PMT's high voltage and consequently in some dead-time of the PMT. This possible saturation of the PMTs is not included in the simulation. Furthermore, the measurement of the charge contained in a PMT signal is limited by the dynamic range of the ARS chip. In this simulation, this dynamic range is set to 12 p.e.

The monopole simulation described in this section is based on the direct and δ-ray induced Cherenkov light emission by monopoles with one Dirac charge g_D. This is the basic unit of magnetic charge, larger magnetic charges g are an integer multiple k of this, $g = k\, g_D$. Since the direct and δ-ray light yield are proportional to the square of the magnetic charge (see equations 4.3 and 4.9), the simulation can also be used for

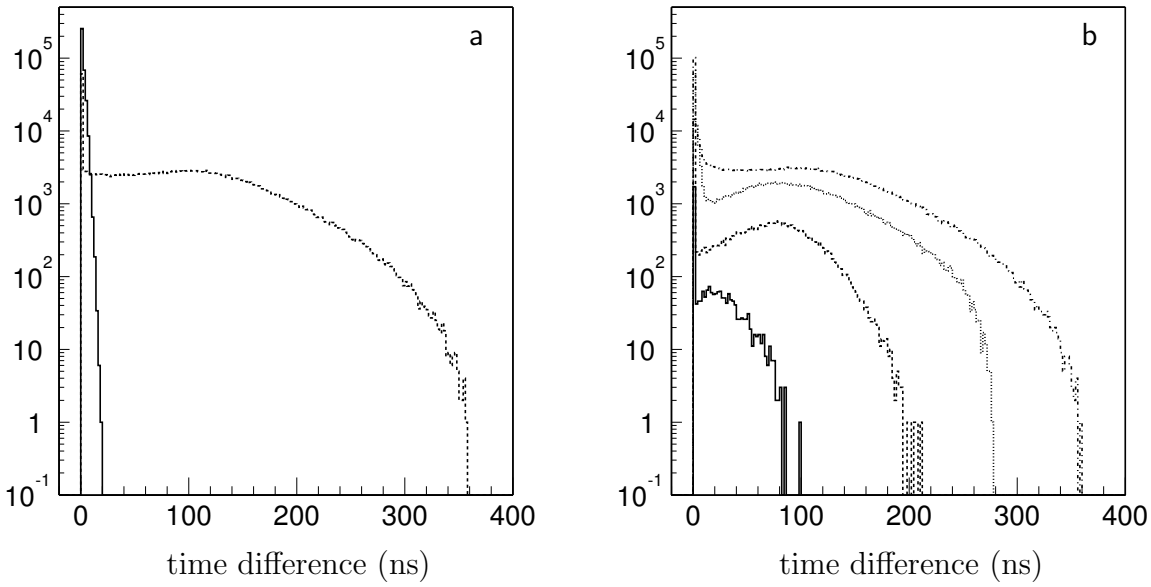

Figure 4.11: *a: The time difference between the first and last hit on a PMT due to direct light (solid line) and δ-ray light (dashed line) for monopoles with γ = 10. b: The time difference between the first and last hit on a PMT due to both types of light combined, for monopole velocities 0.55 c (solid line), 0.65 c (dashed line), 0.85 c (dotted line) and γ = 10 (dash-dotted line).*

monopoles with larger charges by multiplying the light yield with k^2. It is assumed here that the quantum-mechanical lower impact parameter also prevails for these monopoles. Moreover, the simulation can be used for any heavy particle with electric charge ze. The direct Cherenkov light emission by such a particle is related to that of a monopole by a factor $(ze/gn)^2$, and the δ-ray Cherenkov light production by a factor $(ze/g\beta)^2$.

4.6 Discussion

The cross section per unit energy interval for energy loss T by a heavy incident particle with electric charge ze in a Coulomb collision with a free stationary electron can be given by [3]

$$\frac{d\sigma}{dT} = \frac{2\pi z^2 e^4}{m_e c^2 \beta^2 T^2} \ . \tag{4.21}$$

This cross section derives from the Rutherford scattering formula, and is valid for close collisions and nonrelativistic velocities of the incident particle. It can be used for actual collisions in matter when T is (much) larger than the mean excitation energy I, so that the atomic electrons can be considered as free. For relativistic velocities, the effect of the electron spin in the collision needs to be taken into account. This gives a correction to

the energy loss cross section,

$$\left(\frac{d\sigma}{dT}\right)_M = \frac{2\pi z^2 e^4}{m_e c^2 \beta^2 T^2}\left(1 - \beta^2 \frac{T}{T_m}\right) , \tag{4.22}$$

where T_m is the classical maximum energy transfer given by equation 4.6. The relation is the energy-loss equivalent of the so-called Mott cross section. It forms the basis of the δ-ray distribution that is used in section 4.3 to calculate the δ-ray production by monopoles. In that calculation, quantum effects are taken into account by using a quantum-mechanical limit on the maximum energy transfer, given by T_{max} in equation 4.8. However, the Mott cross section is already quantum-mechanically correct with the use of the classical energy transfer T_m. Thus, a more consistent calculation of the δ-ray production involves the use of T_m instead of T_{max}. This has certain consequences. Firstly, it gives a harder δ-ray energy spectrum and a larger number of δ-rays that are produced above the Cherenkov limit. This results in the emission of more Cherenkov photons per unit monopole path than shown in figure 4.5. Secondly, the minimum velocity with which monopoles can produce δ-rays above the Cherenkov limit decreases to about $0.44\,c$. And finally, the angular distributions of the δ-rays change. As follows from equation 4.15, the upper limit on the δ-ray production angle becomes $\cos\theta_e = 1$ for all monopole velocities. This influences the angular distribution of the δ-ray light emission, which will have a different shape than the distributions shown in figure 4.8.

As has been mentioned in section 4.3, the use of the Mott cross section with the substitution $z = g\beta/e$ gives an approximation of the δ-ray production by monopoles. A more accurate result is obtained by using the cross section for the scattering of an electron by a relativistic magnetic monopole as described in [70]. This so-called KYG cross section is quantum-mechanically valid, and its energy-loss equivalent can be given by

$$\left(\frac{d\sigma}{dT}\right)_{KYG} = \frac{2\pi g^2 e^2}{m_e c^2 T^2} F(T) , \tag{4.23}$$

where the functional form of the factor $F(T)$ depends mildly on the charge of the monopole. It is shown as a function of T/T_m in figure 4.12a for monopoles with one Dirac charge, with T_m again the classical maximum energy transfer. The factor is about 1 for energy transfers well below T_m, and increases to approximately 2 for energy transfers close to T_m. This differs from the relativistic spin correction in the Mott cross section, which decreases from 1 at $T \ll T_m$ to about $(1-\beta^2)$ at $T \simeq T_m$. Hence, the KYG cross section gives a harder δ-ray spectrum than the Mott cross section.

The total number of Cherenkov photons emitted by the δ-rays that are produced by a monopole in the sea water is shown in figure 4.12b for a δ-ray distribution that is based on the Mott cross section with the use of T_{max} (I), the Mott cross section with the use of T_m (II), and the KYG cross section (III). Case (I) is the result of the calculation presented in section 4.3 which is also shown in figure 4.5. As can be seen from figure 4.12b, it is a conservative estimate of the δ-ray light yield compared to the other two cases. Nevertheless, this result is used in the remainder of this thesis for three reasons. First, the choice to use T_{max} instead of the more correct T_m is consistent with earlier work carried out in ANTARES [90, 12] and other neutrino telescope experiments [96, 86].

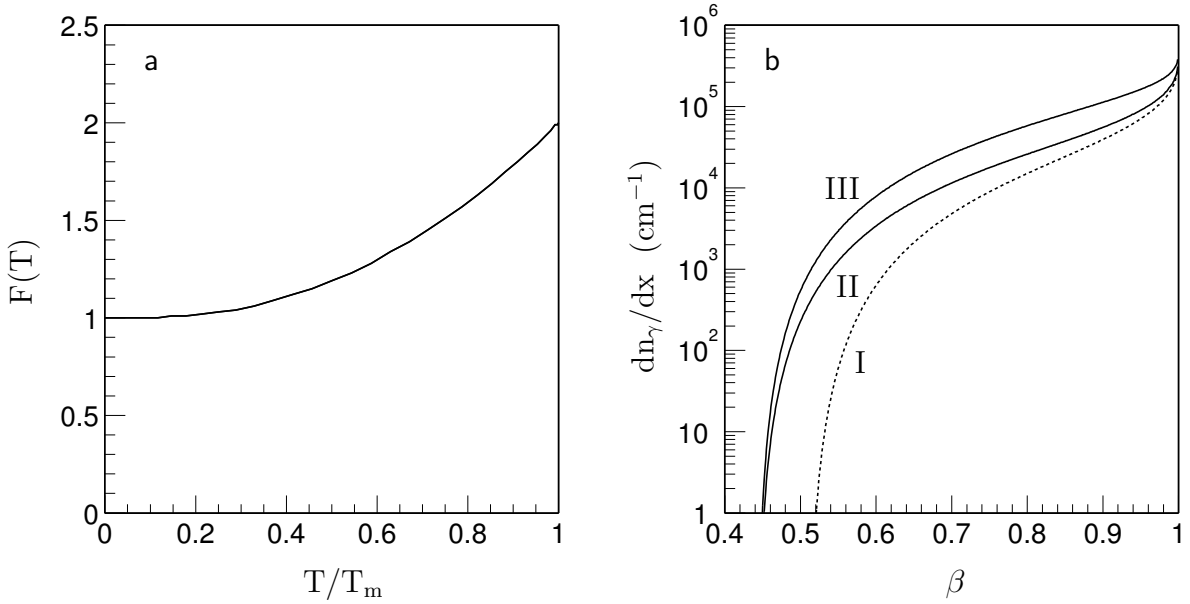

Figure 4.12: *a: The form of the factor $F(T)$ in equation 4.23 as a function of T/T_m. b: The δ-ray light yield of monopoles for a δ-ray spectrum derived from the Mott cross section with T_{max} (I), the Mott cross section with T_m (II), and the KYG cross section (III) (see text).*

Second, the use of the Mott cross section allows the application of the simulation for slowly moving electrically charged particles. Third, for obvious reasons, the result can be considered as a safe estimate of the light yield.

Chapter 5

Monopole trigger

The raw data coming from the detector are filtered on shore by a fast trigger algorithm that searches for muon signals in the data. It will be shown in this chapter, that this standard muon trigger is inefficient in finding signals of magnetic monopoles that have velocities below the Cherenkov limit. Therefore, a new trigger has been developed in order to find the signals of these relatively slow monopoles. The causality relations that have been derived for this trigger are explained in this chapter. Ways to suppress background due to random and atmospheric muon signals are presented. The performance of the trigger is quantified in terms of detection efficiency, speed and purity of the used hit selection.

5.1 Muon trigger efficiency for monopoles

The muon trigger is described in detail in section 1.5. It searches for correlations between hits in the raw data based on the properties of the Cherenkov light emission by a muon. These properties can be summarised in the causality relations given in equations 1.5 and 1.8. It is assumed in these relations that the muon travels with the speed of light c and that the Cherenkov photons are emitted at a fixed angle with respect to the direction of the muon. As was shown in the previous chapter, magnetic monopoles are capable of producing a detectable signal at velocities down to about $0.5\,c$. Furthermore, the light emitted by monopoles has a considerable angular spread. Consequently, the time-position correlations between hits caused by a monopole can be different from those between hits due to a muon.

This effect can be seen in the efficiency with which the standard muon trigger finds monopole signals in the detector. This efficiency has been determined with the simulation of the detector response to monopole signals described in the previous chapter. The standard cuts in the muon trigger have been used, which are a minimum cluster size of 5 and a maximum transverse distance of 90 m. The efficiency is defined as the fraction of monopole events with at least 5 L1 hits on at least 5 different storeys that is detected by the trigger. The efficiency is shown in figure 5.1 as a function of the monopole velocity βc. It is nearly 100% for monopoles with velocities above the Cherenkov limit, which is approximately $0.74\,c$. For velocities below this limit, the efficiency decreases to about 10% at $0.55\,c$. This is due to the characteristics of the light emission and the velocity of

these monopoles, which do not satisfy the causality relations for muon signals. Hence, the detection of monopoles below the Cherenkov limit requires a different trigger method.

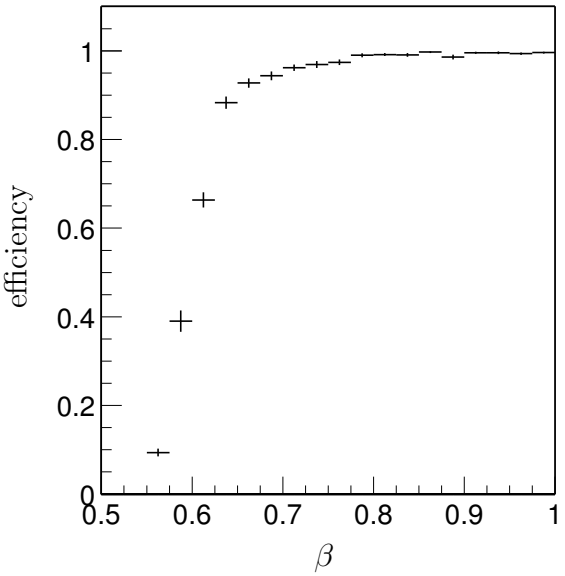

Figure 5.1: *The efficiency of the muon trigger for magnetic monopoles as a function of the monopole velocity βc. The efficiency is defined as the fraction of monopole events with at least 5 L1 hits on at least 5 different storeys that is detected by the trigger.*

5.2 Trigger for monopoles below the Cherenkov limit

A new separate trigger has been developed that is dedicated to the detection of monopoles with velocities below the Cherenkov limit. These monopoles are detectable through the Cherenkov light emission by the δ-rays that they produce. Since the monopole velocity is unknown beforehand, the monopole trigger should be sensitive to a wide velocity range. The minimum velocity of this range is denoted as $\beta_{min}c$, the maximum velocity as $\beta_{max}c$. The logic of the monopole trigger is the same as that of the muon trigger. This means, that the trigger consists of three successive steps in which hits are selected that are possibly related to a monopole signal.

The first step consists of the selection of level 1 (L1) hits. These hits are either a local coincidence, or they have a large charge. This step is incorporated in the decoding of the raw data. The resulting set of L1 hits is used as an input for higher level triggering based on time-position correlations. Consequently, the selection of L1 hits in the monopole trigger is identical to that in the muon trigger.

In the second step, the trigger algorithm searches for correlated L1 hits from a monopole from any direction. For monopoles below the Cherenkov limit, the slowest possible speed with which the monopole signal propagates through the detector is the velocity of the monopole itself*. Thus, two different L1 hits are assumed to be correlated when their time difference Δt satisfies the causality relation

$$|\Delta t| \leq \frac{d}{\beta_{min} c} + \frac{L}{c}\left(\frac{1}{\beta_{min}} - n_g\right) \ , \tag{5.1}$$

*This is not true for monopoles very close to the Cherenkov limit, see below.

where d is the three-dimensional distance between the storeys on which the hits occur, c/n_g is the group velocity of light in the sea water and $\beta_{min}c$ is the minimum monopole velocity to be detected. The second term in the right hand side of the equation is related to the emission of photons along the monopole direction and will be explained below. An extra time window of 20 ns is added to account for uncertainties in the time and position calibration. A group of correlated L1 hits that is found by the algorithm is called a cluster.

In the third stage of the trigger, a loop over a set of predefined directions is implemented. For each direction, a more stringent causality relation is applied to search for correlated L1 hits from a monopole that travels in the given direction. Only L1 hits that are in a cluster are considered. The causality relation is derived from the topology of the δ-ray induced Cherenkov light emission by the monopoles. The topology is shown schematically in figure 5.2 for a monopole that travels in the z-direction. As is shown in figure 4.8, the angle at which the δ-ray light is emitted with respect to the direction of the monopole varies between 0 and 180 degrees. However, for monopoles with $\beta < 1/n$ more than 98% of the photons is emitted in forward directions, i.e. between 0 and 90 degrees. In order to keep the time window of the causality relation as small as possible, only these photons are considered here. Hence, the angles θ_1 and θ_2 in figure 5.2 can vary between 0 and 90 degrees.

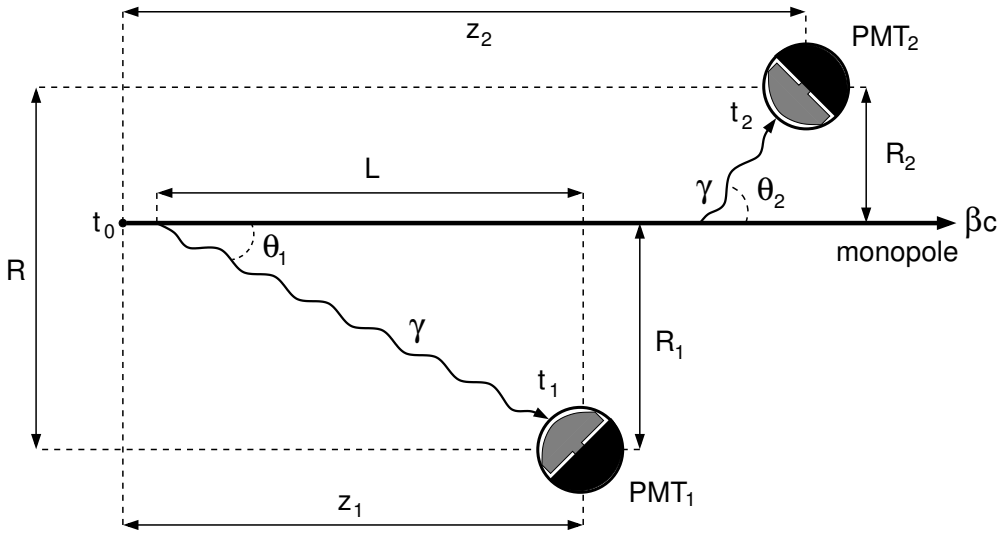

Figure 5.2: *The topology of the light emission by a monopole that travels in the z-direction with velocity βc. The photons that are emitted under an angle θ_j can be detected by a PMT$_j$ on a position along the monopole path. The position of PMT$_j$ can be expressed in terms of the distance z_j to the monopole position at time t_0, and the distance of closest approach R_j to the monopole path.*

According to figure 5.2, the expected arrival time t_j of a photon on PMT$_j$ can be given by

$$t_j = t_0 + \frac{z_j}{\beta c} + \frac{R_j}{c}\left(\frac{\beta n_g - \cos\theta_j}{\beta \sin\theta_j}\right) \ , \tag{5.2}$$

where t_0 is some reference time, z_j is the difference between the z-co-ordinates of the

monopole position at time t_0 and the position of PMT$_j$, βc is the velocity of the monopole, R_j is the minimum distance of approach between PMT$_j$ and the monopole path, and θ_j is the emission angle of the photon. The difference between the arrival times t_1 and t_2 of two photons on two different PMTs can then be written as

$$t_2 - t_1 = \frac{z_2 - z_1}{\beta c} + \frac{R_2}{c}\left(\frac{\beta n_g - \cos\theta_2}{\beta \sin\theta_2}\right) - \frac{R_1}{c}\left(\frac{\beta n_g - \cos\theta_1}{\beta \sin\theta_1}\right) . \tag{5.3}$$

The angles θ_1 and θ_2 at which the photons are emitted are not known a priori. The difference in arrival time is therefore not uniquely defined by the positions of the PMTs, like in the case of a muon. However, an estimate of the minimum and maximum time differences can be obtained. Because the photons travel faster than the monopole, the earliest arrival time occurs when a PMT detects photons that are emitted parallel to the path of the monopole. These photons are thus emitted at an angle of 0 degrees. As the emission angle increases, the arrival time of the photons becomes later. Photons that are emitted at an angle of 90 degrees arrive the latest. Hence, the maximum time difference between two hits occurs when PMT$_1$ detects photons that are emitted at $\theta_1 = 0$ degrees and PMT$_2$ detects photons emitted at $\theta_2 = 90$ degrees. This implies that the monopole track crosses PMT$_1$, in which case $R_1 = 0$ and $R_2 = R$, with R the two-dimensional distance between the PMT positions projected on a plane perpendicular to the direction of the monopole. With $\theta_1 = 0$, the third term in the right hand side of equation 5.3 blows up. This is because the attenuation of light in the sea water has not been taken into account. In that case, photons can be detected that are emitted at a point along the monopole track that is infinitely far away. The corresponding term is therefore rewritten with the use of $R_1 = L\tan\theta_1$, with L the longitudinal distance between the PMT and the point on the track where the photons are emitted. The maximum difference between the arrival times can then be written as

$$(t_2 - t_1)_{max} = \frac{z_2 - z_1}{\beta c} + \frac{R n_g}{c} + \frac{L}{c}\left(\frac{1}{\beta} - n_g\right) , \tag{5.4}$$

where the value of L is limited to a few absorption lengths of the light in the sea water. The first term in the right hand side of equation 5.4 is the time that the monopole needs to travel between the PMTs. The second term corresponds to the time that the photons need to cover the transverse distance between the PMTs. The third term is the difference between the arrival times of the monopole and the photons at the first PMT. This term also needs to be taken into account in the three-dimensional triggering, and is therefore present in equation 5.1.

The situation in which the monopole crosses PMT$_2$ (θ_1 and θ_2 are 90 and 0 degrees respectively) gives an estimate of the minimum difference between two arrival times. Since no assumption is made on the position of the monopole path, the time difference between two hits produced by a monopole that travels in the z-direction must then satisfy

$$\frac{z_2 - z_1}{\beta c} - \frac{R n_g}{c} - \frac{L}{c}\left(\frac{1}{\beta} - n_g\right) \leq t_2 - t_1 \leq \frac{z_2 - z_1}{\beta c} + \frac{R n_g}{c} + \frac{L}{c}\left(\frac{1}{\beta} - n_g\right) . \tag{5.5}$$

This time window is valid for monopoles with a given velocity βc. However, the trigger should be sensitive to the velocity interval between $\beta_{min} c$ and $\beta_{max} c$. This requires a

modification of the time window, because the minimum and maximum time differences between two hits are determined either by β_{min} or by β_{max}, depending on the value of $z_2 - z_1$. Three situations can be distinguished in order to optimise the time window:

- $z_2 - z_1 \geq L$:

$$\frac{z_2 - z_1}{\beta_{max} c} - \frac{R n_g}{c} - \frac{L}{c}\left(\frac{1}{\beta_{max}} - n_g\right) \leq t_2 - t_1 \leq \frac{z_2 - z_1}{\beta_{min} c} + \frac{R n_g}{c} + \frac{L}{c}\left(\frac{1}{\beta_{min}} - n_g\right) \quad (5.6)$$

- $z_2 - z_1 \leq -L$:

$$\frac{z_2 - z_1}{\beta_{min} c} - \frac{R n_g}{c} - \frac{L}{c}\left(\frac{1}{\beta_{min}} - n_g\right) \leq t_2 - t_1 \leq \frac{z_2 - z_1}{\beta_{max} c} + \frac{R n_g}{c} + \frac{L}{c}\left(\frac{1}{\beta_{max}} - n_g\right) \quad (5.7)$$

- $|z_2 - z_1| < L$:

$$\frac{z_2 - z_1}{\beta_{min} c} - \frac{R n_g}{c} - \frac{L}{c}\left(\frac{1}{\beta_{min}} - n_g\right) \leq t_2 - t_1 \leq \frac{z_2 - z_1}{\beta_{min} c} + \frac{R n_g}{c} + \frac{L}{c}\left(\frac{1}{\beta_{min}} - n_g\right) \quad (5.8)$$

Thus, dependent on the longitudinal distance between the corresponding storeys, two L1 hits in a cluster are assumed to be correlated if their time difference satisfies the corresponding causality relation given above. Again, an extra time window of 20 ns is taken into account to accommodate calibration uncertainties.

Actually, there exists a small velocity interval below the Cherenkov limit in which the monopoles travel faster than the light. This is due to the fact that the Cherenkov limit is defined by the phase velocity of light $c/n \simeq 0.74\,c$, whereas the effective velocity with which light propagates is the group velocity $c/n_g \simeq 0.72\,c$. When the value of β_{max} lies within this narrow interval, the terms with the factor $(1/\beta_{max} - n_g)$ in the causality relations above are set to zero. It is assumed that the remaining time windows are still valid. The terms with $(1/\beta_{min} - n_g)$ are set to zero when the value of β_{min} lies in the small interval. In addition, the relation in equation 5.1 then reduces to that in equation 1.5.

The expressions in equations 5.6 to 5.8 are generally more stringent than the one in equation 5.1. This is most easily seen for the case that β_{min} equals β_{max}. The causality time window for the directional triggering then depends on the term with Rn_g, which is generally smaller than the term with d/β_{min} in the three-dimensional time window. The only exception is the case in which β_{min} is larger than $1/n_g$ and $z_2 - z_1$ is zero. The numerical values of the two time windows are then the same.

When in any of the directions a sufficient number of causally related L1 hits is found, it is assumed that a monopole signal is present in the data. The data corresponding to this cluster are then stored on disk as a physics event. The ARS data that are directly related to the cluster are referred to as triggered hits. Besides these triggered hits, a physics event also contains all ARS hits that occurred within a certain time window around the time of the cluster. This is done to include all hits that are possibly related to a monopole signal, but did not satisfy the L1 conditions. The time window corresponds to the maximum time that a monopole needs to cross the detector, and is therefore determined by the

minimum velocity $\beta_{min}c$ and the size of the detector.

The monopole trigger will be used to detect monopoles below the Cherenkov limit. Therefore, the value of β_{max} is 0.74. The value of β_{min} is determined by the lowest velocity at which monopoles can produce detectable light, and is therefore chosen to be 0.50.

An estimate of the distance L can be derived from the propagation of the δ-ray light in the sea water. The intensity I of δ-ray light emitted parallel to the path of the monopole decreases with L as (see section 4.5)

$$I \propto \frac{1}{L^2} e^{-L/\lambda_{abs}} \ , \tag{5.9}$$

with λ_{abs} the absorption length of light in the sea water. The value of L should be chosen such, that the overall time window in equations 5.6 to 5.8 is as small as possible, and the probability to include a hit produced by a photon emitted within a distance L from the PMT is as high as possible. Considering the most intense signals in the chosen velocity range (see figure 4.8), a reasonable value of L is then 24 m.

The set of predefined directions that is used in the third step of the algorithm has been optimised such that the full solid angle is covered with a minimum number of directions. The angular spacing between the directions amounts to about 10 degrees.

The efficiency of the new trigger for monopoles below the Cherenkov limit has been determined as a function of the monopole velocity βc. The cuts that have been used are a minimum cluster size of 5 and a maximum transverse distance of 90 m. The efficiency is defined as in section 5.1 and is 100% for the whole velocity range. This indicates that if a monopole produces the required number of L1 hits on as many different storeys, it is indeed found by the trigger. This is not the case for the muon trigger, as is shown in figure 5.1. A more detailed comparison of the two trigger efficiencies will be given in section 5.4.

5.3 Background suppression

Random background, atmospheric muons and atmospheric neutrinos can produce signals in the detector that mimic a passing monopole. Since these signals are not related to a monopole, they are referred to as background. The monopoles which are to be detected are referred to as signal. In order to reduce the rate with which the monopole trigger finds events due to any background, three constraints are applied in addition to the hit selection described in the previous section.

Two constraints concern the minimum cluster size and maximum transverse distance cuts that are applied in the muon trigger to reduce the rate of random background events (see section 1.5). These cuts have also been implemented in the monopole trigger. The minimum cluster size corresponds to the minimum number of L1 hits that a cluster must contain to qualify as physics event. As will be explained in the next chapter, the reconstruction of events found by the monopole trigger involves a fitting procedure with six free parameters. In order to be able to make a constrained fit, hits from at least seven different positions in the detector are needed. The minimum cluster size in the monopole trigger is therefore set to 7.

The maximum transverse distance (R_{max}) is applied in the trigger algorithm to the transverse distance between L1 hits. When this distance exceeds the maximum, it is assumed that the hits are not correlated. The cut is used because the distances between random background hits that are accidentally found to be correlated are generally much larger than those between signal hits. The value of R_{max} in the muon trigger is 90 m. This value has been derived from the propagation of the direct Cherenkov light that muons emit. However, monopoles below the Cherenkov limit only have δ-ray induced light emission. The intensity of δ-ray light falls off more rapidly with the photon path length than that of direct light. It is therefore expected that the distances between hits related to a monopole are smaller than those between hits related to a muon. Consequently, a smaller value of R_{max} can be used in the monopole trigger.

The efficiency with which the trigger finds monopole events is shown in table 5.1 for different values of R_{max}. The efficiencies are given relative to that for $R_{max} = 90$ m. As can be seen, the value of R_{max} can be reduced considerably without a significant loss of monopole events. A reasonable value of R_{max} is 50 m. The relative efficiency loss for this value is less than 2%, which is considered acceptable.

R_{max} (m)	relative trigger efficiency (%)
90	100
80	99.9
70	99.8
60	99.5
50	98.5
40	95.9
30	90.8
20	73.1

Table 5.1: *The relative efficiencies of the monopole trigger for different values of the maximum transverse distance R_{max}.*

A considerable amount of correlated background light in the detector is caused by atmospheric muons. These muons pass through the detector in downward directions, because they cannot penetrate the Earth. To reduce the sensitivity of the detector to downward moving particles, the PMTs in the detector face downward. At the same time, this increases the detector's sensitivity to upward moving particles. The detection of monopoles described in this thesis is therefore restricted to monopoles coming from the lower hemisphere, which means that they must penetrate the Earth in order to be detected. The conditions under which monopoles can cross the Earth and produce light in the detector were discussed in section 4.4.

The direction of a particle moving through the detector can be expressed in terms of the zenith angle and the azimuth angle. The zenith angle is the angle between the direction of the particle and the vertical. A zenith angle of 0 degrees refers to a direction that points vertically upward, i.e. away from the centre of the Earth. The azimuth angle is the angle between the direction of the particle projected on the horizontal plane and

some reference direction in that plane. The directions of particles originating from the lower hemisphere are then characterised by zenith angles between 0 and 90 degrees. Since the monopole detection is restricted to the lower hemisphere, only upward directions with zenith angles between 0 and 90 degrees are considered in the third step of the trigger. This is the third constraint that is applied to reduce the rate of background events.

An estimate of the rate with which the monopole trigger finds events due to the various kinds of background is given in table 5.2. The event rates due to atmospheric muons and atmospheric neutrinos have been determined using the simulations of the detector response to the corresponding signals as described in section 1.8. The atmospheric muon flux that is used in the simulation is taken from [97]. The used fluxes of atmospheric neutrinos are given in [98] and [99]. The contribution of random background to the event rate has been determined assuming a singles rate of 100 kHz. Only an upper limit on the event rate could be determined for this type of background, because the sample of simulated random background data corresponds to only 32 hours. This is due to the large number of random hits that must be generated ($\sim 10^{13}$).

background type	event rate (Hz)
random	$< 2 \times 10^{-5}$
atmospheric neutrinos	4.6×10^{-5}
atmospheric muons	0.11

Table 5.2: *The rate of events found by the monopole trigger due to the three types of background.*

The total rate of background events is about 0.11 Hz, which is dominated by the contribution of atmospheric muons. With a raw data rate of about 0.6 GByte/s and a typical physics event size of approximately 3 kByte (see chapter 1), the reduction in data rate achieved with the trigger is then a factor of about 2×10^6. This reduction factor is sufficient for data taking. Still, the event rate is about 5 orders of magnitude larger than the expected flux of detectable monopoles in ANTARES, which is less than 10 per year (see chapter 3). A further reduction of the background with a factor of about 10^5 should thus be achieved with the off-line analysis of the triggered events. This will be discussed in the next chapter.

5.4 Signal efficiency and effective area

As a consequence of the hit selection and cuts that are used in the monopole trigger to reduce the background event rate, not all monopoles passing through the detector will be detected. The degree of this signal loss can be represented by the efficiency of the trigger for monopole signals. Here, the efficiency is defined as the ratio of the number of detected monopole events to the number of events which have at least 10 detected photons due to the monopole. The efficiency is shown in figure 5.3a as a function of the monopole velocity βc. The efficiency of the muon trigger for monopoles is also shown in the figure. Only upward going monopoles have been considered. Furthermore, only signal

hits† have been taken into account. This differs from the actual situation, in which signal hits are accompanied by hits due to the random background. Accidental coincidences of these background hits with signal hits may cause monopole signals to meet the trigger requirements more often. Taking into account random background hits therefore generally results in slightly higher efficiencies than those shown in figure 5.3a.

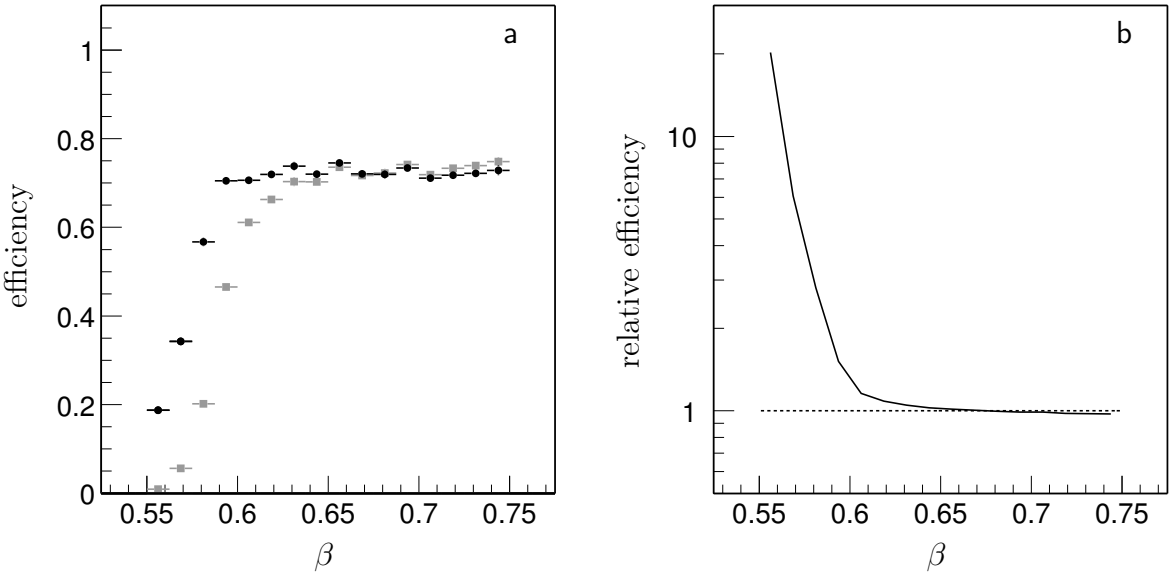

Figure 5.3: *a: The efficiencies of the monopole trigger (black dots) and the muon trigger (grey squares) for upward going monopoles as a function of the monopole velocity. The efficiency is defined as the ratio of the number of detected monopole events to the number of events with at least 10 detected signal photons. b: The efficiency of the monopole trigger (black line) relative to that of the muon trigger (dashed line).*

The efficiency of the monopole trigger shows a velocity threshold at about $0.60\,c$. Above this threshold, the efficiency is approximately constant and amounts to about 70%. Below the threshold, the efficiency decreases with decreasing velocity to about 20% at $0.55\,c$. Monopoles with these velocities have a relatively small light yield. Consequently, they produce relatively few hits that either have a large charge or form a local coincidence (L1 hits). The number of L1 hits that these monopoles produce is therefore more often below the threshold of the minimum cluster size than for faster monopoles.

Monopoles with larger velocities are more efficient in producing a sufficient number of L1 hits because the light yield increases with increasing velocity (see figure 4.5). However, above about $0.60\,c$ the efficiency of the trigger does not increase further. This is caused by monopoles that are relatively far away from the detector. Due to their large light yield, these monopoles can still have enough detected photons to be considered in the normalisation of the efficiency. The intensity of the light that still reaches the detector can however be such, that the produced hits do not satisfy the L1 conditions.

†Here, a hit is defined as an ARS hit, i.e. the digital information on the time and charge of a PMT signal as produced by the read-out electronics, see section 1.3.

The efficiency of the monopole trigger relative to that of the muon trigger is shown in figure 5.3b. The figure shows that below monopole velocities of about $0.60\,c$, the monopole trigger is a factor between about 2 and 20 more efficient than the muon trigger, depending on the velocity. Above about $0.60\,c$ the efficiencies of the two triggers are approximately the same. It can be expected that the monopole trigger should be somewhat more efficient in this velocity range. However, the value of the minimum cluster size that is used in the monopole trigger is 7, as opposed to 5 in the muon trigger. This results in a small decrease of the monopole trigger efficiency. The great advantage of the monopole trigger for these velocities is its background event rate, which is a factor of about 50 less than that of the muon trigger.

The sensitivity of the detector to a flux of through-going monopoles can be represented by a so-called effective area. The effective area is defined as the ratio of the rate of detected monopole events R to the monopole flux F,

$$A_{\mathit{eff}}\,(\beta,\theta,\phi) = \frac{R\,(\beta,\theta,\phi)}{F\,(\beta,\theta,\phi)}\ , \tag{5.10}$$

where all three quantities can be expressed as a function of the monopole velocity βc and the monopole direction (θ,ϕ), where θ and ϕ are the zenith and azimuth angle respectively. The effective area of the ANTARES detector for upward going monopoles that are detected by the monopole trigger is shown in figure 5.4 as a function of the monopole velocity. The effective area has been averaged over all upward directions. The geometrical area of the detector averaged over all upward directions is also shown in the figure. This area has been derived from the smallest cylindrical volume that contains the instrumented detector volume.

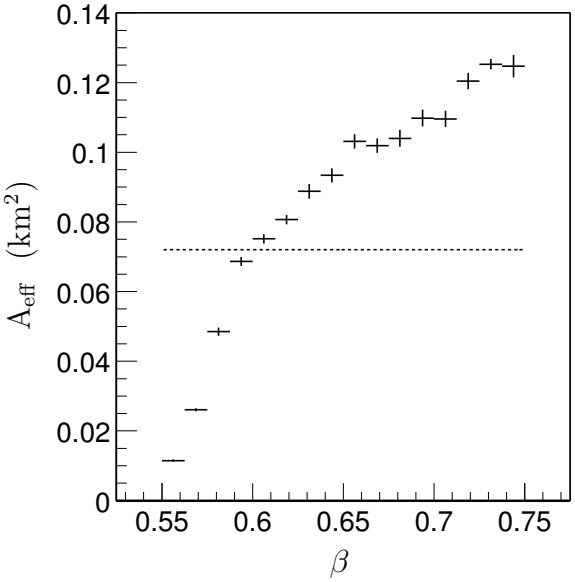

Figure 5.4: *The average effective area A_{eff} of the detector for up-going monopoles using the monopole trigger. The average geometrical area of the detector is indicated by the dashed line.*

The effective area is about 0.01 km^2 for monopoles with velocities of about $0.55\,c$, and increases to about 0.13 km^2 for monopole velocities of about $0.74\,c$. Above about

$0.60\,c$, the effective area exceeds the geometrical area of the detector. At these velocities, monopoles that pass the detector at some distance outside the instrumented volume can be detected by the trigger, and hence contribute to the effective area.

5.5 Speed, hit efficiency and hit purity

The monopole trigger will be used to process the raw data coming from the detector in real time. To achieve this, it will be running on multiple processors. The number of required processors is determined by the speed of the trigger algorithm. For a singles rate of 100 kHz, the speed of the monopole trigger is about the same as that of the muon trigger. This implies, that about 10 processors of 2.2 GHz are needed to process the data in real time with the monopole trigger.

Besides the data rate reduction, signal efficiency and speed, the quality of the monopole trigger is also related to the efficiency and purity of the hit selection that is used in the trigger. The hit efficiency is defined as the ratio of the number of signal hits in a monopole event that are selected by the trigger to the total number of signal hits in that event. The average hit efficiency for monopole events with less than 100 signal hits is shown in figure 5.5a as a function of the monopole velocity. Only events that were found by the trigger have been considered. The hit efficiency is about 80% at $0.55\,c$, and decreases to approximately 50% at $0.74\,c$. The decrease is mainly related to the more intense light emission of faster monopoles, due to which these monopoles produce a greater fraction of the hits at large (transverse) distances. The intensity of the light at large distances is more often such, that the produced hits do not satisfy the L1 requirements. Furthermore, hits that occur at large (transverse) distances are more likely to be rejected by the maximum transverse distance cut.

As is explained in the previous section, in reality the signal hits are accompanied by hits caused by random background. Due to accidental coincidences with signal hits, these background hits may be selected by the trigger and contribute to the cluster of triggered hits. The degree to which this happens can be quantified by the hit purity, which is given by the ratio of the number of triggered hits that is caused by a monopole to the total number of triggered hits. The average hit purity for a singles rate of 100 kHz is shown in figure 5.5b as a function of the monopole velocity. Only events with less than 100 signal hits that were found by the trigger have been considered. The hit purity is more than 95% for the whole velocity range. Both the hit efficiency and hit purity increase when events with more than 100 signal hits are considered.

5.6 Discussion

The background event rate of the monopole trigger could be reduced further by choosing a smaller velocity interval for which the trigger is sensitive. In order to still be sensitive to all velocities below the Cherenkov limit, several trigger algorithms could run simultaneously, each one searching for monopoles in a small velocity interval. A first study shows however, that only a slight reduction of the background event rate can be accomplished in this way.

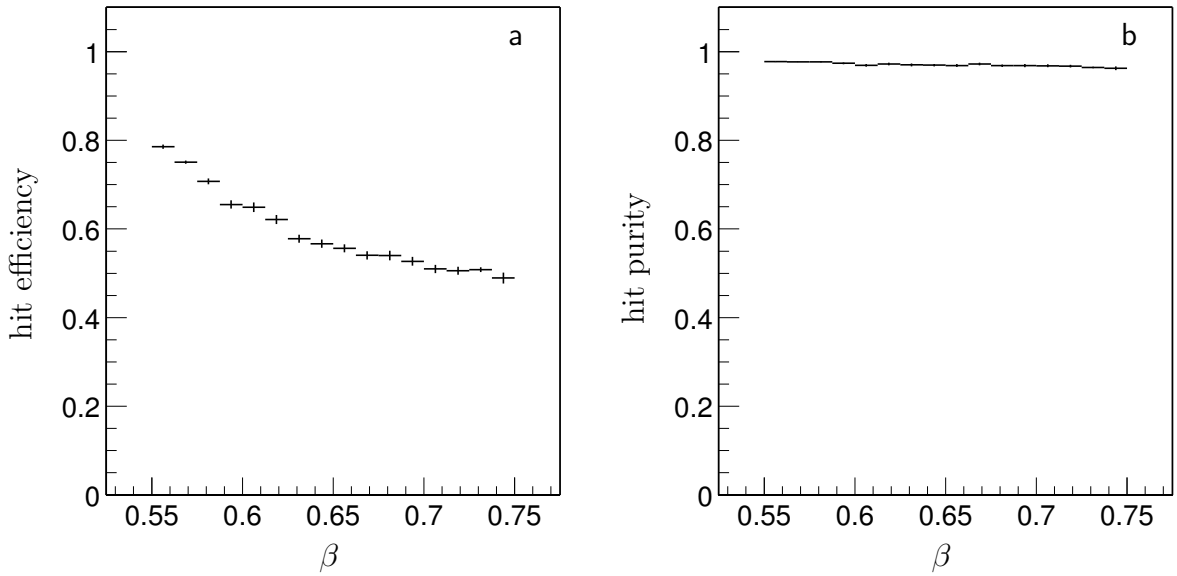

Figure 5.5: *The average hit efficiency (a) and hit purity (b) of the monopole trigger for events with less than 100 signal hits in the detector.*

This indicates that the possibility to discriminate between particle velocities on the basis of the trigger algorithm is limited.

The off-line analysis of events found by the monopole trigger will be presented in the next chapter. The effective area of the ANTARES detector obtained with the monopole trigger will be affected by this analysis.

Monopoles with velocities above the Cherenkov limit are likely to be found by the muon trigger. These monopoles are characterised by the very intense direct Cherenkov light emission. The reconstruction and analysis of these bright monopole signals have been studied within ANTARES [12] and by the BAIKAL and AMANDA neutrino telescope experiments [85, 86]. These have set an upper limit on the flux of these fast monopoles (see section 3.6.4). In the event analysis described in the next chapter, monopoles with velocities above the Cherenkov limit will not be considered.

Chapter 6

Analysis and results

In the preceding chapter, a trigger algorithm has been developed that searches for signals of magnetic monopoles in the raw data coming from the detector. When the trigger algorithm indicates the presence of a set of hits that are possibly related to a monopole signal, the corresponding data are written to disk. These data are referred to as an event. Most of these events are caused by background light produced by atmospheric muons or atmospheric neutrinos. Considering present limits on the cosmic monopole flux, only a very small fraction of the events might be caused by magnetic monopoles. In order to distinguish between signal and background, the events are analysed further. This is done off-line using a dedicated software program. The data in each event are tested against different hypotheses. In this way, the compatibility of the observed data with a monopole signal can be determined and a discovery potential for monopoles can be quantified.

6.1 Analysis

The major part of the events found by the monopole trigger is due to background signals produced by atmospheric muons. A small contribution is due to muons produced by interactions of atmospheric neutrinos. In order to detect a magnetic monopole, it has to be decided whether an event has been caused by a muon or by a monopole passing through the detector*. For this purpose, the time and position information of the triggered hits in the event are used to calculate the probability that the event was produced by a muon (hypothesis H_0) and that the event was caused by a monopole (hypothesis H_1). The triggered hits of an event are the hits that were found to be causally related by the trigger algorithm.

The trajectory of a particle that passes through the detector can be described by five independent parameters when it is assumed that the velocity of the particle is known. The direction of the track can be expressed in terms of the zenith and the azimuth angle (θ,ϕ). The position of the track is commonly expressed in terms of the position at the minimum distance of approach between the track and the centre of the detector. This position can be described by two orthogonal co-ordinates (x_0,y_0) which are both transverse to the track direction. This nomenclature corresponds to a system in which the particle moves along

*The contribution of random background to the event rate is not considered here, see section 6.6.

the z-axis. The fifth track parameter is the time t_0 that the particle passes this position.

The algorithm that is used to calculate the probability of the event for a certain particle hypothesis consists of two consecutive fitting procedures: the linear prefit and the maximum likelihood fit. These procedures estimate the particle's track parameters from the data by maximisation of the probability of the event for a given hypothesis.

The linear prefit provides a first estimate of the time and position of the track for a predefined direction. It is a least squares fit through the positions of the PMTs on which the hits in the event occurred, with the hit times as independent measurements. Assuming that the errors on the hit times and positions are uncorrelated, the track parameters can be estimated by minimising the χ^2 given by

$$\chi^2 = \sum_j \frac{(t_j - t_j^{exp})^2}{\sigma_j^2} \ , \tag{6.1}$$

where t_j is the measured time of hit j, t_j^{exp} is the expected hit time for the given track parameters, and σ_j is the uncertainty on the measured hit time. As will be discussed below, a linear relation between the hit times and the track parameters can be obtained, in which case the track parameters can be found analytically.

The predefined direction and the estimated track time and position from the prefit define a track that is used as starting point in the second fitting procedure. This fit is applied to improve the results from the prefit. It makes use of the method of maximum likelihood. For a given hypothesis and a given set of track parameters, the probability to observe the measured data can be calculated. This probability is commonly referred to as the likelihood. The assumed hypothesis is reflected by probability density functions (PDFs), which describe the expected distributions of the measured quantities. The track parameters that are found correspond to those for which the likelihood is maximal. If the PDFs and the hypothesis are correct, a high probability for the measured data is then expected.

In the maximum likelihood fit two quantities are considered. The first quantity is the angle θ at which the photons that caused a hit were emitted with respect to the direction of the track. The second quantity is the distance r that these photons travelled through the sea water before being detected. Using the values of the track parameters, both quantities can be determined from the hit time and position. They are then used to calculate the probability that a certain hit occurred at that angle and distance. It is assumed that the dependence of this probability on the two quantities can be factorised. The expected distributions of the angle and the distance can then be described by separate PDFs, denoted as $P(\cos\theta)$ and $P(r)$ respectively. In the case of independent measurements, the likelihood L of an event can be expressed as the product of the individual hit probabilities,

$$L = \prod_j P(\cos\theta_j) \times P(r_j) \ , \tag{6.2}$$

where θ_j is the photon emission angle and r_j is the photon path length for hit j. The maximisation of this likelihood function is done iteratively using standard numerical tools [100]. All five track parameters are left free in the fit. In the case of the monopole hypothesis, this fit is repeated for different presumed values of the monopole velocity.

Like in the trigger algorithm, a loop over a set of predefined directions is implemented in the analysis program. For each event, both fitting procedures are applied for each direction. The purpose of the loop is twofold. Firstly, the given direction is used in the linear prefit. Secondly, the likelihood function may have more than one maximum, in which case a general maximisation algorithm can converge to a local maximum instead of the global maximum. The number of predefined directions is chosen such that the (angular) distance to the global maximum is sufficiently small and the performance of the algorithm is not compromised. The resulting number of directions is typically 200, which corresponds to an average spacing of about 10 degrees.

6.1.1 Muon hypothesis

A muon that passes through the detector is characterised by a straight track, along which it moves with the speed of light c. On its way, the muon emits Cherenkov light at the typical Cherenkov angle $\cos\theta_c = 1/n$ with respect to its direction, with n the phase refractive index of the sea water. For a muon that travels in the z-direction, the expected arrival time t^{exp} of a Cherenkov photon on a certain PMT at position (x,y,z) in the detector can be given by (see section 1.5)

$$t^{exp} = t_0 + \frac{z - z_0}{c} + \frac{R}{c}\tan\theta_c \ . \tag{6.3}$$

Here $z - z_0$ is the difference between the z-positions of the PMT and the muon at time t_0, and R is the transverse distance between the PMT and the muon path, given by $R = \sqrt{(x - x_0)^2 + (y - y_0)^2}$. In this expression the approximation $n = n_g$ is used, with $n_g = 1.38$ the group refractive index of the sea water.

The prefit first averages the hit positions to determine an initial estimate of the position (x_0,y_0,z_0) of the muon track. This position is then used to obtain a first estimate of the track time t_0. A linear relation between the hit times and the z co-ordinates of the hits is obtained when the transverse distances of the hits are small. Therefore, the measured hit times are corrected for the transverse distance, $t_j - \frac{R_j}{c}\tan\theta_c$. Minimisation of the χ^2 given in equation 6.1 then yields the following expression for t_0,

$$t_0 = \frac{1}{N}\sum_{j=1}^{N}\left(t_j - \frac{R_j}{c}\tan\theta_c - \frac{z_j - z_0}{c}\right) \ , \tag{6.4}$$

with N the total number of hits in the event. It is assumed here that the uncertainty σ_j on the hit time is the same for each measurement. The transverse positions of the hits are then averaged again using the corrected hit times $t_j - t_0 - \frac{z_j - z_0}{c}$ as the inverse weight to obtain an improved estimate of the transverse position (x_0,y_0) of the track. This corrected hit time is proportional to the transverse distance R_j of a hit, as follows from equation 6.3. The improved position is used to determine a second and final estimate of t_0 in the prefit.

For given track parameters, the emission angle of the photons that caused a hit can be calculated from the hit time and position as (see equation 6.3)

$$\tan\theta_j = \frac{c}{R_j}\left(t_j - t_0 - \frac{z_j - z_0}{c}\right) \ . \tag{6.5}$$

When the track parameters are close to the true values, this angle is expected to equal the Cherenkov angle. However, due to for instance scattering of the photons in the sea water, the distribution of the arrival times of the photons shows a finite spread. This results in a spread of the measured distribution of the angle θ. This distribution can be approximated by a Gaussian PDF centred at the value of the Cherenkov angle,

$$P(\cos\theta) = \frac{1}{\sigma_\theta\sqrt{2\pi}} e^{-(\cos\theta - \cos\theta_c)^2/2\sigma_\theta^2} \ . \tag{6.6}$$

This is the angular PDF that is used in the maximum likelihood fit for the muon hypothesis. The spread σ_θ in $\cos\theta$ around the Cherenkov angle is estimated from Monte Carlo simulations of atmospheric muons. It corresponds to a spread in θ of about 6 degrees. A small fraction of the triggered hits in an event may be due to random background (see section 5.5). Considering the purity of the triggered hits shown in figure 5.5b, a fraction of 5% of random background hits is accounted for in the PDF[†]. This is done by adding a constant baseline, since a flat distribution of $\cos\theta$ is expected for these hits. The PDF including background is normalised such that $\int_{-1}^{1} P(\cos\theta) d\cos\theta = 1$. The result is shown in figure 6.1a.

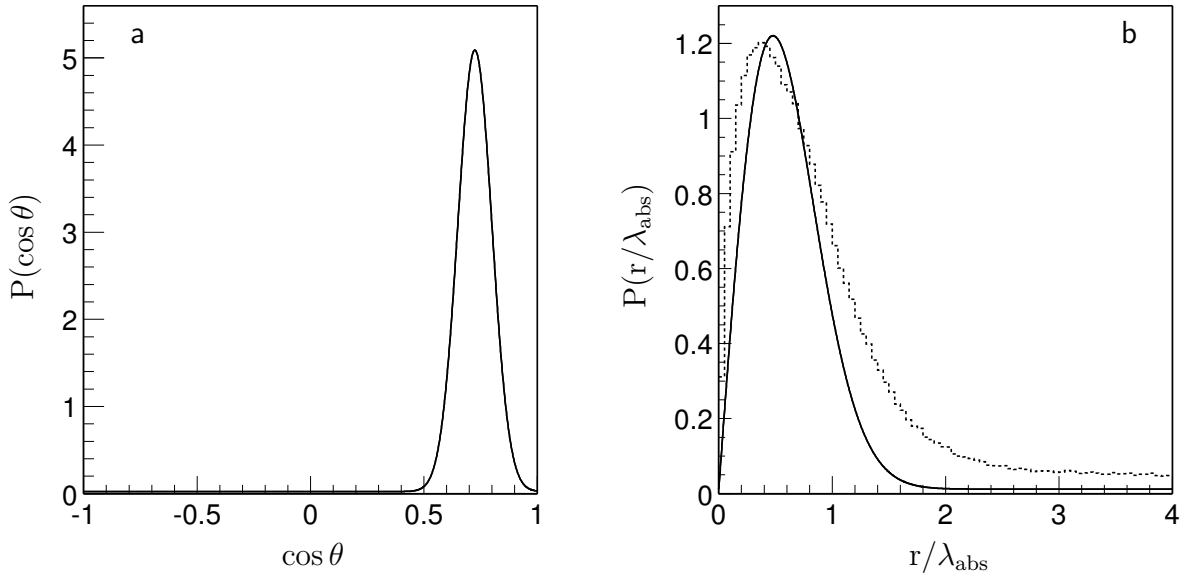

Figure 6.1: *a: The angular PDF $P(\cos\theta)$ for the muon hypothesis. b: The distance PDF $P(r)$ for the muon hypothesis (solid line). Also shown is the distribution of r obtained from Monte Carlo simulations of atmospheric muons (dashed line).*

The path length of the photons can be calculated once their emission angle is known,

$$r_j = \frac{R_j}{\sin\theta_j} \ . \tag{6.7}$$

[†]The hit purity shown in figure 5.5b has been determined with simulated monopole events. It is assumed that the same purity is valid for events caused by muons.

The probability $P(r)$ that the light indeed caused a hit after travelling the distance r can be expressed as the product of the probability to encounter a PMT at this distance, and the probability that a PMT records a hit given the light intensity at this distance. When a constant density of PMTs is assumed and when the particle track is within the instrumented detector volume, the probability to find a PMT at r is proportional to the corresponding transverse distance R. In general, the light intensity is such that the probability $P(n_\gamma)$ that a PMT detects a number of photons n_γ is Poisson distributed. By definition, a hit is recorded when the PMT detects one or more photons. The corresponding probability can thus be written as

$$\begin{aligned} P(n_\gamma \geq 1) &= 1 - P(n_\gamma = 0) \\ &= 1 - e^{-\mu} \ , \end{aligned} \tag{6.8}$$

where the expectation value μ is proportional to the light intensity, the PMT's quantum efficiency QE and the PMT's effective photo-cathode area A, which depends on the photon's angle of incidence. Averaging over the orientations of the PMTs, and taking into account the attenuation of the direct Cherenkov light in the sea water, μ can be expressed as

$$\mu \propto \frac{I_0}{r} e^{-r/\lambda_{abs}} \times QE \times A \ , \tag{6.9}$$

where I_0 is the number of Cherenkov photons that is emitted per unit path length of the muon, and λ_{abs} is the absorption length. $P(n_\gamma \geq 1)$ can then be estimated using the numerical values of the quantities in equation 6.9 (see chapter 1). Deviations of r due to the spread in θ are neglected. $P(n_\gamma \geq 1)$ is 1 for r significantly less than λ_{abs}, and decreases to 0 at large r. This dependence can be approximated by a Gaussian function centred at $r = 0$. The standard deviation σ_r of this function corresponds to the distance where $\mu = 0.5$. This distance amounts to about 30 m.

The distance PDF $P(r)$ that is used in the maximum likelihood fit is then given by

$$P(r) = \frac{r}{\sigma_r^2} e^{-r^2/2\sigma_r^2} \ , \tag{6.10}$$

where the substitution $R = r \sin\theta$ is used. Again, an impurity of 5% is incorporated in the PDF as a flat distribution. The PDF including background is normalised to 1. The result is shown in figure 6.1b as a function of the photon path length in units of λ_{abs}. As can be seen from the figure, the PDF agrees rather well with Monte Carlo simulations of atmospheric muons for values of r less than about one absorption length.

6.1.2 Monopole hypothesis

The magnetic monopoles of interest are characterised by a velocity $\beta c < c/n$ and a relatively broad angular distribution of the light emission, see figure 4.8. For a monopole that travels in the z-direction, the expected arrival time of a photon on a PMT can be given by (see section 5.2)

$$t^{exp} = t_0 + \frac{z - z_0}{\beta c} + \frac{R}{c} \left(\frac{\beta n_g - \cos\theta}{\beta \sin\theta} \right) \ , \tag{6.11}$$

where θ is the emission angle of the light with respect to the monopole direction.

In the prefit, a first estimate of the track position is determined from the average of the hit positions. Since the monopole velocity is unknown, it is a free parameter in the fit. An initial estimate of the velocity is obtained from the difference between the times and positions of the earliest and latest hit in the event. The measured hit times cannot be corrected for the transverse distance of the hits, because the emission angle of the photons is not fixed. Assuming small values of the transverse distances, the position and velocity estimates can be used to correct the measured hit times for the monopole propagation time, $t_j - \frac{z_j - z_0}{\beta c}$. The corrected times are then averaged to obtain a first estimate of t_0. The estimate of the transverse position of the track is then improved by averaging the transverse positions of the hits with the times $t_j - t_0 - \frac{z_j - z_0}{\beta c}$ as inverse weight. Final estimates of the velocity and t_0 follow from the minimisation of the χ^2 (see equation 6.1),

$$\frac{1}{\beta c} = \frac{\langle t_j(z_j - z_0)\rangle - \langle t_j\rangle\langle(z_j - z_0)\rangle}{\langle(z_j - z_0)^2\rangle - \langle(z_j - z_0)\rangle^2} \tag{6.12}$$

$$t_0 = \langle t_j\rangle - \frac{\langle(z_j - z_0)\rangle}{\beta c} \ , \tag{6.13}$$

assuming that σ_j is the same for each measurement. In this, the triangular brackets indicate the sample average.

The monopole velocity is also a free parameter in the maximum likelihood fit. Because the intensity and the angular distribution of the light emitted by monopoles depend on the monopole velocity (see figures 4.8 and 4.5), this is achieved by repeating the fit for five different presumed velocities. For each velocity, a unique angular and distance PDF are used. The five velocities correspond to $\beta = 0.55$, 0.60, 0.65, 0.70, 0.75. The angular distributions of the light emission that have been derived in section 4.3 are used as the angular PDFs $P(\cos\theta)$. The PDFs including 5% background are normalised to 1. The results are shown in figure 6.2.

The photon emission angle for a certain hit and given track parameters can be derived from equation 6.11. For $\beta < 1/n_g$ only one physical solution exists. It is given by

$$\cos\theta_j = \frac{b_j - a_j\sqrt{a_j^2 - b_j^2 + 1}}{a_j^2 + 1} \tag{6.14}$$

where

$$a_j = \frac{\beta c}{R_j}\left(t_j - t_0 - \frac{z_j - z_0}{\beta c}\right) \tag{6.15}$$

$$b_j = \beta n_g \ . \tag{6.16}$$

This expression is also used when $1/n_g < \beta < 1/n$.

The functional form of the distance PDFs $P(r)$ used for the monopole hypothesis is given by equation 6.10. The standard deviations σ_r of these PDFs can again be derived from the point where $\mu = 0.5$. Taking into account the attenuation of δ-ray induced light in the sea water, μ can be expressed as

$$\mu \propto \frac{I_0}{r^2} e^{-r/\lambda_{abs}} \times QE \times A \ , \tag{6.17}$$

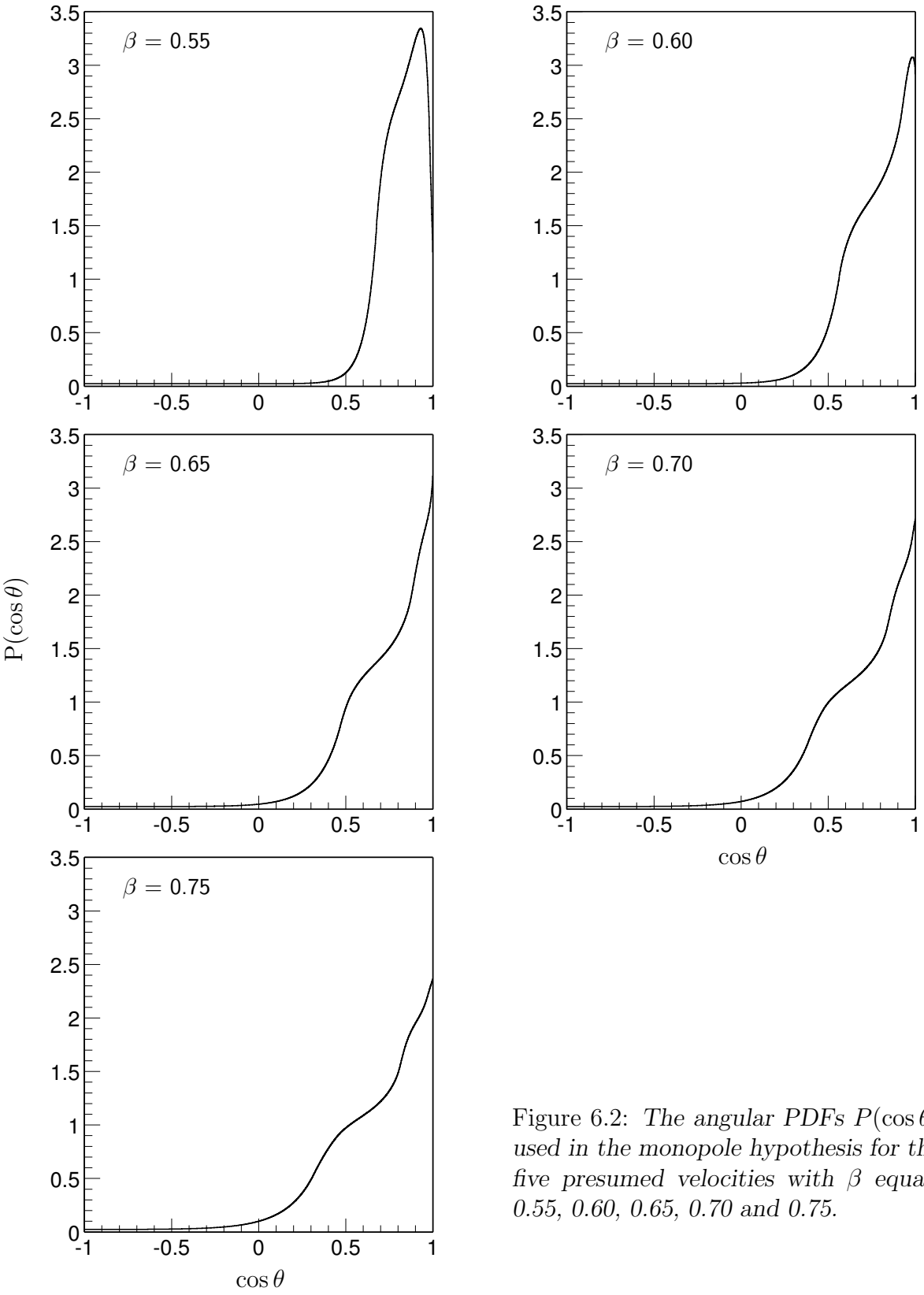

Figure 6.2: *The angular PDFs $P(\cos\theta)$ used in the monopole hypothesis for the five presumed velocities with β equals 0.55, 0.60, 0.65, 0.70 and 0.75.*

where the light yield I_0 on the monopole track depends on the monopole velocity, see figure 4.5. However, substitution of I_0 into this equation generally leads to too small values of σ_r. This is because an appropriate angular integration over the emission angle is necessary to determine the light intensity at distance r. This has been done in the Monte Carlo simulation of monopole signals, which is described in section 4.5. The σ_r are therefore estimated from simulations of magnetic monopoles with the corresponding velocities. They are given in table 6.1. Again the PDFs account for 5% impurity, and are normalised to 1.

β	σ_r (m)
0.55	17
0.60	25
0.65	32
0.70	38
0.75	40

Table 6.1: *The standard deviation σ_r of the distance PDF $P(r)$ for the five presumed velocities of the monopole hypothesis.*

6.2 Likelihood ratio

In the analysis of an event, the likelihood function is maximised for each predefined direction in the set. This generally results in several likelihood values for each hypothesis due to local maxima in the likelihood functions. For the muon hypothesis, the global maximum is assumed to be the final likelihood value. As is discussed in section 5.3, the work described in this thesis is restricted to monopoles with upward directions, i.e. directions with a zenith angle between 0 and 90 degrees. The maximum likelihood for the monopole hypothesis is therefore selected from the values that correspond to an upward fitted direction. In this, the results for all five presumed monopole velocities are considered. The likelihood fit for the monopole hypothesis thus has six free parameters. In order to make a constrained fit, at least seven different positions in the detector are then needed. The analysis is therefore applied to all events that are found by the monopole trigger which have hits on at least seven different storeys.

A quantity Λ is defined that is a measure for the compatibility of the observed data with a monopole signal. The quantity is given by the logarithm of the ratio of the maximum likelihood for the monopole hypothesis L_1 to the maximum likelihood for the muon hypothesis L_0,

$$\begin{aligned} \Lambda &= \ln \frac{L_1}{L_0} \\ &= \ln L_1 - \ln L_0 \ . \end{aligned} \tag{6.18}$$

For events that are caused by a monopole, Λ is expected to yield positive values. For events caused by atmospheric muons or atmospheric neutrinos, the value of Λ is expected

to be negative. Since no hit selection is performed in the analysis, the fitting procedures of both hypotheses take all hits in an event into account. In the following, the value of Λ is normalised to the number of hits in the event.

The distribution of Λ is shown in figure 6.3 for monopoles with $0.55 \leq \beta < 0.74$ and for the two dominant contributions to the background. For this, simulated events have been used with a contribution of random background that corresponds to a singles rate of 100 kHz. The integral of each distribution corresponds to the number of events that would be found during one year of data taking. For this, the events caused by atmospheric muons and atmospheric neutrinos have been weighted with the corresponding fluxes given in section 5.3. The number of atmospheric muon and atmospheric neutrino events are 2.8×10^6 and 1.4×10^3 per year, respectively. The monopole events have been weighted with a flux that corresponds to 10 monopoles that cross the geometrical area of the detector per year and are distributed uniformly over all upward directions and all β in the range between 0.55 and 0.74. As expected, the value of Λ is positive for most signal events, and negative for most background events. A small fraction of the monopole events has a negative value of Λ. Some background events have a positive Λ value.

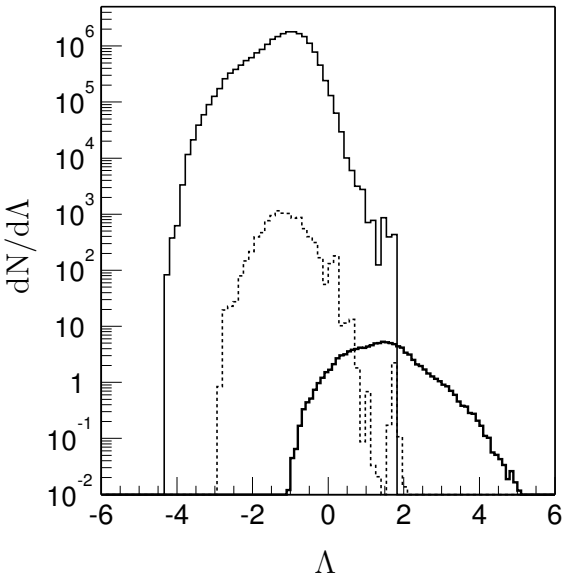

Figure 6.3: *The distribution of the likelihood ratio Λ for simulated events caused by magnetic monopoles (thick solid line), atmospheric muons (solid line) and atmospheric neutrinos (dashed line). The number of events in each distribution corresponds to one year of data taking.*

In order to find an event that was caused by a monopole, background events need to be separated from signal events. The value of Λ can be used to distinguish between signal and background. By construction, events for which Λ has a negative value can directly be considered as background. In this way, about 99% of the atmospheric muon events and 96% of the atmospheric neutrino events can be rejected. The fraction of signal events that is lost by applying this cut amounts to about 5%. However, to find a signal event unambiguously, the background that remains at positive values of Λ needs to be reduced further. This is done by introducing a final cut that is applied to all events that are analysed. This cut is based on the value of Λ.

6.3 Background rejection

The final event selection is defined by a final cut value of the likelihood ratio, Λ_c, that is applied to the data. The value of Λ_c is determined from the distribution of Λ for both types of background events taken together. Ideally, this critical value should be chosen such that the probability that a background event is mistaken for a signal event after the final cut is less than 2.7×10^{-3} or 5.7×10^{-7}. These probabilities correspond to, respectively, the 3σ and 5σ confidence levels of the likelihood ratio test. Only events for which Λ exceeds the critical value will then be accepted as signal events. The events found can then be interpreted as a discovery of a magnetic monopole with a 3σ or 5σ significance.

Due to the limited number of simulated background events, it is not possible to determine the values of Λ_c that correspond to the 3σ and 5σ levels from the background distribution directly. Therefore, an exponential function is fitted to the distribution. This function is then extrapolated to obtain estimates of the values of Λ_c. The fitted function is shown in figure 6.4a together with the simulated data. The fit yields a χ^2 value of 1.2 per degree of freedom, which indicates that the distribution is fitted rather well. Extrapolation of the function then yields Λ_c values of 3.38 and 5.14 for the 3σ and 5σ levels respectively.

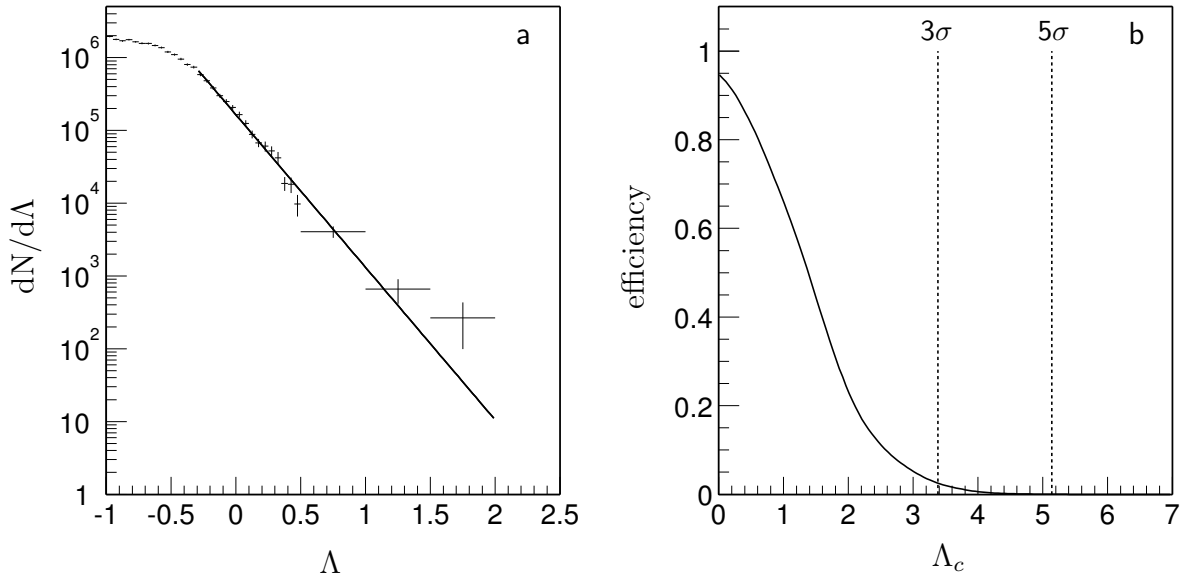

Figure 6.4: *a: The function that is fitted to the Λ distribution of all background to extrapolate to the 3σ and 5σ confidence levels. b: The efficiency with which signal events are selected as a function of the cut value Λ_c.*

Application of the final cut leads to a considerable loss of signal events. The fraction of analysed signal events that is accepted as a function of the cut value is shown in figure 6.4b. The values of the cut for the 3σ and 5σ levels are also shown in the figure. The signal efficiency is about 95% for $\Lambda_c = 0$, and decreases to about 3% for the cut at the 3σ

level. For the 5σ cut, essentially no signal is left. This indicates that a discovery on the basis of a single event is not feasible with the analysis presented here. Furthermore, to estimate the values of the cut at the two confidence levels, the fitted function needs to be extrapolated significantly beyond the Λ distribution obtained with simulated background events. The validity of describing the distribution with the exponential function in this region is questionable. Therefore, a different approach is used. The value of the cut is chosen close to the region with significant statistics. The fitted function can then be considered as a reliable description of the tail of the Λ distribution. However, in this case the number of background events that survive the final cut increases. Consequently, a discovery can then be made only on the basis of several events per year. The value of Λ_c is then chosen such, that the number of events needed for a 5σ discovery is as small as possible, and the efficiency for signal events is as large as possible. The optimal value of Λ_c thus obtained is 2.35. The expected number of background events that remain after this cut is about 0.4 per year.

6.4 Signal efficiency and effective area

The efficiency with which monopole events are accepted as a function of the cut value is shown in figure 6.5 for monopoles with different velocities. The value of the final cut has been set to $\Lambda_c = 2.35$ and is also shown in the figure. For monopoles with velocities above about $0.68\,c$, the final efficiency is less than 1%. The efficiency increases with decreasing velocity to about 60% for monopoles with $0.55 \leq \beta < 0.58$. As can be seen from figure 6.4b, the average efficiency for monopole velocities between $0.55\,c$ and $0.74\,c$ is about 15%. For the assumed monopole flux (see section 6.2), this corresponds to about 1.5 monopole events that can be found per year. Monopoles with $\beta > 0.68$ do not contribute to this, since the efficiency for these velocities is practically zero. Although the efficiency for monopoles with $0.55 \leq \beta < 0.58$ is the highest for all velocity ranges in figure 6.5, only a small fraction of the found events corresponds to these monopoles. This is due to the small effective area of the detector for these monopoles, as will be shown below.

The sensitivity of the ANTARES neutrino telescope to a flux of through-going monopoles can be expressed in terms of an effective area A_{eff}. This area is defined as the ratio of the rate of detected monopole events to the monopole flux (see equation 5.10). The effective area of the detector for upward moving monopoles with velocities between $0.55\,c$ and $0.74\,c$ is shown in figure 6.6 as a function of the monopole velocity. The effective area is averaged over all upward directions. Only velocities below $0.68\,c$ have been considered. The area shown represents the sensitivity for the case that the monopole trigger (see chapter 5) and the event analysis with the final cut presented in this chapter are applied. The effective area is about 5×10^3 m^2 for monopoles with velocities of about $0.55\,c$, and increases to approximately 2.8×10^4 m^2 for monopole velocities of about $0.60\,c$. Above this velocity, the effective area decreases again to about 6×10^3 m^2 at $0.67\,c$. Generally, the effective area is expected to increase with the monopole velocity due to the increasing light yield of the monopoles. This can be seen in figure 5.4, which shows the effective area when only the monopole trigger is applied. However, the inefficiency that is introduced by applying the final cut increases with increasing monopole velocity. This is due to the

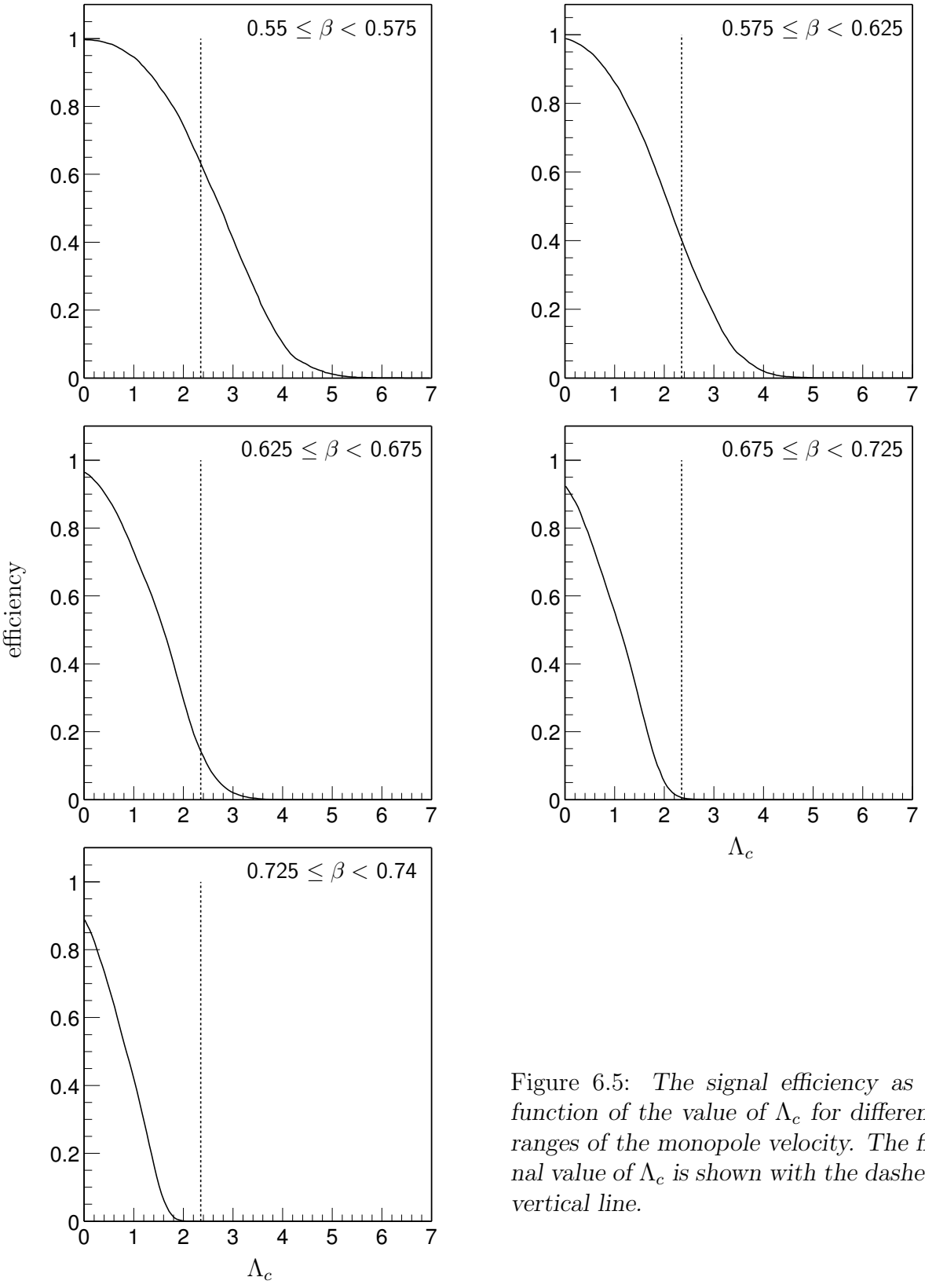

Figure 6.5: *The signal efficiency as a function of the value of Λ_c for different ranges of the monopole velocity. The final value of Λ_c is shown with the dashed vertical line.*

effect of the read-out electronics, which has not been taken into account in the PDFs for the maximum likelihood fits. The agreement between the PDFs and the distributions of the triggered hits becomes worse as the velocity increases.

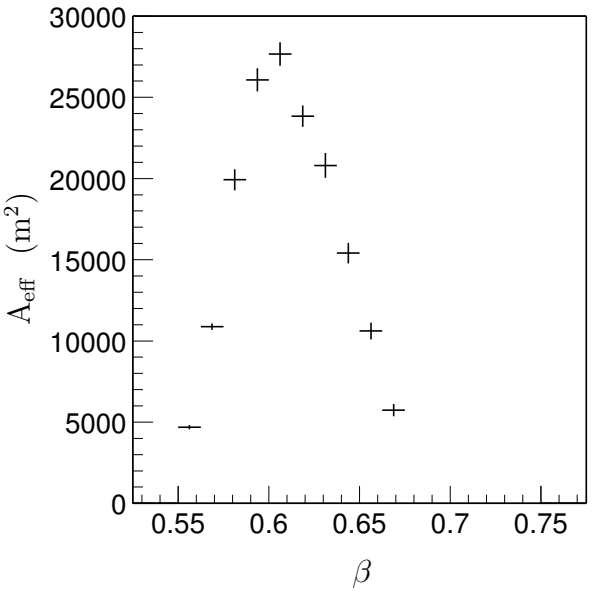

Figure 6.6: *The average effective area A_{eff} of the ANTARES detector for up-going monopoles with velocities βc using the monopole trigger and the event analysis developed in this work.*

6.5 Discovery potential

The value of the final cut Λ_c is chosen such, that the expected number of background events that remain is about 0.4 per year. A discovery can then be made when several events are found for which the value of Λ exceeds Λ_c. The minimum number of events that is needed for a discovery with a 3σ (5σ) significance level corresponds to that number for which the probability that it is due to background only is less than 2.7×10^{-3} (5.7×10^{-7}). For an expected background of 0.4 events per year, the required minimum number of events is then 4 (7) per year.

The probability of discovering a monopole at the 3σ (5σ) level with one year of data taking is given by the probability that a given flux produces at least 4 (7) events that survive the final cut. The flux needed for a discovery can be calculated with the effective area of the detector averaged over all velocities in the range between $0.55\,c$ and $0.74\,c$. As a measure for the discovery potential, the calculated monopole flux has a 50% probability to produce a sufficient number of events. The result is shown in figure 6.7 for both significance levels. It is assumed that the monopoles have a uniform distribution for all upward directions and for all velocities between $0.55\,c$ and $0.74\,c$. For the 3σ (5σ) significance level, the required flux is a factor of about 6 (3) below the Parker limit on the average monopole flux (see chapter 3). This limit is approximately 10^{-15} cm^{-2}sr^{-1}s^{-1} and is also shown in figure 6.7.

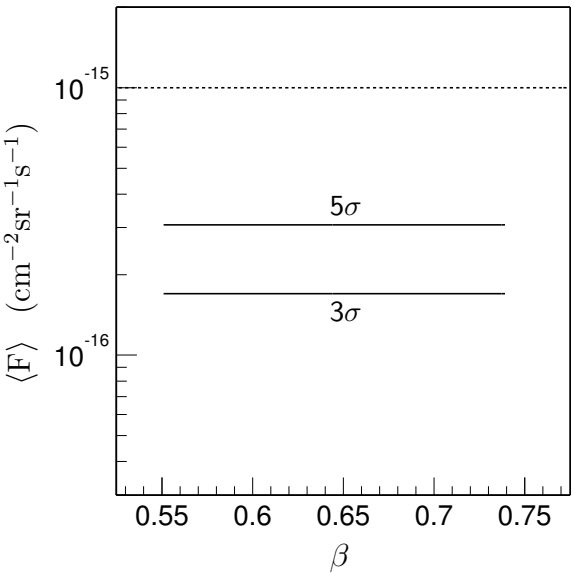

Figure 6.7: *The average monopole flux $\langle F \rangle$ needed to detect the minimum number of events per year for a discovery at the 3σ and 5σ significance levels (solid lines). The Parker upper limit on the monopole flux is also shown (dashed line).*

6.6 Discussion

Most events that are found by the monopole trigger are background events caused by atmospheric muons. The trigger detects several millions of these events per year. With the analysis presented in this chapter, an event selection can be applied that reduces this background with a factor of about 10^7 to less than one event per year. This results in the possibility to make a discovery at the 5σ level with only 7 events per year. The monopole flux that is needed to produce this number of events has been determined and is below the upper limit on the monopole flux set by Parker [66].

The Parker bound and the present experimental upper limits on the monopole flux are shown in figure 3.2. As can be seen from this figure, the AMANDA and Baikal neutrino telescopes have not set a limit on relativistic monopoles with velocities below the Cherenkov limit ($0.74\,c$). The methods described in this work show however, that detection of monopoles with these velocities is possible with a neutrino telescope, and that a meaningful search can be performed. Figure 3.2 also shows that the flux needed for a discovery with a 5σ significance with the analysis presented here has been excluded by the MACRO experiment [83]. However, the flux needed for a 3σ discovery is about the same as the limit set by MACRO. This experiment used several types of detectors to search for different monopole signatures based on their excitation and ionisation properties. The upper limit corresponds to a live time of about 5 years. The total acceptance of the MACRO detector was about 10^4 m^{2}sr, which is a factor of about 16 smaller than the acceptance of the ANTARES detector for up-going monopoles with velocities of about $0.60\,c$ (see figure 6.6).

To compare the performances of the ANTARES and MACRO detectors, the velocity-dependent effective area shown in figure 6.6 is translated into an upper limit on the monopole flux. For this, it is assumed that after one year of data taking with the ANTARES

detector, no event has been found with the analysis presented here[‡]. The resulting upper limit as a function of the monopole velocity is shown in figure 6.8 for a confidence level of 90%. The limit set by MACRO is also shown. The upper limit obtained with ANTARES is lower than the MACRO limit for monopoles with β between about 0.57 and 0.66. For $\beta \simeq 0.60$, the upper limit of MACRO obtained with 5 years of live time can be improved by a factor of about 3 with only one year of data taking with ANTARES. To obtain limits for longer periods of data taking with ANTARES, the value of Λ_c has to be adjusted.

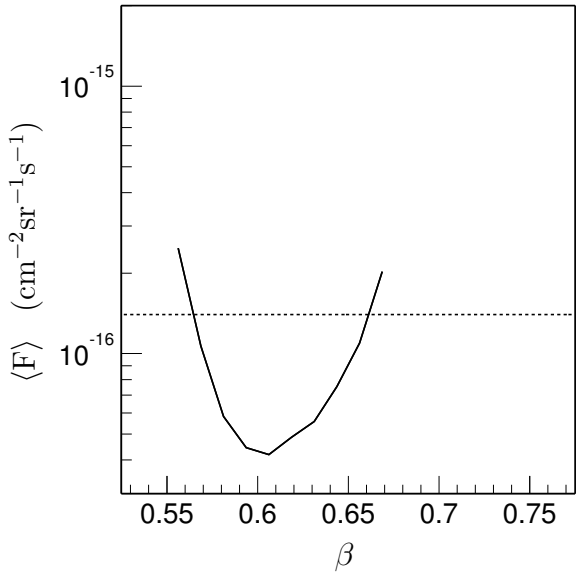

Figure 6.8: *Upper limit (90% confidence level) on the average monopole flux $\langle F \rangle$ as a function of the monopole velocity after one year of data taking with the ANTARES detector (solid line). The upper limit set by the MACRO detector is also shown (dashed line).*

The contribution of events that are the result of accidental coincidences of hits caused by random background has not been considered in the analysis. It is expected that the trigger finds less than 1000 of such events per year. For these events, a similar reduction factor as for atmospheric muons is expected. The net result is such that this background can safely be neglected.

The charge of a hit (see chapter 1) is a measure for the number of photons that arrived simultaneously on a PMT. This information is not used in the event analysis presented in this work. The significance and effect of using the hit charge in the analysis could be the subject of future studies.

Monopoles with velocities above the Cherenkov limit have not been considered in the development of the trigger and analysis methods described in this work. Other methods should be applied to identify the signals of these monopoles. Since they are characterised by a very bright Cherenkov signal, these methods could include the pulse height of the hits.

[‡]The probability to observe zero events after one year with an expected background of 0.4 events is about 70%.

Chapter 7

Summary and conclusions

The ANTARES collaboration is constructing a neutrino telescope in the Mediterranean Sea for the detection of high-energy cosmic neutrinos. The detector will consist of 900 photo-multiplier tubes that are positioned on 12 vertical strings. The strings are about 450 m long and are situated on the sea floor some 60 m apart. In this way a volume of about 0.02 km^3 of the sea will be instrumented. The detector is designed primarily for the detection of muon neutrinos. These can interact with matter via a charged current interaction in which a muon is produced. The Cherenkov radiation that this muon emits can be detected by the photo-multiplier tubes. By measuring the arrival times and intensities of the Cherenkov light, the direction and energy of the muon can be reconstructed. This provides information on the energy and direction of the incident neutrino.

The ANTARES detector has a data acquisition system which digitises, collects and processes the analogue signals from the photo-multiplier tubes. All photo-multiplier tube signals that cross a certain threshold are digitised, and the corresponding data are transported to the shore in compliance with the all-data-to-shore concept. The average counting rate per photo-multiplier tube is about 100 kHz. This rate is mainly due to background light from bioluminescence and the decay of ^{40}K. The corresponding data rate amounts to approximately 0.6 GByte/s for the whole detector. All these data are processed on shore in real time by a fast software trigger which is designed to find muon signals in the data. Only data samples that are possibly related to a muon signal are kept for further analysis, all other data are rejected. In this way, the data rate can be reduced by a factor of at least 10^4. The data stored by the trigger algorithm are analysed off-line with dedicated software to determine the direction and energy of the parent neutrinos.

The physics programme of the ANTARES collaboration also includes searches for exotic particles like magnetic monopoles. The detection of magnetic monopoles is the subject of the work described in this thesis. The possible existence of monopoles is one of the predictions of grand unified theories. Monopoles may have been created in the early Universe at the time of the spontaneous breakdown of a unified symmetry. Various choices of the unified group and its breaking pattern in the early Universe lead to predictions of monopole masses between 10^7 and 10^{17} GeV and monopole charges between one and several Dirac units. The most stringent, model-independent theoretical upper limit on the galactic monopole flux is the Parker bound. It is approximately 10^{-15} $cm^{-2}sr^{-1}s^{-1}$.

Monopoles can be accelerated by large scale magnetic fields in the cosmos. Obser-

vations and models of galactic and extragalactic magnetic fields suggest that monopoles with masses up to about 10^{15} GeV can be accelerated to relativistic velocities. Relativistic monopoles can be detected in underwater and underice neutrino telescopes due to the Cherenkov light that they emit. The most stringent upper limit on the flux of relativistic monopoles has been set experimentally by the AMANDA neutrino telescope. This upper limit corresponds to about 10 detectable monopoles per year for the ANTARES detector.

Monopoles emit very intense Cherenkov radiation in the sea water when their velocity exceeds the speed of light in the water. This threshold velocity is referred to as the Cherenkov limit, and corresponds to about $0.74\,c$. A preliminary study has shown that the detection of these fast monopoles with the ANTARES detector is possible provided that they can be distinguished from muons [12]. This requires a detailed study of the number of PMTs that record a hit and of the pulse heights of these hits when a monopole passes through the detector. Similar studies have been done for the analysis methods used by the Baikal and AMANDA neutrino telescopes, which have already set upper limits on the flux of fast monopoles.

In principle, monopoles can also be detected at velocities below the Cherenkov limit due to the large number of δ-rays that they produce along their path. When these δ-rays are energetic enough, they can emit Cherenkov light. This can lead to detectable signals of monopoles with velocities down to about half the speed of light. The number of Cherenkov photons emitted by the δ-rays increases with increasing monopole velocity. Above about $0.60\,c$, the total light yield of the δ-rays exceeds that of a minimum ionising muon. The light emission of the δ-rays is characterised by a rather broad angular spread of the photons. This spread also increases with the monopole velocity.

This thesis describes the development of a software trigger and an analysis method that are dedicated to the detection of monopoles below the Cherenkov limit. To quantify the performance of the trigger and analysis algorithms, the δ-ray induced Cherenkov radiation of a monopole has been incorporated into a program that is used to simulate the detector response.

The standard muon trigger searches for time-position correlations between hits in the raw data based on the properties of the Cherenkov light emission by a muon. These properties are summarised in a single causality relation that is used by the muon trigger. The time-position correlations between hits due to a slow monopole can be different from those between hits due to a muon as a consequence of the different velocity and light emission of the monopole. This effect causes the muon trigger to be inefficient for signals of monopoles below the Cherenkov limit. Therefore, a new trigger has been developed. This new trigger uses a set of causality relations in which the main properties of the signals of slow monopoles are summarised. As a result, the new trigger is more sensitive to slow monopoles than the muon trigger.

Atmospheric muons, atmospheric neutrinos and random background can produce signals in the detector that resemble a passing monopole. These background signals can be accidentally found by the monopole trigger. In addition to the hit selection based on the causality relations, three more constraints are applied in the trigger to reduce the accidental trigger rate. A minimum cluster size and a maximum transverse distance are applied mainly to suppress random background. A third constraint is applied to reduce background signals caused by atmospheric muons. Since these muons travel through the

detector in downward directions, only upward directions are considered in the trigger. This means that the monopoles must penetrate the Earth in order to be detected. Monopoles with masses below about 10^{15} GeV can penetrate the Earth and still be fast enough to produce a detectable signal.

The total rate of background events found by the monopole trigger is about 0.11 Hz for a singles rate of 100 kHz. The corresponding reduction of the data rate achieved with the monopole trigger is then a factor of about 2×10^6. For monopoles with velocities below about $0.60\,c$, the monopole trigger is a factor between 2 and 20 more efficient in finding monopole signals than the muon trigger. For monopole velocities between $0.60\,c$ and $0.74\,c$, the efficiencies of both triggers are about the same. However, the background of the monopole trigger is a factor of approximately 50 less than that of the muon trigger. The speed of the trigger algorithm is such, that about 10 processors of 2.2 GHz are needed to process the raw data coming from the detector in real time.

The monopole trigger has been implemented in such a way, that it can be used for all velocities below the Cherenkov limit. The only requirement is that the particle to be detected should exhibit light emission in forward directions. In fact, the trigger has been tested successfully in a study of the possibilities to detect nuclearites with velocities of $10^{-3}\,c$ with the ANTARES detector [101].

Most events found by the monopole trigger are due to background signals caused by atmospheric muons and by muons produced in interactions of atmospheric neutrinos. Only a very small fraction of the events might be caused by magnetic monopoles. In order to distinguish monopole events from the background, the events are analysed off-line. This is done with a dedicated software program that calculates the probability of the observed data for the hypothesis that it was produced by a muon and for the hypothesis that is was produced by a monopole. The program consists of two successive fitting procedures in which the likelihood of the event for a given hypothesis is maximised. The first fitting procedure is a linear least squares fit. It provides a starting point for the second fitting procedure, which is a maximum likelihood fit. In both procedures information on the particle velocity and the emission angle, intensity and propagation of the produced light is used.

The decision whether an event was caused by a monopole or by a muon is based on a likelihood ratio test. For the muon hypothesis, the global maximum of the likelihood is taken. The maximum likelihood for the monopole hypothesis is selected from values associated only with upward directions. The logarithm of the ratio of the two maximum likelihood values is a measure for the compatibility of the data with a monopole signal. A first selection on the basis of the likelihood ratio rejects about 99% of the atmospheric muon events and about 96% of the atmospheric neutrino events. The fraction of monopole events that is accepted is about 95%. To find a monopole event unambiguously, a final cut is applied to the data. This cut is based on the value of the likelihood ratio.

The sensitivity of the ANTARES detector to a flux of through-going monopoles can be represented by an effective area. After application of the monopole trigger and the event analysis including the final cut, the effective area of the detector is about 5×10^3 m^2 for monopoles with velocities of about $0.55\,c$. The effective area increases to about 2.8×10^4 m^2 for monopole velocities of about $0.60\,c$. Above $0.60\,c$, it decreases again. This decrease is due to the fact that the distinction between a monopole signal and a muon signal becomes

more difficult as the monopole velocity increases.

The expected number of background events that remain after applying the final cut is about 0.4 per year. This means that the background has been reduced with a factor of about 10^7. This gives the possibility to make a discovery at the 3σ (5σ) significance level with only 4 (7) events that survive the final cut per year. The average monopole flux that is needed to produce this number of events is a factor of about 6 (3) below the flux upper limit set by Parker.

The Baikal and AMANDA neutrino telescopes have not set a limit on the flux of relativistic monopoles with velocities below the Cherenkov limit. The methods described in this thesis show that detection of monopoles with these velocities is also possible with a neutrino telescope. When it is assumed that after one year of data taking with the ANTARES detector no event has been found, the effective area of the detector can be translated into an upper limit on the monopole flux. For a confidence level of 90%, the upper limit obtained with ANTARES will be below the upper limit set by the MACRO experiment for monopoles with velocities between approximately $0.57\,c$ and $0.66\,c$. For velocities of about $0.60\,c$, the MACRO limit can be improved by a factor of about 3.

References

[1] The ANTARES Collaboration, *A Deep Sea Telescope for High Energy Neutrinos*, May 1999. astro-ph/9907432

[2] R. Gandhi et al., *Ultrahigh-Energy Neutrino Interactions.* Astroparticle Physics **5**, 81 (1996)

[3] J.D. Jackson, *Classical Electrodynamics.* John Wiley & Sons, Inc., 1998

[4] J. Brunner, *The Refraction Index at the ANTARES Site*, October 2000. ANTARES internal note Site/2000-001

[5] J.A. Aguilar et al., *Transmission of Light in Deep Sea Water at the Site of the ANTARES Neutrino Telescope.* Astroparticle Physics **23**, 131 (2005)

[6] L.A. Kuzmichev, *On the Velocity of Light Signals in Deep Underwater Neutrino Experiments.* Nuclear Instruments and Methods A **482**, 304 (2002)

[7] D.J.L. Bailey, *Monte Carlo Tools and Analysis Methods for Understanding the ANTARES Experiment and Predicting Its Sensitivity to Dark Matter.* Ph.D. Thesis, Wolfson College, Oxford, 2002

[8] The ANTARES Collaboration, *Technical Design Report of the ANTARES 0.1 km^2 project, Version 1.0*, July 2001

[9] P. Amram et al., *The ANTARES Optical Module.* Nuclear Instruments and Methods A **484**, 369 (2002)

[10] The Rolling Stones, *Paint it black*, 1966

[11] F. Feinstein, *The Analogue Ring Sampler: A Front-end Chip for ANTARES.* Nuclear Instruments and Methods A **504**, 258 (2003)

[12] Js. Ricol, *Etude de la Détection de Monopôles Magnétiques au Sein du Futur Télescope á Neutrinos Antares et Caractérisation des Performances du Traitement des Impulsions des Photomultiplicateurs.* Ph.D. Thesis, Université de la Méditerranée Aix-Marseille II, Marseille, 2002

[13] A.J. Heijboer, *private communication*

[14] R. Brun and F. Rademakers, *ROOT - An Object Oriented Data Analysis Framework.* Nuclear Instruments and Methods A **389**, 81 (1997)

[15] P.J. Lucas, *An Object-Oriented Language System for Implementing Concurrent, Hierarchical, Finite State Machines.* Master's Thesis, University of Illinois at Urbana-Champaign, Urbana, Illinois, 1993

[16] R. van Wijk.
`http://www.nikhef.nl/~ruud/HTML/choo_manual.html`

[17] R. Gurin and A. Maslennikov, *ControlHost: Package for Distributed Data Handling.* CASPUR Inter-University Computing Consortium Rome (1995)

[18] M.C. Bouwhuis, *Detection of Neutrinos from Gamma-Ray Bursts.* Ph.D. Thesis, Universiteit van Amsterdam, Amsterdam, 2005

[19] J. Brunner, *Simulation of ^{40}K signals*, June 1999. ANTARES internal note Site/1999-002

[20] *ANTARES Status June 2003*, 2003.
`http://antares.in2p3.fr/ERC/ERC_July_2003.pdf`

[21] B.A.P. van Rens, *The Software Trigger in ANTARES*, March 2004. ANTARES internal note Soft/2004-001

[22] M. de Jong, *The ANTARES Trigger Software*, May 2005. ANTARES internal note Soft/2005-005

[23] R. Bruijn, *private communication*

[24] Particle Data Group, *Passage of Particles through Matter.* European Physical Journal C **3**, 144 (1998)

[25] R. Bruijn, *Muon Energy Reconstruction in ANTARES Using Neural Networks.* Master's Thesis, Universiteit van Amsterdam, Amsterdam, 2002

[26] A.J. Heijboer, *Track Reconstruction and Point Source Searches with ANTARES.* Ph.D. Thesis, Universiteit van Amsterdam, Amsterdam, 2004

[27] D. Heck et al., *CORSIKA: A Monte Carlo Code to Simulate Extensive Air Showers.* Forschungszentrum Karlsruhe Report **FZKA 6019** (1998).
`http://www-ik.fzk.de/corsika/`

[28] E. Korolkova and L. Thompson, *Monte Carlo Simulation of Cosmic Ray Muons at Sea Level with CORSIKA*, March 2003. ANTARES internal note Soft/2003-002

[29] P. Antonioli et al., *A Three-dimensional Code for Muon Propagation through the Rock: MUSIC.* Astroparticle Physics **7**, 357 (1997)

[30] S. Navas and L. Thompson, *KM3 User Guide and Reference Manual*, November 1999. ANTARES internal note Soft/1999-011

[31] J. Brunner, *GEASIM*, March 2000.
`http://antares.in2p3.fr/internal/software/geasim.html`

[32] Application Software Group, *GEANT - Detector Description and Simulation Tool*. CERN Program Library Long Writeup **W5013** (1993).
`http://wwwasd.web.cern.ch/wwwasd/geant/`

[33] `http://www.itu.int/home/`

[34] J. Hogenbirk and P. Rewiersma, *Design Specifications for the ANTARES Optical DAQ-DWDM Network, Part I: Passive Optical Network*, Technical Report ETR2000-07, NIKHEF, Amsterdam, The Netherlands, 2001

[35] J. Hogenbirk and P. Rewiersma, *Design Specifications for the ANTARES Optical DAQ-DWDM Network, Part II: Optical/Electrical & Electronics*, Technical Report ETR2000-08, NIKHEF, Amsterdam, The Netherlands, 2000

[36] EXFO Electro-Optical Engineering, Inc., *Lightwave Test and Measurement*, Reference Guide, 2001

[37] *IEEE 802.3z Gigabit Ethernet Standard*

[38] D.G. Cunningham and W.G. Lane, *Gigabit Ethernet Networking*. Macmillan Technical Publishing, 1999

[39] Maxim Integrated Products, Inc., *Jitter in Digital Communication Systems, Part I*, Application Note HFAN-4.0.3, 2001

[40] Tektronix, Inc., *Measure Error Rates Quickly and Accurately*, Technical Brief, 2001

[41] Tektronix, Inc., *Real-Time versus Equivalent-Time Sampling*, Applications Note

[42] E. Kok, H.Z. Peek and R. van Wijk, *Bit Error Ratio Determination by Failing TCP/IP Transfers*, ANTARES internal note Elec/2003-001, NIKHEF, Amsterdam, The Netherlands, 2003

[43] P.A.M. Dirac, *Quantised Singularities in the Electromagnetic Field*. Proceedings of the Royal Society of London **133**, 60 (1931)

[44] G. 't Hooft, *Magnetic Monopoles in Unified Gauge Theories*. Nuclear Physics B **79**, 276 (1974)

[45] A.M. Polyakov, *Particle Spectrum in Quantum Field Theory*. JETP Letters **20**, 194 (1974)

[46] S. Weinberg, *The Quantum Theory of Fields, Volume II: Modern Applications*. Cambridge University Press, 1996

[47] D.A. Kirzhnits, *Weinberg Model and The "Hot" Universe*. JETP Letters **15**, 529 (1972)

[48] T.W.B. Kibble, *Topology of Cosmic Domains and Strings.* Journal of Physics A **9**, 1387 (1976)

[49] J.P. Preskill, *Cosmological Production of Superheavy Magnetic Monopoles.* Physical Review Letters **43**, 1365 (1979)

[50] A.H. Guth and E.J. Weinberg, *Could the Universe Have Recovered from a Slow First-Order Phase Transition?* Nuclear Physics B **212**, 321 (1983)

[51] G. Giacomelli, *Magnetic Monopoles.* La Rivista del Nuovo Cimento **7**, 1 (1984)

[52] H. Georgi, H.R. Quinn and S. Weinberg, *Hierarchy of Interactions in Unified Gauge Theories.* Physical Review Letters **33**, 451 (1974)

[53] M. Daniel, G. Lazarides and Q. Shafi, *SU(5) Monopoles, Magnetic Symmetry and Confinement.* Nuclear Physics B **170**, 156 (1980)

[54] G. Lazarides, C. Panagiotakopoulus and Q. Shafi, *Magnetic Monopoles from Superstring Models.* Physical Review Letters **58**, 1707 (1987)

[55] G. Lazarides and Q. Shafi, *Extended Structures at Intermediate Scales in an Inflationary Cosmology.* Physics Letters B **148**, 35 (1984)

[56] T.W. Kephart and T.J. Weiler, *Magnetic Monopoles as the Highest Energy Cosmic Ray Primaries.* Astroparticle Physics **4**, 271 (1996)

[57] P.H. Frampton and B.H. Lee, *SU(15) Grand Unification.* Physical Review Letters **64**, 619 (1990)

[58] P.H. Frampton and T.W. Kephart, *Higgs Sector and Proton Decay in SU(15) Grand Unification.* Physical Review D **42**, 3892 (1990)

[59] S.F. King and Q. Shafi, *Minimal Supersymmetric* $SU(4)\times SU(2)_L\times SU(2)_R$. Physics Letters B **422**, 135 (1998)

[60] T.W. Kephart and Q. Shafi, *Family Unification, Exotic States and Magnetic Monopoles*, May 2001. hep-ph/0105237

[61] M.S. Turner, E.N. Parker and T.J. Bogdan, *Magnetic Monopoles and the Survival of Galactic Magnetic Fields.* Physical Review D **26**, 1296 (1982)

[62] E. Huguet and P. Peter, *Bound States in Monopoles: Sources for UHECR?* Astroparticle Physics **12**, 277 (2000)

[63] E.W. Kolb and M.S. Turner, *The Early Universe*, in Frontiers in Physics. Perseus Publishing, 1990

[64] S.D. Wick, T.W. Kephart, T.J. Weiler and P.L. Biermann, *Signatures for a Cosmic Flux of Magnetic Monopoles*, April 2000. astro-ph/0001233

[65] `http://map.gsfc.nasa.gov`

[66] E.N. Parker, *The Origin of Magnetic Fields.* The Astrophysical Journal **160**, 383 (1970)

[67] E.N. Parker, *The Generation of Magnetic Fields in Astrophysical Bodies II: The Galactic Field.* The Astrophysical Journal **163**, 255 (1971)

[68] S.P. Ahlen, *Monopole-Track Characteristics in Plastic Detectors.* Physical Review D **14**, 2935 (1976)

[69] S.P. Ahlen, *Stopping-power Formula for Magnetic Monopoles.* Physical Review D **17**, 229 (1978)

[70] Y. Kazama, C.N. Yang and A.S. Goldhaber, *Scattering of a Dirac Particle with Charge Ze by a Fixed Magnetic Monopole.* Physical Review D **15**, 2287 (1977)

[71] D.R. Tompkins, *Total Energy Loss and Čerenkov Emission from Monopoles.* Physical Review **138**, 248 (1965)

[72] S.D. Wick, T.W. Kephart and T.J. Weiler, *Signature Studies of Cosmic Magnetic Monopoles*, February 2001. astro-ph/0102002

[73] V.A. Rubakov, *Superheavy Magnetic Monopoles and Decay of the Proton.* JETP Letters **33**, 644 (1981)

[74] V.A. Rubakov, *Adler-Bell-Jackiw Anomaly and Fermion-Number Breaking in the Presence of a Magnetic Monopole.* Nuclear Physics B **203**, 311 (1982)

[75] C.G. Callan, *Disappearing Dyons.* Physical Review D **25**, 2141 (1982)

[76] C.G. Callan, *Dyon-Fermion Dynamics.* Physical Review D **26**, 2058 (1982)

[77] V.A. Rubakov, *Monopole Catalysis of Proton Decay.* Reports on Progress in Physics **51**, 189 (1988)

[78] J. Arafune and M. Fukugita, *Velocity-Dependent Factors for the Rubakov Process for Slowly Moving Magnetic Monopoles in Matter.* Physical Review Letters **50**, 1901 (1983)

[79] S. Dawson and A.N. Schellekens, *Monopole Catalysis of Proton Decay in SO(10) Grand Unified Models.* Physical Review D **27**, 2119 (1983)

[80] A.N. Schellekens, *Boundary-Condition Independence of Catalysis of Proton Decay by Monopoles.* Physical Review D **29**, 2378 (1984)

[81] T.F. Walsh, P. Weisz and T.T. Wu, *Monopole Catalysis of Proton Decay.* Nuclear Physics B **232**, 349 (1984)

[82] B. Cabrera, *First Results from a Superconductive Detector for Moving Magnetic Monopoles.* Physical Review Letters **48**, 1378 (1982)

[83] M. Ambrosio et al., *Final Results of Magnetic Monopole Searches with the MACRO Experiment*, July 2002. hep-ex/0207020

[84] S. Orito et al., *Search for Supermassive Relics with a 2000-*m^2 *Array of Plastic Track Detectors.* Physical Review Letters **66**, 1951 (1991)

[85] V.A. Balkanov et al., *The Lake Baikal Neutrino Experiment.* Physics of Atomic Nuclei **66**, 503 (2003)

[86] P. Niessen, *Search for Relativistic Magnetic Monopoles with the AMANDA Detector.* Ph.D. Thesis, Humboldt-Universität, Berlin, 2001

[87] J. Bartelt et al., *Monopole-Flux and Proton-Decay Limits from the Soudan 1 Detector.* Physical Review D **36**, 1990 (1987)

[88] R. Becker-Szendy et al., *New Magnetic Monopole Flux Limits from the IMB Proton Decay Detector.* Physical Review D **49**, 2169 (1994)

[89] R.M. Sternheimer, *Density Effect for the Ionization Loss in Various Materials.* Physical Review **103**, 511 (1956)

[90] G. Giacomelli et al., *Energy Losses of Fast Magnetic Monopoles in Water*, March 2001. ANTARES internal note Phys/2001-003

[91] B. Rossi, *High-Energy Particles.* Prentice-Hall, Inc., 1952

[92] S.M. Seltzer and M.J. Berger, *Improved Procedure for Calculating the Collision Stopping Power of Elements and Compounds for Electrons and Positrons.* International Journal of Applied Radiation and Isotopes **35**, 665 (1984)

[93] G.R. Lynch and O.I. Dahl, *Approximations to Multiple Coulomb Scattering.* Nuclear Instruments and Methods B **58**, 6 (1991)

[94] Particle Data Group, *Atomic and Nuclear Properties of Materials.* European Physical Journal C **3**, 76 (1998)

[95] J. Derkaoui et al., *Energy Losses of Magnetic Monopoles and of Dyons in the Earth.* Astroparticle Physics **9**, 173 (1998)

[96] D. Dshilkibaev and C. Spiering, *Search for Magnetic Monopoles with the Baikal Underwater Neutrino Telescope* . Unpublished, 1998

[97] B. Wiebel-Sooth et al., *Cosmic Rays VII. Individual Element Spectra: Prediction and Data.* Astronomy and Astrophysics **330**, 389 (1998)

[98] V. Agrawal et al., *Atmospheric Neutrino Flux above 1 GeV.* Physical Review D **53**, 1314 (1996)

[99] M. Thunman et al., *Charm Production and High Energy Atmospheric Muon and Neutrino Fluxes.* Astroparticle Physics **5**, 309 (1996)

[100] F. James, *MINUIT - Function Minimization and Error Analysis.* CERN Program Library Long Writeup **D506** (1994)

[101] V. Popa, *private communication*

Samenvatting

Zoals bekend, hebben alle magnetische voorwerpen twee tegenovergestelde polen, genaamd de noordpool en de zuidpool. Geïsoleerde magnetische polen, ook wel magnetische monopolen genaamd, zijn nog nooit waargenomen. Niettemin zijn er theorieën die het bestaan van magnetische monopolen voorspellen. Zo zouden monopolen geproduceerd kunnen zijn in het vroege heelal, vlak na de oerknal, in de vorm van sub-atomaire deeltjes. Deze deeltjes zouden dan als relikwieën van de oerknal door het heelal zwerven.

Monopolen zijn interessante objecten om naar te zoeken omdat ze ons informatie kunnen verschaffen over het vroege heelal. Dit proefschrift beschrijft het voorbereidende werk voor een zoektocht naar magnetische monopolen met de ANTARES neutrino telescoop. Dit is een groot meetinstrument dat ontworpen is voor het detecteren van kosmische neutrino's. Het wordt gebouwd op de bodem van de Middellandse Zee, op een diepte waar geen daglicht meer doordringt. Kosmische neutrino's worden indirect waargenomen door het detecteren van o.a. muonen die geproduceerd kunnen worden in botsingen van de neutrino's met atoomkernen in het zeewater of in de zeebodem. Als zo'n muon een snelheid heeft die groter is dan de lichtsnelheid in het zeewater, straalt het zogenaamd Cherenkov licht af. Deze snelheidsdrempel wordt daarom ook wel de Cherenkov limiet genoemd. De ANTARES detector bestaat uit 900 lichtgevoelige sensoren die dit licht kunnen opvangen. Uit de relatieve aankomsttijden en de intensiteit van de gemeten lichtpulsjes kunnen de energie en bewegingsrichting van het muon bepaald worden. Dit geeft informatie over de energie en richting van het oorspronkelijke neutrino.

Na hun ontstaan in het vroege heelal, kunnen monopolen versneld zijn door zwaartekrachtsvelden en magneetvelden die aanwezig zijn in de kosmos. Theoretische voorspellingen van de snelheid waarmee monopolen door het heelal zwerven lopen ver uiteen. Het is mogelijk om met een neutrino telescoop te zoeken naar monopolen die met snelheden dicht bij die van het licht door het heelal reizen. Deze snelle monopolen zenden namelijk ook Cherenkov licht uit in water, en hun signaal lijkt dus sterk op dat van een muon. Echter, monopolen kunnen ook detecteerbare signalen produceren bij lagere snelheden die onder de Cherenkov limiet liggen. Als monopolen door het water bewegen, botsen ze met de elektronen die aanwezig zijn in de watermoleculen. Deze elektronen kunnen door zo'n botsing met een grote snelheid uit het molecuul vrijkomen. De vrijgekomen elektronen zenden dan op hun beurt Cherenkov licht uit. Dit schept de mogelijkheid om met een neutrino telescoop te zoeken naar langzame monopolen. De detectie van deze langzame monopolen met de ANTARES detector is het onderwerp van dit proefschrift. Aangezien monopolen tot nu toe niet zijn waargenomen, hebben zoektochten enkel geleid tot bovengrenzen op de dichtheid van monopolen in het heelal.

Het overgrote deel van de lichtpulsjes die gemeten worden door de lichtsensoren in

de detector wordt geproduceerd door lichtgevende organismen in het zeewater en door het verval van radioactief kalium dat aanwezig is in het zeezout. Daarnaast wordt licht gemeten dat afkomstig is van muonen die door de detector bewegen. Deze processen hebben niets met een monopool te maken en worden daarom achtergrond genoemd. In totaal worden per seconde ongeveer 100.000 lichtpulsjes gemeten door iedere lichtsensor. Men verwacht dat slechts een zeer klein deel hiervan door een monopool veroorzaakt zou kunnen zijn. Om zo min mogelijk informatie te verliezen, worden alle meetgegevens van de lichtsensoren naar de kust getransporteerd. De totale hoeveelheid meetgegevens is echter te veel om op te kunnen slaan. Daarom worden alle meetgegevens op de kust razendsnel verwerkt door computers. Op deze computers draait een speciaal ontwikkeld software programma dat het signaal van een monopool uit de enorme hoeveelheid achtergrond filtert. Dit programma wordt de monopool trigger genoemd. Deze trigger zoekt naar correlaties tussen lichtpulsjes op basis van de karakteristieke snelheid en lichtproductie van langzame monopolen. Een verzameling meetgegevens die mogelijkerwijs veroorzaakt zijn door zo'n monopool wordt bewaard, alle andere meetgegevens worden weggegooid. Zo'n verzameling meetgegevens wordt een gebeurtenis genoemd. Op deze manier wordt het aantal meetgegevens met een factor van ongeveer twee miljoen teruggebracht.

Muonen kunnen een signaal in de detector produceren dat lijkt op een signaal van een langzaam monopool. Het kan voorkomen dat de monopool trigger zo'n achtergrond signaal foutief aanziet voor een monopool signaal en de overeenkomstige meetgegevens toch opslaat. Dit gebeurt ongeveer een keer per tien seconden. Het aantal achtergrond gebeurtenissen dat zo per jaar door de trigger gevonden wordt is vele malen groter dan het verwachte aantal monopolen. Het vinden van een monopool komt dus neer op het zo goed mogelijk scheiden van muon en monopool signalen. Dit gebeurt in een speciaal ontwikkelde analyse waaraan alle bewaarde gebeurtenissen onderworpen worden. In deze analyse worden de meetgegevens van elke gebeurtenis nauwkeurig vergeleken met de karakteristieke eigenschappen van een monopool signaal en die van een muon signaal. Op deze manier kan het aantal achtergrond gebeurtenissen teruggebracht worden naar minder dan één per jaar. Met zo'n lage achtergrond is het mogelijk om onomstotelijk een monopool te vinden.

De ontwikkelde trigger en analyse methodes laten zien dat het mogelijk is om monopolen met snelheden zo laag als de halve lichtsnelheid te detecteren met de ANTARES detector. In het geval dat er geen enkele monopool gebeurtenis gevonden wordt, kan er een bovengrens gesteld worden op de dichtheid van monopolen in het heelal. Dankzij de speciaal ontwikkelde methodes kan na één jaar meten met de ANTARES detector de reeds bestaande bovengrens met een factor drie verbeterd worden.

Dankwoord

De afgelopen jaren heb ik op het NIKHEF met ontzettend veel plezier gewerkt aan mijn promotieonderzoek. Collega's, vrienden en familie hebben allemaal op hun eigen manier bijgedragen aan deze erg goede tijd. Ik wil graag iedereen hiervoor bedanken. Een aantal mensen wil ik hier in het bijzonder noemen.

Maarten, aan jou ben ik veruit de meeste dank verschuldigd. "Ik zie je wel met hangende pootjes terugkomen" zei je, nadat ik besloten had om mijn promotiecapaciteiten te gaan beproeven in de Verenigde Staten. En je kreeg gelijk. Super dat je mij toen alsnog een promotieplek onder jouw begeleiding hebt aangeboden. Een betere plek had ik me niet kunnen wensen. En een betere begeleider al helemaal niet! Je enthousiasme en onuitputtelijke drive hebben me al die tijd enorm gemotiveerd. Zonder jouw kennis, 24/7 hulp en briljante ideeën had ik dit proefschrift nooit kunnen schrijven. En je flexibiliteit in tijden dat mam's gezondheid het liet afweten was uiteraard van onschatbare waarde. Ik vind het dan ook een eer om, nu je professor bent, je eerste promovendus te mogen zijn. Maarten, bedankt!

Paul, hartstikke bedankt dat je in het laatste jaar van mijn promotie wilde aantreden als mijn promotor. Je betrokkenheid bij mijn onderzoek sindsdien heb ik zeer gewaardeerd. Ik kijk met plezier terug op de interessante gesprekken die we hebben gehad, en jouw wijsheid en waardevolle adviezen zijn zeker ten goede gekomen aan de kwaliteit van dit proefschrift.

Aart en Mieke, jullie wil ik graag bedanken voor de erg gezellige en rielekste sfeer in H351, en natuurlijk ook daarbuiten. Jullie hebben een belangrijk aandeel gehad in mijn welzijn binnen de ANTARES groep. Ik kon altijd bij jullie terecht met vragen over uiteenlopende zaken. Ronald, ook jouw hulp in de laatste maanden was erg waardevol.

Erwin, ik wil je bedanken voor de prettige samenwerking en je uitstekende begeleiding bij mijn kennismaking met de wondere wereld van fibers, gigabits en multiplexers. Jouw kennis en nauwgezet commentaar waren onmisbaar bij het tot stand komen van hoofdstuk 2.

Ana, your clear explanations of subjects related to monopoles and cosmology have helped a great deal in my understanding of those topics. Thank you very much.

Jean-stéphane, your work on monopole detection provided me with a quick start. Thanks a lot for your explanations and assistance with the simulation software. Jürgen, I'm also grateful to you for your help with the simulation code and related topics.

Gijsbert en Menno, hartstikke bedankt voor het nemen van de tijd en moeite om delen van dit proefschrift nauwkeurig door te lezen en te voorzien van commentaar en suggesties.

Jan, Gordon, Bob, Faab en Jan V., de niet onbelangrijke uren buiten NIKHEF heb ik veelvuldig met jullie doorgebracht. De lange spelletjes avonden, 't stappen in Paradiso,

de potjes pool en het pakken van een filmpje waren super. Bedankt!

Pap en Mam, aan jullie heb ik zoveel te danken...

En tenslotte, Marcella, bedankt dat je er voor me was. Kus!